博士論文

Functionalizations of single-walled carbon nanotubes and their application on solar cells

（単層 CNT の機能化と太陽電池応用）

Seungju SEO

（徐 昇柱）

Doctoral Dissertation

Functionalizations of single-walled carbon nanotubes and their application on solar cells

by

Seungju SEO

Presented to

GRADUATE SCHOOL OF ENGINEERING, THE UNIVERSITY OF TOKYO

in Partial Fulfillment of the Requirements for the Degree of

Doctoral of Philosophy

in the Field of Mechanical Engineering

March 2021

Abstract

Single-walled Carbon Nanotubes (SWNTs) have been widely explored in many fields to be integrated into new functional devices arising from their exciting optical, electrical, and thermal properties along with their mechanical and chemical stability. Solar cell application of SWNTs is one of the most promising application of SWNTs since they can be incorporated in various functional layers of solar cell devices as well as their earth abundance and stability. However, the main challenge regarding co-existence of metallic (m-SWNT) and semiconducting SWNTs (s-SWNTs) after synthesis has to be overcome to maximize SWNTs' potential on solar cell application, as small incorporation of either s-SWNTs into m-SWNTs or vice versa could seriously undermine the as-desired physical property of the SWNTs as functional material in solar cell devices. While controlled synthesis for chiral-specific growth of SWNTs has been extensively studied, they often result in low synthesis yield and thus have proven to be not favorable for large-scale device fabrication. On the other hand, the functionalization of as-synthesized SWNTs has also been widely used for subsequent device application of SWNTs. In solar cell application, however, the limited understanding and application of SWNT functionalization in solar cell devices has hindered the further improvement of device performance of SWNT-based solar cells compared to that of inorganic or organic counterparts.

This doctoral thesis aims at exploring the new possibility of functionalized SWNT application on solar cell devices and understanding how functionalized SWNTs can benefit to achieve high photovoltaic performance in solar cell devices, especially in perovskite solar cells. Perovskite solar cells have attracted much attention as an alternative energy source as their power conversion efficiency (PCE) was reported to be over 25 % in 2020 on top of their easy processibility with cheap materials. However, reported efficiency is still below 33 % of the theoretical limit and also improving PCE can further and most efficiently reduce the module cost of solar cells, since more than half of the total solar cell system cost comes from the module cost. So, integrating

functionalized s-SWNTs into perovskite solar cells to improve device performance and understanding their roles under device operation was the main goal of this doctoral study.

First, adding small amount of surfactant-functionalized s-SWNTs into perovskite precursor was found to improve crystal quality of perovskite film as well as charge extraction under device operation. Achieving large grain size as well as efficiently passivating grain boundaries is crucial to minimize non-radiative recombination of photo-generated carriers in perovskite solar cells. 2 wt% of surfactant (sodium deoxycholate) functionalized s-SWNTs was incorporated into perovskite precursor solution to accomplish larger grain size and grain boundary passivation, owing to their surfactant forming Lewis adduct with perovskite precursor PbI_2. It was found that they can efficiently passivate the perovskite grain boundaries and also benefit charge extraction from perovskite absorbers, thus leading to enhanced efficiency of perovskite solar cells of 19.5 % compared to 18.1 % reference device. This work paved a new way for SWNT application on perovskite solar cells where dispersed and surfactant-functionalized s-SWNTs can efficiently benefit perovskite crystal growth and charge transfer leading to higher device performances of perovskite solar cells. This work also suggests that by carefully designing dispersing agent of SWNTs that can comply with perovskite crystal growth, higher efficiency in PSCs can also be achieved.

Second, thermally evaporated molybdenum trioxide (MoO_3) was found to be efficient *p*-dopant for CNT top transparent electrodes in semi-transparent perovskite solar cells for perovskite-silicon tandem solar cells. This was achieved by thermally evaporating MoO_3 on as-laminated CNTs in perovskite solar cells. It was found that direct contact between MoO_3 and perovskite absorber can induce interfacial states which led to degradation of device performance. By modifying device fabrication process where MoO_3 deposition was followed by p-type organic semiconducting material (Spiro-OMeTAD) deposition on CNTs, 20.25 %-efficient semi-transparent perovskite solar cell with CNT-70T% top electrode was successfully fabricated. Enhanced charge extraction dynamics owing to efficient *p*-doping of CNT electrodes with MoO_3 was

characterized through various spectroscopy methods including PYS, PL, and EIS. Furthermore, perovskite-silicon tandem simulation was analyzed with p-n junction silicon bottom cell. In tandem with silicon bottom cell of 14.84 % PCE, 23.26 % efficient perovskite-silicon tandem solar cell with CNT-70T% top transparent electrode was simulated based on optical transmittance of perovskite top cell.

Acknowledgement

First and mostly, I would like to thank my supervisor, Prof. Shigeo Maruyama. When I decided to go to the University of Tokyo (UTokyo) for graduate school, I have never imagined that I would further pursue PhD studies when I first came from Waseda University right after graduation. I was very and most fortunate to have met my academic advisor, Prof. Shigeo Maruyama, who taught me how to do research, become an independent thinker. He never stopped me trying new approach for research but rather encouraged me in all ways. He always mentioned that doing a good science that can benefit other scientists and researchers is most important. I am particularly grateful for all of the encouragement, perspective and confidence from him during my studies.

I have been very privileged to have been able to work with amazing faculties, postdocs, and students within our group. Especially, Prof. Il Jeon has been an amazing mentor for both academic and personnel discussions. I learned everything about solar cell from him and was great to work with him during my PhD studies. Also, I would like to thank amazing faculties and colleagues including Prof. Shohei Chiashi, Prof. Xiang Rong, Prof. Taiki Inoue, Prof. Yutaka Matsuo, Prof. Keigo Otsuka, Dr. Yang Qian, Dr. Ahmed Shawky, Prof. Hao-sheng Lin, Dr. Yuki Itabashi, Dr. Takafumi Nakagawa, Dr. Hiroshi Okada, Prof. Hiroshi Ueno, Mr. Kousuke Akino, Mr. Shuhei Okawa, Mr. Hiroki Nagaya, Dr. Kaoru Hisama, Dr. Ming Liu, Dr. Yongjia Zheng, and Dr. Pengyingkai Wang. Also, especially I would like to thank Watanabe-san, Terao-san, and Shimada-san for supporting my research activities as staffs in Maruyama-Chiashi Lab. Also, I would like to thank to my Ph.D. defense committee professors for giving me valuable comments to further improve my Ph.D. research; Prof. Delaunay and Prof. Nagashio

I have been very privileged to have been able to visit Prof. A. John Hart's group and Prof. Jeehwan Kim group at Massachusetts Institute of Technology (MIT) during my graduate studies. I would like to thank Prof. Sang-Hoon Bae, Prof. Sanha Kim, Prof. Kehang Cui, Mr. Chanyeol Choi, Mr. Doyoon Lee, Dr. Peng Chen, Mr. Jaekang Song,

Mr. Beomseok Kang, Mr. Chansoo Kim, Dr. Yuan Meng, Dr. Hyunseok Kim, Dr. Hyunsung Kum, and Dr. Jaewoo Shim.

All of my research would not be possible without funding from the Japanese Society of Science Promotion (JSPS) through a Young Researcher Fellowship (DC1). Also I would like to deeply thank Tokyu Foundation for supporting my master studies that enabled me to continue academic journey for PhD studies. The solar cell device fabrication was done at the Miraikan, National Museum of Emerging Science and Innovation and I want to express my gratitude to all Miraikan members and staffs. Also, I would like to thank Prof. Esko. I. Kauppinen for providing high-quality CNT films that enabled highly efficient perovskite solar cell fabrication during my graduate studies.

My UTokyo experience has been particularly memorable because of all of the supportive and comforting friends and colleagues that I met through the years. I would like to thank to members of Korean Student Association and Korean Student Football Club in UTokyo. Also, I would like to express my gratitude to my great senpai, Prof. Minhyeok Lee, and friend, Dr. Byeongwook Jo who were very supportive during my UTokyo life.

Above all, I feel very grateful for my parents and families for their selfless support during my study abroad. I really thank to my girlfriend, Bella Lee, for endless support and encouragement during my PhD studies.

Finally, I would like to thank all other friends, colleagues and collaborators that I was not able to mention here specifically due to limitation of space and wish you all the best. Also, I was lucky enough to finish my PhD studies during COVID-19 situations with unseen supports from hardworking UTokyo staffs as well as government staffs that kept my student life safe. I feel very grateful for their support.

Table of Contents

Chapter 1:

Introduction

1.1 Introduction and overview of the thesis

Carbon nanotubes (CNTs), firstly experimentally found in 1993 by Iijima et al. [1], are a nano-carbon material with one-dimensional (1D) tubular structure made up of rolled-up graphene sheets. Owing to the unique physical properties from sp^2 nanocarbon system and their 1D quantum structure, CNTs have attracted much interest from various application field including electronics, mechanics, chemical engineering and so on [2]. In recent years, CNTs as for solar cell application has shown significant progresses as they can enable highly efficient and stable devices from their excellent stability [3] (both mechanical and chemical) and high carrier mobilities [4–6] compared to conventional materials such as organic materials and metals. Furthermore, CNTs can have direct-bandgap, broad spectral response, large absorption coefficient and fast response (~picosecond), which makes CNTs more attractive in solar cell application [7,8]. Large scale CNT synthesis, which was regarded as one of the main bottlenecks for CNT device integration has also been successfully achieved [9] so now it is technically available for CNTs to be employed in solar cell industries as long as they are shown to be more efficient compared to conventional materials in the industry. However, integrating as-grown CNTs into practical solar cell device is still challenging as they have both metallic and semiconducting CNTs which usually undermine the device performance as in general, each functional layer of solar cells has to be either metallic or semiconducting. Thereby, functionalization of CNTs such as dispersion,

separation, doping, etc. has been employed to achieve target properties of CNTs to be used in device. Nevertheless, we still lack the understanding of the role of functionalized CNTs in solar cell device as well as functionalization method itself.

In this thesis, functionalized CNTs and their integration into PV devices will be studied to better understand and clarify the role of functionalized CNTs when applied in PV devices. In addition, compatible integration techniques of functionalized CNTs into current PV fabrication process will be also investigated based on preparation of functionalized CNTs, device fabrication and characterization.

1.2 Carbon Nanotubes

To understand the carbon nanotubes, it is important to start with its most simple structure of "single layer". Single layer carbon nanotube, or single-walled carbon nanotubes (SWNTs) have a tubular 1D structure of a rolled-up graphene sheet. The geometry of a rolled-up graphene sheet identifies the electronic structure of SWNTs. Semiconducting SWNTs (s-SWNTs) are known to have band gap ranging from 0.5 eV to 2 eV (Fig. 1.2.1b) depending on a rolled-up structure, so called chirality defined by (n, m) chiral indices (Fig. 1.2.1a). Also, depending on the number of layers consisting of CNTs, they can be categorized into SWNTs, double-walled CNTs (DWCNTs), and multi-walled CNTs (MWCNTs).

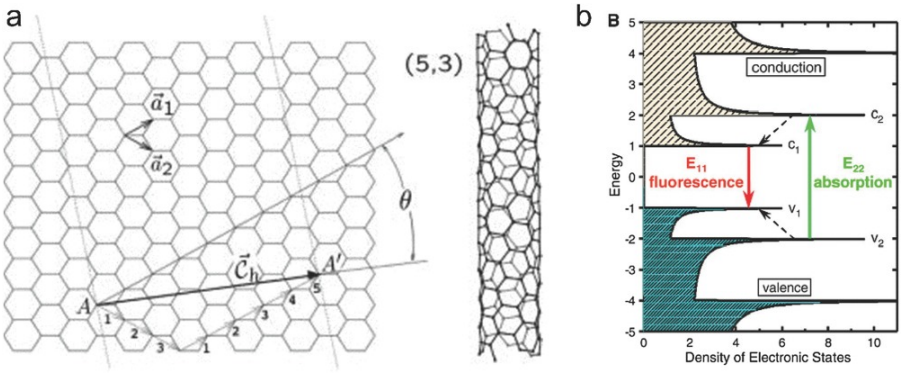

Figure 1.2.1 (a) Structure and vectors for defining a (5,3) CNT. (b)Typical density of states of a semiconducting CNT, showing strong peaks at the edges of the bands. Reprinted with permission from[7]. Copyright (2016) John Wiley and Sons/Wiley-VCH.

1.2.1 Structure-related optical properties of Carbon Nanotubes

To simplify the structure of carbon nanotubes, we can start from understanding SWNTs as a building block of entire carbon nanotube family. SWNTs can ideally be made of rolled-up sp^2-bonded graphene sheet (one layer of graphite) as a cylindrical structure. Physical properties of SWNTs can be decided upon the way how graphene sheet is rolled up, determining distinct properties of either semiconducting or metallic with specific chiral indices (n, m). The excellent optoelectronic properties of CNTs arise from their unique band structure, which is very important to understand their physical properties and thereby to design optoelectronic devices. It is known that statistically, in most SWNT growth, 2 / 3 of the SWNTs are semiconducting and 1 / 3 are metallic. Their band structure calculated through a single-particle tight binding model [10], and their typical density of states (DOS) are shown in Fig. 1.2.1.1a. Either type of SWNT has distinct peaks called van Hove singularities (VHS) that stem from two-dimensional quantum confinement. In m-SWNTs, finite DOS in between the lowest conduction and valence VHS can be found, and the lowest-energy ground-state electrons reside at the middle of the gap (the Fermi level). On the other hand, s-SWNTs possess no DOS in between the lowest-energy conduction and valence VHS. Thus, the lowest-energy electrons reside at the top of the valence VHS. Significant electron-hole binding energies associated with strong Coulomb interactions stabilizes bound excitons (electron-hole pair) with its binding energy (E_b) ranging of 0.2 – 0.5 eV [11] (Fig. 1.2.1.1b). Metal and semiconducting separation of SWNTs can be achieved by density gradient ultracentrifugation (DGU) [12], gel column chromatography (GCC) [13], aqueous two-phase extraction (ATPE) [14], and selective polymer extraction [15].

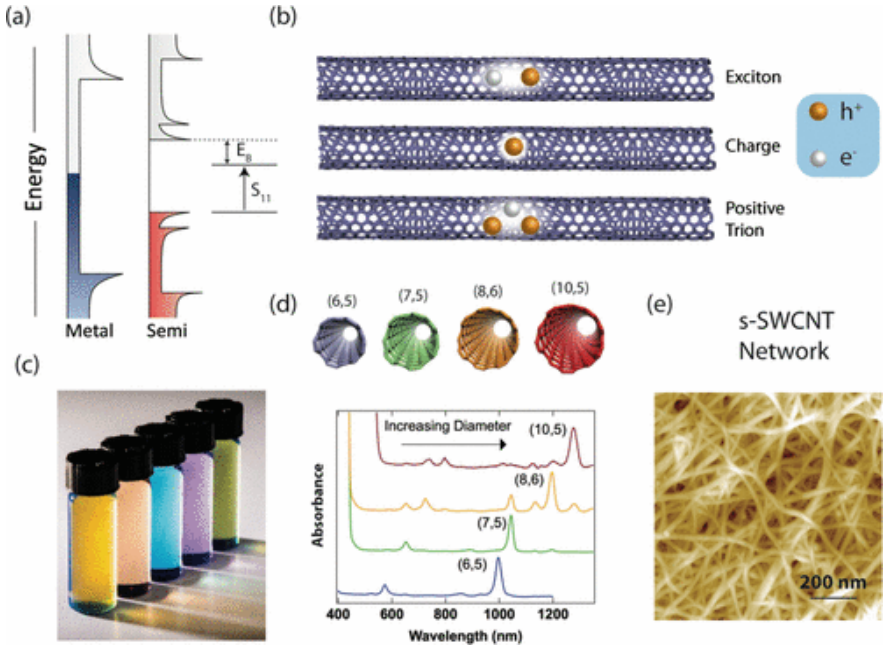

Figure 1.2.1.1 (a) Single-particle DOS for m- and s-SWCNTs. (b) Three different excited states of s-SWNTs. (c,d) Photos and absorption spectra of high purity s-SWNT inks prepared by polyfluorene extraction. (e) AFM images of a s-SWNT film prepared by ultrasonic spraying. Reprinted with permission from [16]**. Copyright (2017) American Chemical Society**

1.3 Metrology of Carbon Nanotubes

1.3.1 Electron Microscopy

As the size of CNTs is usually below the resolution of optical microscopy which is approximately the wavelength of visible light of 500-800 nm, electron microscopy is usually a more suitable way to microscopically observe CNTs. According to the wave-particle duality, the electrons with accelerated voltage can have wavelength shorter than visible light, thereby leading to higher microscopical resolution. SEM and TEM were used for the observation and characterization of CNTs.

1.3.1.1 SEM

Scanning electron microscopy (SEM) shown in Fig.1.3.1.1.1 is mostly often used to characterize the CNTs. SEM is rather used to observe CNT “bulk” such as forest,

network not to determine single CNT since its resolution is not high enough to observe single CNT. By scanning the surface of the sample with electron beams, SEM collects secondary electrons that are scattered from the sample with detectors and create the image of the sample. Imaging CNTs by SEM highly depends on the sample preparation, substrates, parameters in SEM (beam focus, acceleration voltage of electrons, stigma and etc.). SEM resolution can be achieved by around ~100 nm by up-to-date technology.

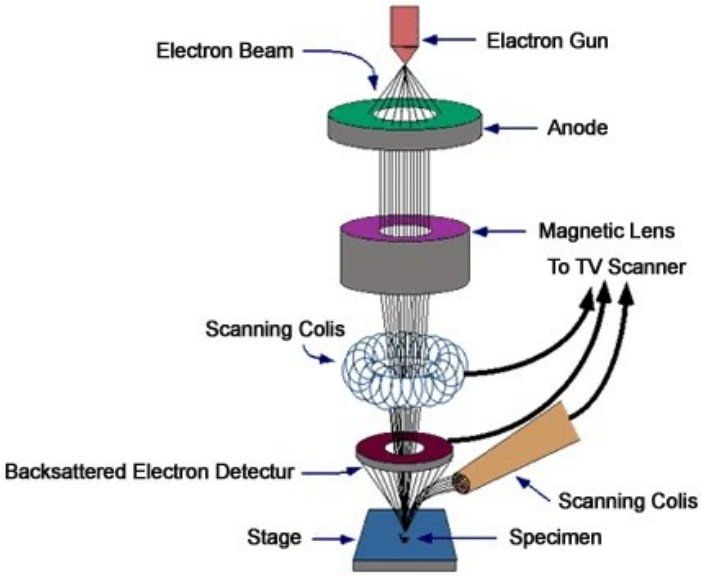

Figure 1.3.1.1.1 Schematics of Scanning Electron Microscope (SEM). Picture was acquired from https://sites.google.com/site/frontierlab2011/scannig-electron-microscope/principie-of-sem.

1.3.1.2 TEM

Transmission Electron Microscopy (TEM) is also frequently used observing CNTs to characterize single CNT information such as diameter, number of walls, defects, and etc. As TEM usually is used for higher resolution compared to SEM, TEM operation requires higher acceleration voltage of 60 -100 kV compared to that of SEM (1 - 10 kV). The high resolution of TEM achieved by higher acceleration voltage, enables more precise observation of CNTs with direct visualization of atoms, defects. On top of that, TEM can also provide electron diffraction pattern that enables to directly identify the chiral indices (n,m) of SWNTs.

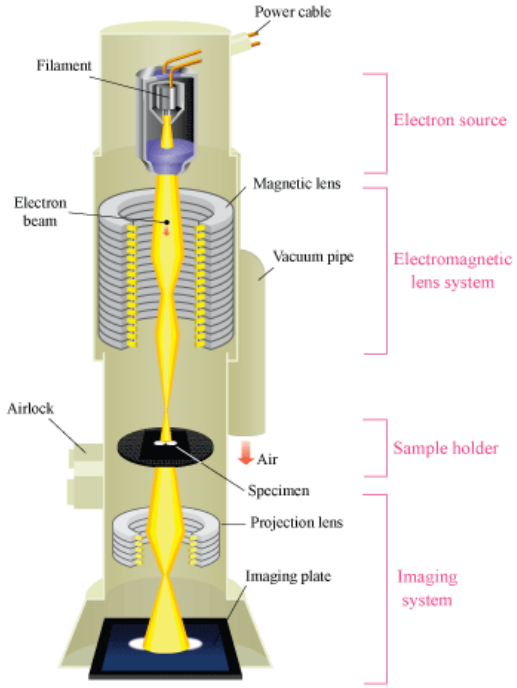

Figure 1.3.1.2.1 Schematics of Transmission Electron Microscope (SEM). Picture was acquired from http://www.hk-phy.org/atomic_world/tem/tem02_e.html.

1.3.3 Raman Spectroscopy

Raman spectroscopy is a convenient and powerful optical tool for characterizing carbon nanotubes. Raman spectroscopy utilizes the inelastic scattering of incident photon, so called "Raman scattering", coordinated with the lattice vibration and rotation from the material of interest. This scattered information is particular to each material and therefore can be used for identification or characterization of materials. In SWNTs, resonant effects of scattered photons are significant due to the van Hove singularities in electronic density of states arising from their quantum 1D structure. Especially, when the incident photon energy matches the optical transition energy of SWNTs, this resonance effects get significant and thereby even very small SWNTs where diameter is around ~1 nm can be detected by Raman scattering. SWNTs' Raman response can be characterized into several modes upon the chiral indices (n,m). G-mode or G-band of SWNTs appear around 1590 cm^{-1} which can also be detected on other sp^2 carbon family such as graphite, graphene and this arises from an in-plane mode of hexagonal

rings of graphite. In SWNTs, this G-mode splits into two peaks (G^+ and G^-) due to the rolled-up structures or chirality. At low frequency region, to ~ 500 cm^{-1}, Radial breathing mode (RBM) is detected that originates from radial expansion or contraction of the SWNTs. This mode is dependent on the diameter of SWNTs, so can be used to identify the diameter of SWNTs.

Raman spectroscopy characterization is dependent on the lasers with different wavelengths, so enables more detailed identification of nano-materials. But it can be also said that this measurement can be only achieved on available lasers, therefore not all SWNTs can be detected as long as there is restriction on available lasers.

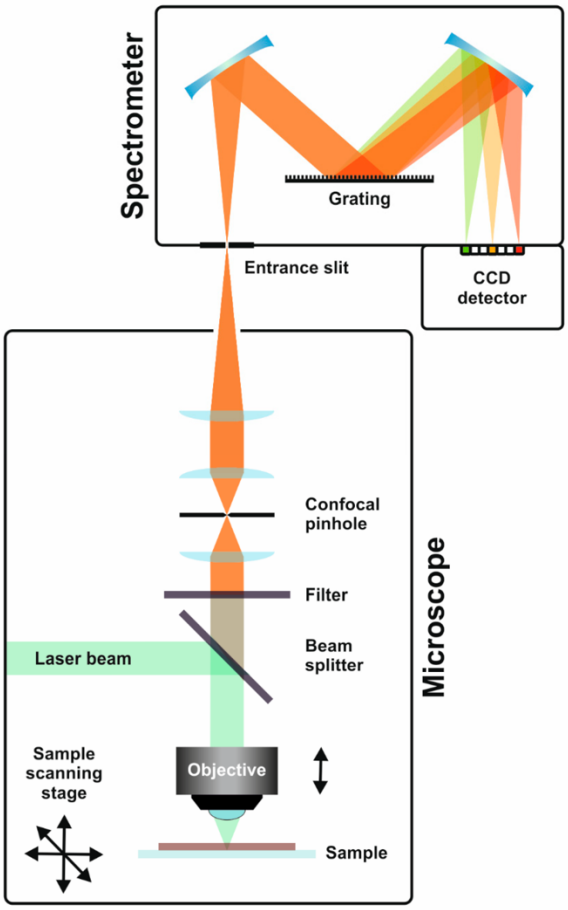

Figure 1.3.1.2.1 Schematics of Raman spectroscopy. Picture was acquired and reproduced from [17]**.**

1.3.4 Photoluminescence

Photoluminescence (PL) is a useful optical tool for especially characterizing the semiconducting carbon nanotubes (s-CNTs). s-CNTs have direct bandgaps that can produce efficient light emission. When s-CNTs are shed light, holes and electrons are excited. Some excited electron and hole pairs from s-CNT will recombine and emit light of which energy is same to the bandgap energy of s-CNT. We call this light emission to PL and this can be used for identifying the chirality of CNTs. This is because, when excitation energy is scanned through different wavelength, PL enhances when excitation energy matches the resonance with peaks in the density of states. Therefore, chirality of CNTs can be determined by measuring both the resonant energy and the emission energy from PL measurement.

1.3.5 Ultraviolet - visible - near infrared (UV-vis-NIR) Spectroscopy

In UV-vis-NIR region, CNTs possess characteristic peaks of additional absorption because of 1D van Hove singularities. Especially, s-CNTs exhibit three transitions between the transition in the electronic density of states S_{11}, S_{22}, and so on. Metallic CNTs (m-CNTs) have the first transition M_{11}. These inter-band optical transitions show characteristic features in UV-VIS-NIR region where S_{11} locates near 1700 nm, S_{22} locates near 1000 nm and M_{11}[18]. This indicates van Hove transitions of CNTs of different diameters. These peaks are usually not individually resolved, so to some extent, this absorption spectra can be dependent on the diameter distribution of CNT samples. UV-vis-NIR spectroscopy can be a useful tool to characterize the doping level of CNT samples by looking at changes in exciton bands in the NIR spectral range[19].

1.4 Potential, challenges and functionalization strategy of CNTs for photovoltaic application

1.4.1 Introduction of CNTs for photovoltaic application

CNTs with cylinder-like, 1D structures have attracted much attention for photovoltaic applications due to their physical (electrical and optical) properties, including the high carrier mobilities, tunable band gaps over a wide wavelength range, and high optical transparency along with low resistivity. They are also mechanically and chemically stable nanomaterials which enable long-term operation of photovoltaic devices as well as flexible applications. Not to mention, technically, they are made of earth abundant carbon (C) atoms so that makes no concerns about material sourcing. A variety of photovoltaic devices using CNTs have been reported in organic solar cells and inorganic solar cells. Utilization of CNTs in solar cell devices can be categorized into two types. First is as "charge transport channel" and second is "photoactive material". First has been more feasible considering the high exciton binding energy of CNTs and low absorption coefficient compared to conventional photoactive materials that limits efficient light energy conversion [20]. Also, CNTs as photoactive material require highly purified s-SWNTs, which is another challenging topic. Instead, as photoactive materials, they can be developed as "photodetector" to sense wide range of wavelengths which does not require high power generation [21]. CNTs as "charge transport channel" have showed a great potential as they can function as charge extractor and conductors. Their mechanical rigidity that enables flexible devices is an added bonus. This can be summarized into following Table 1.4.1.1.

Table 1.4.1.1 CNT application reported in PV devices and its feasibility

CNT application in PV	Required properties	What CNT have	CNT type	Conventional material	Potential (Reason)	Ref
Photoactive material	Suitable bandgap for light absorption	Tunable band gap	Highly pure semi	Si, Ge, perovskite, organic semiconductors	Low (Low PCE)	[22–24]
Charge extraction interface	Fast charge extraction and high mobility	High mobility, good coverage	Mixed or semi	Organic semiconductors, metal oxides	High	[25–27]
Transparent electrode	Optical transparency with low resistivity	High optical transparency (low parasitic absorption), low resistivity	Metal or semi-metal	Transparent conductive oxide (ITO, IGZO, ZnO, etc.), Metal nanowires, thin metal	High	[28–33]
Conductive electrode	Low resistivity, chemical stability	High mobility, chemical stability	Metal or semi-metal	Au, Ag, Al, etc.	Middle (Competitive counterpart)	[3,34,35]

1.4.2 Challenges of CNTs for solar cell application

Despite great optoelectronic properties of CNTs, CNT-based PV devices are still behind the conventional material system in terms of device performance. Followings are the problems that limits further device improvement in CNT-based PV devices.

- Co-existence of metallic and semiconducting CNTs after growth: Popular growth method of CNTs is done by chemical vapor deposition (CVD) with metallic catalysts. Usually, SWNT growth without any control yields ~2/3 of s-CNTs and ~1/3 of m-CNTS. When CNTs are used as electrical conductor, this metallic-semiconducting mixture limits electrical conduction forming Schottky barrier inside the mixture. On the other hand, when used as charge transport interface or photoactive material, this mixture leads to non-radiative recombination of carriers thereby undermining device performance.
- Transfer: Since it is difficult to directly grow CNTs on PV devices as CNT growth requires high temperature >300 °C, as-grown CNTs usually have to be transferred to PV devices. Current transfer requires wet process, or polymers which can degrade the target device leaving impurities.
- Length: As functional materials used in PVs are ~100 nm thick, bulk CNTs should be limited within ~100 nm thickness (Therefore few centimeter long vertically aligned CNTs are not relatively suitable for PV devices.). Also, the average length of CNTs grown by CVD is usually within ~few hundred micrometers, as their growth is limited by catalyst lifetime, neighboring CNTs, etc. Integrating as-grown CNTs into two-dimensional films, they result in having randomly oriented features inducing lots of contacts among CNTs. This number of contacts usually limit the efficient charge transfer, resulting in decreased conductivity compared to aligned film. The solution for this is to have long CNTs or aligned CNTs having less contacts among other CNTs.
- Defects: CNT growth usually accompanies lots of defects on CNTs and those

defects usually harm efficient charge transfer through CNTs. They can work as active sites for absorbing ambient chemicals which can degrade the underlying materials. Therefore, achieving highly crystalline CNTs is important to develop highly efficient CNT-based PV devices.

1.4.3 Functionalization of CNTs for photovoltaic application

To address the issues mentioned above, functionalizing CNTs was reported to be an effective way to better utilize or even improve the intrinsic CNT properties into PV devices. By designing proper functionalization method of CNTs, CNTs can possess desirable properties required for PSC incorporation.

- Dispersion: Dispersion of CNTs in solvents can be an efficient way to utilize CNTs produced in large scale, which could tackle the difficulty of transfer process of as-grown CNTs. For practical application of PV cells from lab to the industry, the compatibility of scaling up the fabrication process is extremely important. In this regard, CNTs now can be produced in the ton scale as powders, but they need to be dispersed to be used in disaggregated and more usable forms for PV applications. In addition, the dispersion of CNTs allows the separation of m-SWNTs and s-SWNTs. Thereby, functionalization of CNTs with suitable dispersing agent in target solution (polar or non-polar) is desired. Furthermore, the careful design of electronic structure and semiconductor property of dispersing agent can offer bonuses as CNT hybrid materials. Seo et al [27] and Lin et al [36] reported that by dispersing s-SWNTs dispersed with sodium deoxycholate and 4,6-di(anthracen-9-yl)-1,3-phenylene bis(dimethylcarbamate), those agents can be used as efficient dispersion surfactants as well as great Lewis base for forming Lewis adduct to improve crystal quality of PSCs. Habisreutinger et al reported that CNT/P3HT hybrid can work as a highly stable hole collection layer in PSCs[37].
- Doping: For CNT application for transparent electrodes in PV devices, the CNT

film should be highly optically transparent while highly electrically conductive. However, the optical transparency and electrical conductivity of CNT films are highly coupled to a trade-off relationship. Compared to conventional transparent electrodes including ITO, the reported sheet resistance of CNT films so far shows higher sheet resistance of ~few hundred ohm/square at high optical transparency over 90% (at wavelength of 550 nm). One of the reasons would be the existence of Schottky contacts among mixed s-CNTs and m-CNTs within the film. A doping strategy has been reported to be a successful approach to tackle this problem. Effective doping of CNTs can modify the Fermi level of CNTs resulting in lower band gap features similar to semi-metal. This offers the higher electrical conductivity of CNT film, minimizing the Schottky barrier as well as increasing the charge carrier density of s-CNTs. Strong oxidizing agents have largely been studied as effective p-type dopants for CNTs, including inorganic redox agents, such asH_2SO_4, HNO_3, $SOCl_2$, O_3 and $AuCl_3$ [38], as well as organic redox agents, such as bis-(trifluromethanesulfonyl)imide and perfluorinated polymeric acid Nafion [39,40]. Metal oxides such as MoO_3 and WO_3 with high work function greater than 6 eV are also reported to be effective p-type dopants for CNTs [41,42].

- Separation: To address the mixed metallic and semiconducting properties in as-grown CNTs, separation of metallic and semiconducting mixture of CNTs has been widely investigated as mentioned in Sec 1.2.1. Reports in separation of CNTs related to PV application usually refers to separation of s-CNTs for further utilizing their semiconductor properties. Selective polymer extraction method is popularly used in use of s-CNTs in PV application as selective polymer can also offer additional functionality to existing CNTs as well as separation ability. A wide variety of polyfluorene polymers are extensively used to extract s-CNTs as they can give high purities of s-CNTs and also very low metal impurities. This method also has very high yield and throughput which enables scalable deposition and fabrication of PV devices. By using this method, Blackburn et al reported that (6,5)-enriched s-SWNTs can efficiently extract charge and reduce recombination

when applied at the interface of HTL/perovskite[43]. They also reported that wrapping polymer does not affect carrier transport from perovskite to CNT/polymer hybrid material owing to extremely high mobility of CNTs.

- Van der Waals heterostructure: Recently, one-dimensional van der Waals hetero-structure with CNTs has been reported from our group [44]. This can provide additional properties on top of CNTs, but is still a very new concept to be investigated further. Qian et al reported that wrapping MoS_2 nanotubes with existing CNTs can efficiently function as hole transporters and conductors in PSCs [45].

1.5 Current application of CNTs on photovoltaic devices

1.5.1 Silicon Solar Cells

1.5.1.1 What is Silicon Solar Cell?

Silicon (Si) solar cell is the type of solar cell where its photoactive layer is made up of silicon. For almost three decades, Si-wafer-based PV devices are now dominant over the global PV market. Their high stability, long-lifetime, scalability and high PCE have led to the successful commercialization with a high performance / cost ratio over 90% market share. Despite fast advances in other PV domains (organic, perovskite and CIGS), continuous process optimization and new cell structures have made silicon to stay persistent as the leading PV technology. Theses involves a high efficiency designs with the early aluminum back surface field (Al-BSF) cells to the recently commercialized passivated emitter and rear cell (PERC). Furthermore, in the future, the scaled silicon heterojunction (SHJ) and interdigitated back contact (IBC) cells are the next strong candidates. They have reached very high PCEs close to the theoretical maximum of 29.4%, but new design needs complex structure. Dielectric passivation with SiO_2, Al_2O_3, SiN_x, and a-Si:H have become a very important step and these need high-vacuum or high temperature process for thin-film deposition. Furthermore,

carrier-selective contacts need doping of bulk silicon or doped-thin film. Doping of bulk silicon is the most well-established step to make a p-n junction. This is achieved by high temperature diffusion process with boron/phosphorous gas (toxic and dangerous) or ion implantation to fabricate p^+ or n^+ regions near wafer surface. Thin a-Si films are doped with plasma enhanced CVD (PECVD) with boron/phosphorous gas. Theses passivation step result in high fabrication cost, which now limits successful industrialization. So now, further decrease in fabrication cost (easy process, cheap materials) with high PCE is a key target to be achieved.

1.5.1.2 CNTs in Silicon solar cell

By far, CNTs in Si solar cells have been mainly used as transparent conductive thin film electrodes interfaced with silicon substrates. They are known to form Schottky junction at CNT-Si interface which can separate electron-hole pairs generated at the silicon. CNT film with high optical transparency and high electrical conductivity is desired for maximizing the light absorption while offering a low resistance for the carriers to reach metallic contacts. To date, the highest PCE achieved by CNT-Si solar cell as CNT functioning as transparent electrodes is 18.9% with active area of $1cm^2$[46]. Usually, in CNT-Si solar cell with p-type CNTs / n-type silicon, holes are collected by the CNTs and the electrons by the silicon. Recently, B. Flavel et al reported CNT/polymer hybrid material can efficiently function as passivated charge selective contacts that can be spin coated directly on to silicon[5]. This method needs no high temperature, vacuum process and deposition of dielectric layer.

1.5.2 Perovskite Solar Cells

1.5.2.1 What is Perovskite?

"Perovskite", first named after a Russian scientist Lev Perovski, was originally a term to refer the mineral out of calcium titanium oxide ($CaTiO_3$), first discovered in Russia. This word, "perovskite" has been extended to describe the compound with a

certain crystal structure of ABX_3 (Figure 1.5.2.1.1.1). Materials of the perovskite structure have been studied in many applications including the PV industry.

Researchers in academia and industry have been trying to make solar cells using perovskite materials for a decade. In such a compound with the ABX_3 structure, A is a monovalent cation, B is a divalent cation, and X is a divalent anion, so the more explicit structure expression is $A^{+}B^{2+}X_3^{-}$. While $CaTiO_3$ is a natural compound, there are many recipes to artificially synthesize molecules with the perovskite structure. To form a compound with stable perovskite structure, the relative ion sizes of A, B and X must be within a certain range. Options explored for PV applications are shown in Fig. 1.5.2.1.1.1. Note that each symbol (A, B, and X) can use one of the listed optional materials, which results in a 'neat' perovskite, or a combination of multiple choices that is referred as an alloyed perovskite. Perovskite solar cell (PSC) is a type of solar cell which has perovskite material as its light-harvesting active layer. For instance, Helmholtz-Zentrum Berlin made a perovskite solar cell with the material $Cs_{0.05}(FA_{0.77}MA_{0.23})_{0.95}Pb(I_{0.77}Br_{0.23})_3$. A, on top of a silicon solar cell, which together realized an efficiency record of 29.15% in 2020[47].

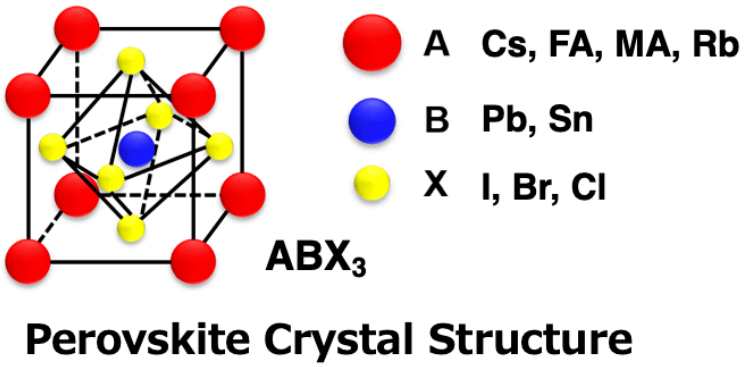

Figure 1.5.2.1.1.1 Schematics of perovskite crystal structure.

PSCs have the potential to achieve lower production cost and higher PCE compared with the current dominant silicon solar cells. The fundamental process of PVs is that an electron's transition from one state to another. When electron obtains enough energy from a photon (light) to jump from a 'restricted' state (valence band) to an 'excited' state (conduction band), it can flow in a specific direction within an built-in electrical field and generate electricity. When such electrons travel inside the solar cell, it is likely

to relax to the restricted state, releasing energy by emitting heat, or transferring energy to other excited electrons. In this case, the electron cannot contribute to electricity anymore. So, it is desirable for electrons to have much 'excitement' and less 'relaxation.'

Perovskite materials involve atoms with electronic structure different from that in silicon and this grants two features to perovskite solar cells. First, perovskite can absorb light very efficiently compared to silicon, so a PSC only needs a layer of about 0.3 micrometers (um) thickness to absorb the incident lights. This is impressive compared to 170-180um thickness for silicon wafers, and significantly reduces material cost. Second, perovskite is defect-tolerant that caused by impurities in the bulk material compared to Si. As a result, the perovskite material needs purity of only 90%, and no additional purification process is needed after solution mixing. This also saves material processing cost. In contrast, the Si material needed for solar cell application needs conversion of metallurgical-grade silicon of 98% purity to 99.9999% purity.

Other cost-saving features stem from the fabrication method. Unlike the manufacturing process for silicon solar cells, that requires reactions at temperatures higher than 1000°C to dissolve silicon, PSCs can be fabricated using solution processes in a line at temperatures less than 150°C. Fewer fabrication steps and low temperature benefits less capital investment on factories, labor cost and energy consumption,

The theoretically achievable PCE is directly related to the energy bandgap (E_g), and this is called Schokley-Quiesser (SQ) limit [48]. If a photon carries energy greater than E_g, the extra will be wasted as heat. If the photon's energy is lower than E_g, it cannot excite the electron from the valence band. A crystalline silicon solar cell is basically a p-n junction, with 'p' and 'n' referring to excessive holes and excessive electrons, respectively. For a solar cell made of one semiconductor material and composed of a single-junction solar cell, there exists the optimal choice of bandgap, which can give highest theoretical PCE. The optimal bandgap for highest possible PCE depends on the spectrum distribution of solar spectrum. For the standard spectrum at the earth surface, AM 1.5, silicon has already reached close to the optimal E_g value. However, its actual achievable efficiency is undermined by carrier recombination related to bulk impurities,

to which perovskite materials are less sensitive. More importantly, perovskite materials can be designed and synthesized to achieve the optimal E_g. Therefore, PSCs could achieve higher efficiency than silicon cells when both are of single-junction structure. The highest laboratory efficiency record of PSCs available in literature is 24.4% with $(FAPbI_3)_{1-x}(MC)_x$,where MC is an abbreviation meaning MDA^{2+} and Cs^+ were mixed in equimolar amounts [49]. Although this is still lower than the 26.7% achieved for silicon cells [50], it is a very exciting result considering the short exploration history of perovskites from 2009 [51].

An ideal solar cell would have multiple junctions, so that each photon with different energy can be fully utilized by the material with the corresponding bandgap. Thus, the theoretical PCE-limit increases when more junctions are incorporated. In such a tandem-junction solar cell, there exists an optimal bandgap for each junction to achieve the highest total efficiency. The bandgap of perovskites can be modified by changing the chemical composition, and this is very achievable by preparing desired precursor solution with target composition ratio. With enough flexibility of recipe engineering, perovskite can provide the desired bandgap. Because most popular perovskite composition exhibits bandgaps higher than silicon, they are usually incorporated as the top junction materials for perovskite/Si tandem cells. In 2020, Oxford PV based in UK achieved a record efficiency of 29.52% on such perovskite/Si tandem cell. Ideally, it is possible to obtain both lower fabrication cost and higher PCE simultaneously on PSCs compared with crystalline silicon cells. However, in reality, single-junction perovskite PV devices can be produced in lower cost than silicon but with lower efficiencies. Perovskite/Si tandem cells are more efficient than silicon but also more expensive.

1.5.2.2 CNTs in perovskite solar cells

CNTs have been extensively employed to tackle many challenges for PSCs. In the last years, numerous reports have been made to utilize CNTs as a wide range of functional components for achieving highly efficient PSCs. Followings are the representative function of the CNTs in PSCs.

- Transparent conductive electrodes: CNTs provide exceptional electrical

conductivity, mechanical rigidity and flexibility, and optical transparency which benefits the usage of CNTs as transparent electrodes. Application as transparent conductive electrodes were most popular among the other application of CNTs in PSCs since they can be used as long as high electrical conductivity and high optical transparency are achieved.

- Electron transport layers: Electron transport layer (ETL) plays an important role to quickly and effectively separate the photogenerated charges and finally transport them to the close electrical contact. It was reported that CNTs can be added on top of popular ETL TiO_2 can facilitate fast charge transfer that can reduce trap-induced nonradiative recombination [52]. Also, addition of CNTs were reported to reduce the work function, which benefit the V_{oc} improvement when applied on top of SnO_2 ETL layer [53].
- Additive in perovskite layers: The film quality of perovskite light absorbers including defects, charge transport ability, morphology, and optical property has a tremendous impact on the PCE and stability of PSCs. Perovskite films fabricated by solution process usually consist of small grains with a lot of grain boundaries because of the fast crystallization process. Grain boundaries can work as trap or defect sites for nonradiative recombination and undermine the device performance of PSCs. Therefore, achieving large grain size and passivating the grain boundaries are important to fabricate highly efficient PSCs. Several approaches have been employed to engineer and control the crystallization process to improve the crystal quality. Especially, additive approach has been reported to be an effective method to improve the morphology of perovskite films. CNTs with appropriate functionalization have been reported to be useful as beneficial additives by controlling nucleation and crystallization kinetics during film formation of perovskite [27].
- Hole transport materials: Hole transport materials (HTL) in PSCs should have favorable energy level alignment and hole mobility to extract and transport (or efficiently block unwanted charges, which are electrons) generated electron-

hole pairs with regard to perovskite absorber. In addition, they should be thermally and chemically stable to be resilient to external degradation factors including water and oxygen. Spiro-OMeTAD is the most popular HTM, but it requires dopant to enhance its intrinsic low charge mobility and conductivity. Lithium salts are the most commonly used dopants for Spiro-OMeTAD, but owing to their hygroscopic property, they result in performance when exposed to ambient atmosphere. Thus, investigating potential HTL or HTL additive with excellent charge extraction ability and high mobility are highly in need for achieving PSCs with high PCE and stability. Arising from their intrinsic p-type nature, favorable work function and great stability, CNTs have been reported to perform very good as both HTL and HTL additives [26,54,55].

- Back electrodes: Conventional PSC fabrication involves the use of expensive back metal electrodes, such as Au or Ag. Nevertheless, their high cost and vacuum process of depositing noble electrodes should be replaced for large-scale production. Moreover, their migration across the charge transport layer into perovskite absorber decreases long-term stability of PSCs. Developing facile alternative back electrodes is highly desired for the successful commercialization of PSCs. CNTs are highly conductive, hydrophobic and thermally stable. They have been reported to efficiently function as back electrodes for PSCs providing both high efficiency and stability[56].

1.6 Metrology of Photovoltaic devices

1.6.1 J-V Characterizations

The performance of fabricated solar cells is characterized under AM 1.5G (1 sun) illumination by current-voltage (J-V) measurement or J-V sweep and corresponding photovoltaic parameters are calculated to characterize photovoltaic performance of the fabricated devices. J-V measurement under 1 sun gives the most basic solar cell features of power conversion efficiency (PCE), fill factor (FF), open-circuit voltage (V_{oc}), short-

circuit current (J_{sc}), series resistance (R_s) and shunt resistance (R_{sh}) (Fig. 1.6.1.1, Fig. 1.6.1.2). These six parameters indicate the basic performance of the solar cell. Furthermore, maximum power point of the solar cell device can be calculated and used on further maximum power point tracking measurement on perovskite solar cells [57]. The dark current of the device is measured under no light (dark) condition. Dark current characterization can give the leakage current of the solar cell devices and also be correlated to shunt or recombination resistance of the solar cell.

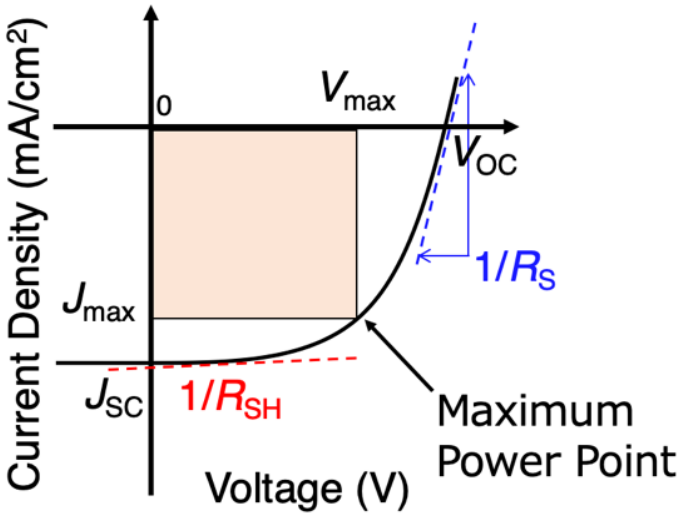

Figure 1.6.1.1 J-V characterization of solar cells

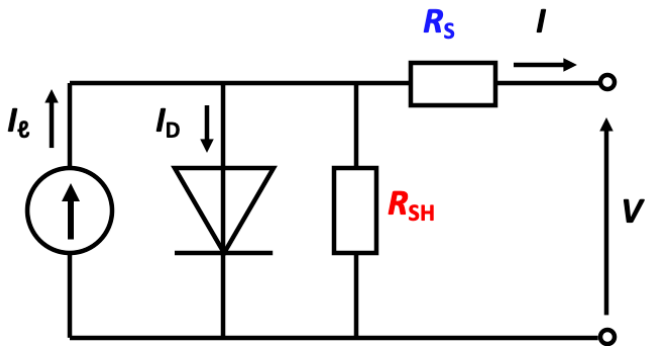

Figure 1.6.1.2 Equivalent circuit of J-V characterization of solar cells

1.6.2 Four-Point Probe measurement

The sheet resistance of CNT films was measured by a four-point probe method. Four-point probe is usually used to obtain resistive properties of thin films. If the thickness of a thin film is already known, the sheet resistance obtained from four-point probe

measurement can be used to derive the resistivity of the material. Van der Pauw (VdP) method is a commonly used technique when using four-point probe measurement. VdP method is known to have ability to measure the properties of a sample regardless of the shape, as long as the sample is two-dimensional, solid with no holes, and the contact electrodes are placed on the very corner. VdP method gives an average resistivity of the sample, whereas counterpart linear four point probe method gives the resistivity in the sensing direction. Therefore, VdP method becomes more effective when measuring anisotropic material (such as 1D tubes that have high carrier mobility along the tube axis).

1.6.3 XRD

X-ray diffraction (XRD) is a powerful method that uses diffraction of incident x-ray on to samples to analyze the geometrical arrangements of the constituents in the material of interest, especially in crystalline materials. This provides the information of atomic level distances, extraction of symmetries, densities, temperature and compositional dependent phase transitions as well as crystallite size and orientation of polycrystalline thin films. XRD works by irradiating a sample (either thin film or powder) with incident X-rays and then count the intensities and scattering angles of X-rays that come out of the material. Crystal atoms usually scatter incident X-rays mainly through interaction with the electrons in atoms. This can be referred to elastic scattering. A regular array of atoms produce a regular array of spherical waves and majority of them cancel each other out via destructive interference. However, some of them add constructively in a few specific directions, which are determined by Bragg's law

$$2dsin\theta = n\lambda \quad (1.6.3.1)$$

Where d is the spacing between diffracting planes, θ is the incident angle of X-rays, n is an integer, and λ is the wavelength of the beam. The specific directions come into view as spots on the diffraction pattern, so called reflections. Therefore, X-ray diffraction patterns result from electromagnetic waves hitting on a regular array of

atoms. X-rays are used to make the diffraction pattern because their wavelength, λ is usually as the same order of magnitude as the spacing d, between the crystal planes that is usually 1-100 angstroms.

1.6.4 XPS

X-ray photoelectron spectroscopy (XPS) is a surface characterization method that analyze a sample to a depth of 2 to 5 nm (depending on the incident X-ray energy). XPS shows which chemical elements are present at the sample surface and the nature of the chemical bond that exists between present elements. XPS can detect most of the elements but hydrogen and helium. XPS is conducted in ultrahigh vacuum conditions that enable accurate surface interrogation. Irradiating a sample with x-rays of sufficient energy excites electrons in specific bound states. During the measurement, sufficient energy of X-ray is irradiated on sample to break the photoelectron away from the nuclear attraction force of an element. Some of the ejected photoelectron scatter inelastically through the sample, while others experience prompt emission with no energy loss escaping into vacuum. Once escaped electrons are in the vacuum, they are collected by an electron detector that measures their kinetic energy. An electron energy analyzer calculates an energy spectrum of intensity (counts, a number of photo-ejected electrons versus time) versus binding energy (eV, the energy they had before leaving the atom). Each prominent peak on the spectrum corresponds to a specific element, such as 284.6 eV for carbon (C) and 532.5 eV for oxygen (O). Peak intensities can be referred to atomic concentration of the sample and also each specific peak can be deconvoluted to what type of chemical bonds they possess (i. e. C-O, C=O for carbon).

1.6.5 EQE

As a solar cell is a device that converts the sunlight into electrical energy by photovoltaic effects, measuring the efficiency of this conversion process is very

important to understand the fundamentals of a solar cell device. This efficiency is called as quantum efficiency (QE). There are two types of QE: 1. External Quantum Efficiency (EQE) and 2. Internal Quantum Efficiency (IQE). EQE is acquired by the ratio between a number of collected charge carriers by solar cells with the number of incident photons. IQE only considers the absorbed photons, in other words, they do not consider the reflection at the solar cell surface. This explains why IQE values are always higher than EQE values. The spectral response measurement first needs to be done before measuring the EQE value. Spectral response is a ration between the current generated by the solar cell and the incident power. The relationship between EQE and spectral ratio can be written as:

$$EQE(\lambda) = \frac{hc}{q\lambda} \cdot Spectral\ response \quad (1.6.5.1)$$

Where h is Planck's constant, c is the speed of the light, q is the electronic charge, and λ is the wavelength. The EQE depends on both the absorption of the light and the collection of excited carriers. Once a photon has been absorbed and generated an electron-hole pair, efficient separation and collection at the junction is needed. A good solar cell has less charge recombination and high EQE across the wavelength spectrum of interest.

1.6.6 PYS

Photoelectron yield spectroscopy (PYS) is a technique to measure the ionization energy of the sample (work function in the case of metals) through photoemission process. A sample surface is irradiated by tunable ultraviolet light, and the number of emitted photoelectrons is collected through detectors. The quantum yield of photoelectron which corresponds to the number of emitted photoelectrons per photon absorbed, is measured as a function of incident photon energy. When incident photon energy becomes higher than the threshold ionization energy during scan, the quantum yield of photoelectron starts to increase. Therefore, by checking the threshold energy from the spectrum, the ionization energy can be evaluated. PYS has some advantages

compared to conventional photoelectron spectroscopy. They can be measured in atmospheric environment and charge-up problem of the sample is negligible.

1.6 Motivation and Purpose of the Thesis

Owing to CNTs' excellent electrical and optoelectrical properties, CNTs have been widely studied as a key material for PV applications. In principle, CNTs can be employed into all elements of a solar cell, from the photosensitive component to carrier selective contacts, passivation layers and transparent conductive electrodes. Also, their great mechanical and chemical stability can enable the fabrication of flexible solar cells and long-term operation. However, as discussed in Chapter 1.4.2, as-synthesized CNTs cannot be easily integrated in solar cells. These challenges have hindered the industrial uptake of CNTs as they face strong competition from alternative materials that already exist. In this regard, functionalization of CNTs such as separation, doping, dispersion and van der Waals heterostructuring have been extensively employed for better integration of CNTs into PV devices. Nevertheless, majority of the reported studies were somewhat limited to demonstrating performance increase by employing new functionalized CNTs compared to conventional materials. This is because CNT functionalization (including CNT growth) and device fabrication are usually studied in separate research groups, thereby their link was not fully studied nor described. This lacks the fundamental understanding of functionalization method itself as well as roles of functionalized CNTs in PV devices. Therefore, this thesis will deal with CNT functionalization and its PV device integration so that CNT-based PV devices can be developed in a cooperative manner.

1.7 Organization of the Thesis

This thesis begins with Chapter 1, a brief introduction of carbon nanotubes, their relevance in current PV technologies, challenges and potential opportunities. Experimental metrologies for both CNTs and PV devices are also introduced with its

brief mechanisms. Chapter 2 discusses about new application approach of functionalized s-SWNTs to improve crystal quality of perovskite film. This paves a new way for research community that dispersed CNTs with surfactant agent can be efficient additives into perovskite film. In Chapter 3, a highly efficient semi-transparent solar cell enabled by MoO_3 doping for perovskite/silicon tandem application will be discussed. This mainly discuss about an efficient doping of CNT top electrodes with high work function metal oxide MoO_3 and their compatibility in conjunction with bottom silicon solar cells. Finally, the thesis is summarized by the impacts and contributions to the research community.

Chapter 2:

Grain size control and passivation of perovskite films with s-SWNT additives for highly efficient perovskite solar cells

2.1 Research Background and Introduction

Although PSCs are considered to be promising next-generation solar cells, further breakthroughs in terms of achieving higher PCE are necessary to supersede conventional silicon solar cells. With this regard, the control of grain size and passivation of its defective boundaries of perovskite crystals are critical to obtain high PCE.[58,59] To enlarge the grain size, inducing homogeneous nucleation and retarding perovskite crystal growth are needed. [60] Thus, polymer templates [61,62] and various anti-solvents have been investigated to accomplish these. For the passivation of grain boundaries, Lewis adduction formation at the grain surfaces has a favorable effect as the structural disorder in the interface of the grains induces shallow trap states, which lead to non-radiative recombination of charge carriers. [63] Ideally, technologies for controlling the grain size and passivating their interfaces at the same time are in need. [64,65]

Over the last two decades, CNTs have generated a lot of excitement among researchers for their device applicability owing to their exceptional charge carrier transporting properties, and outstanding chemical and mechanical stability. In

particular, s- SWNTs with a direct bandgap of up to 2 eV represent high conductivity along the tube axis, favorable for charge-transporting media in PSCs. [66,67]

Recently, fullerenes have been reported to function as charge-transporters in PSCs. [68] However, fullerenes have inferior carrier mobility and stability than that of SWNTs that they cannot be considered an ideal choice of materials. [3] To date, there has been one report on the application of purified s-SWNTs in PSCs, where s-SWNTs were used as a charge extracting material next to a perovskite photoactive layer. [43] Another close application is sulfonated multi-walled carbon nanotubes as crystal growth templates embedded in a perovskite film, but the CNTs were not purified as semiconducting as they were multi-walled. [69]

Herein, we report purified s-SWNTs dispersed in water functioning as both the perovskite crystal growth templates and charge transporters inside a perovskite film, increasing the PCE of PSCs from 18.1% to 19.5%. Sodium deoxycholate (DOC) surfactants (dispersion agent) were employed to collect s-SWNTs bound to agarose gel in the process of separation. The carbonyl groups in DOC surfactants formed Lewis adducts with perovskite precursor PbI_2 to function as growth templates and passivators, resulting in large crystal size and reducing trap sites, respectively. Since s-SWNTs were dispersed in water for a purification process, a small amount of water was added into a $CH_3NH_3PbI_3$ ($MAPbI_3$) solution. To elucidate the role of added water, we fabricated water-added PSCs for a comparison. The added water improved the quality of the perovskite crystal grains in terms of homogeneity. With the presence of s-SWNTs, the size of crystal grains and mobility of the perovskite film improved. This was verified by microscopic techniques, such as scanning electron microscopy (SEM) and in-situ transmission electron microscope (TEM), and various charge kinetics characterizations. However, there was a limitation in the exploitation of s-$SWNT_{(aq)}$; it was found that 2 wt% of s-$SWNT_{(aq)}$ was the optimal amount and higher concentration induced the decrease in device performance. We ascribed this to the limited purity of s-SWNTs and

low mobility of DOC surfactants. Therefore, this leaves us with the room for further enhancement by the purity of s-SWNTs and the mobility of surfactants.

2.2 Materials and Methods

2.2.1 s-SWNT Dispersion Preparation

Preparation of s-SWNT dispersion was performed according to the literature [70,71]. The SWNTs synthesized by high-pressure carbon monoxide processing (HiPco, raw soot, RO513, NanoIntegris, 1.0 – 0.3 nm in diameter) were used in this study. Dispersions of the SWNTs was prepared by dropping 1 mg mL^{-1} of the as-prepared SWNTs in 1% SDS (99%, Sigma–Aldrich) solution and then ultrasonicating the mixture using a tip-type ultrasonic homogenizer (Sonifire 250D, Branson) for 3 h under cooling at 15 ℃. The solution was then centrifuged to remove bundles and impurities (210,000 x g for 30 min at 25 ℃). The resulting supernatant was collected as a dispersant of surfactant-coated SWNTs. A chromatography system (AKTA, GE Healthcare) equipped with a column packed with agarose gel beads was used for the separation of metallic and semiconducting SWNTs. After equilibration of the column with 1% SDS solution, the SWNT dispersion was applied. Metallic and semiconducting SWNTs were obtained as unbound fraction in 1% SDS and bound fraction eluted by 1% DOC, respectively.

2.2.2 Perovskite Solar Cell Fabrication

ITO patterned glass substrates were cleaned and sonicated with detergent, distilled water, acetone, and isopropanol in an ultrasonic bath for 15 min, respectively. The cleaned substrates underwent the UV-ozone for enhanced wettability. Thirty millimolar $SnCl_2 \cdot 2H_2O$ (Aldrich, >99.995%) solution was prepared in ethanol (anhydrous, Fujifilm Wako Pure Chemical Co.) as a precursor solution for deposition of a compact

SnO_2 layer. The solution was filtered by a 0.2 μm syringe filter, followed by spin-coating on the cleaned substrate at 3000 rpm for 30 s. The spin-coated film was annealed at 150 °C for 30 min. After cooling down to room temperature, another cycle of the spin-coating process was repeated, which was followed by annealing at 150 °C for 5 min and 180 °C for 1 h. The SnO_2-coated ITO glass was treated with UV-ozone before spin-coating of the prepared perovskite solution. Perovskite solution was prepared as follows. For the $MAPbI_3$ Solution, CH_3NH_3I (TCI), PbI_2 (TCI), and anhydrous dimethyl sulfoxide (TCI) (molar ratio 1:1:1) were mixed in anhydrous *N,N*-dimethylformamide (TCI) with a concentration of 50 wt%. The solution was filtered through a 0.45 μm poly(tetrafluoroethylene) filter before use. For the water-added $MAPbI_3$ solution, 2 wt% pure water (Fujifilm Wako Pure Chemical Co.) was added into the prepared $MAPbI_3$ solution. The solution was filtered through a 0.45 μm poly(tetrafluoroethylene) filter before use. For the s-SWNT-added $MAPbI_3$ solution, 2 wt% semiconducting SWNT dispersion was added into the prepared $MAPbI_3$ solution. The solution was filtered through a 0.45 μm poly(tetrafluoroethylene) filter before use.

Then, 25 μL of perovskite precursor solution was spin-coated onto the SnO_2 layer at 3000 rpm for 30 s, with 0.5 mL of anhydrous diethyl ether slowly dripped onto the substrate 10 s after the start of the spin-coating process. Next, the film was annealed at 100 °C for 10 min to obtain a dense brown $MAPbI_3$ film. The spiro-MeOTAD solution was prepared by dissolving 85.8 mg of spiro-MeOTAD (Merck) in 1 mL of chlorobenzene (anhydrous, 99.8%, Sigma-Aldrich) which was mixed with 33.8 μL of 4-tert-butylpyridine (96%, Aldrich) and 19.3 μL of Li-TFSI (99.95%, Aldrich, 520 mg/mL in acetonitrile) solution. The spiro-MeOTAD solution was spin-coated on the perovskite layer at 3000 rpm for 20 s by dropping 17 μL of the solution during the

spinning. Finally, a 70-nm-thick Au anode was fabricated by thermal deposition at a constant evaporation rate of 0.05 nm s^{-1}.

2.2.3 Characterizations

The *J*−*V* curves were measured using a software-controlled source meter (Keithley 2400 Source-Meter) under dark conditions and the simulated sunlight irradiation of 1 sun (AM 1.5G; 100 mW cm^{-2}) using a solar simulator (EMS- 35AAA, Ushio Spax Inc.) with an Ushio Xe short arc lamp 500. The source meter was calibrated using a silicon diode (BS-520BK, Bunkokeiki). The SEM analysis of the perovskite films was performed using an S-4800 (Hitachi). The TEM images are taken by JEM-2010F (JEOL Ltd.) with a thermal field emission gun operated at 200 keV. The selected area electron diffraction (SAED) patterns are recorded by a charge-coupled device at a camera length of 60 cm.

Shimadzu UV-3150 was used for the UV−Vis−NIR measurement. The PL measurement for the chiral mapping and the films were obtained by a home-built micro-PL system with a supercontinuum laser as the excitation (wavelength: 450–2400 nm) and an InGaAs multiarray detector for detecting the emission (900–1600 nm in wavelength). Topography images were recorded by using an atomic force microscope (AFM) operating in tapping mode (SPI3800N, SII). The grazing-incidence XRD 2θ scans were performed on a Jordan Valley D1 diffractometer with a copper Kα1 radiation and a parallel beam source. In the 2θ scans, the scattering angle 2θ between incident beam and diffracted beam changes, whereas the incident angle ω between the incident beam and the sample surface is fixed at 1°. The valence band and the Fermi levels measurements were performed using Riken Keiki PYS-A AC-2 and Kelvin probe spectroscopy in air (ESA), respectively. The photo-emission measurements were performed using XPS (PHI5000, Versa Probe) with monochromatic Al Kα radiation. Fermi levels were measured with a Riken Keiki PYS-A AC-2 photoelectron

spectrometer in air. The incident photon-to-current conversion efficiency (IPCE) measurement system consisted of an MLS-1510 monochromator to scan the UV−Vis spectrum. A source measurement unit was used to record the current at each specific wavelength. Two home-made systems based on a Seki Technotron STR-250 laser Raman system (excitation wavelength of 633 nm and 785 nm) and an inVia Raman microscope (Renishaw) were used for Raman measurements. Solartron SI1287 Electrochemical Interface and Solartron 1255B Frequency Response Analyzer were used for the Impedance Measurement. FT-IR spectra were obtained with a Nicolet Avatar 370 DTGS spectrometer which was fitted with a Smart Performer single-reflection accessory and a flat plate with a ZnSe crystal. For the TRMC measurement, thin film samples were prepared on a quartz plate. The sample was put in a resonant cavity and probed by continuous microwaves at *ca.* 9.1 GHz. The laser excitation from an optical parametric oscillator (OPO, Continuum, Panther) seeded by third-harmonic generation of a Nd:YAG laser (Continuum, Surelite II, 5−8 ns pulse duration, 10 Hz) was set at 500 nm. The photon density (I_0) varied from 1.28×10^{11} to 6.42×10^{14} photons cm^{-2} $pulse^{-1}$. The photoconductivity transient $\Delta\sigma$ was converted to the product of the quantum efficiency of the charge-carrier generation at the pulse end (φ) and the sum of the charge carrier mobilities, $\Sigma\mu$ ($=\mu^{+}+\mu^{-}$), by $\varphi\Sigma\mu = \Delta\sigma(eI_0F_{\mathrm{Light}})^{-1}$, where e and F_{Light} are the unit charge of a single electron and a correction (or filling) factor, respectively.

2.3 Purified s-SWNTs for PSC application

Metallic carbon nanotubes function as recombination sites in perovskite films and form Schottky junctions with neighboring s-SWNTs. Therefore, it is important that we use highly pure s-SWNTs if we are to use them inside the perovskite film.[27,72,73] We obtained highly pure s-SWNTs by agarose gel chromatography, where the s-SWNTs were selectively attached to the gel in 1% SDS and were eluted by 1% DOC (Fig. 2.3.2). The photoluminescence (PL) mapping (Fig. 2.3.1a and 2.3.3) and the corresponding chirality mapping (Fig. 2.3.1b and Table 2.3.1) show that there are s-SWNTs in the attained solution with the major chirality being (9,4). The UV-Vis-NIR spectrum with strong S11 and S22 transition peaks represent the high purity of s-SWNTs (Fig. 2.3.1c). Moreover, the Raman spectra obtained from 785 nm and 633 nm excitation laser lines substantiate the s-SWNT purity (Fig.2.3.1d). Atomic force microscopy (AFM) images of the s-SWNTs drop-cast on glass substrates show that the SWNTs are longer than 1 mm and possess an entangled geometry. This implies that the tubes are long and flexible enough to encompass the perovskite crystal grains (Fig. 2.3.4). The fact that the SWNT strings appear thicker than the measured diameters indicates that many tubes exist in bundles.

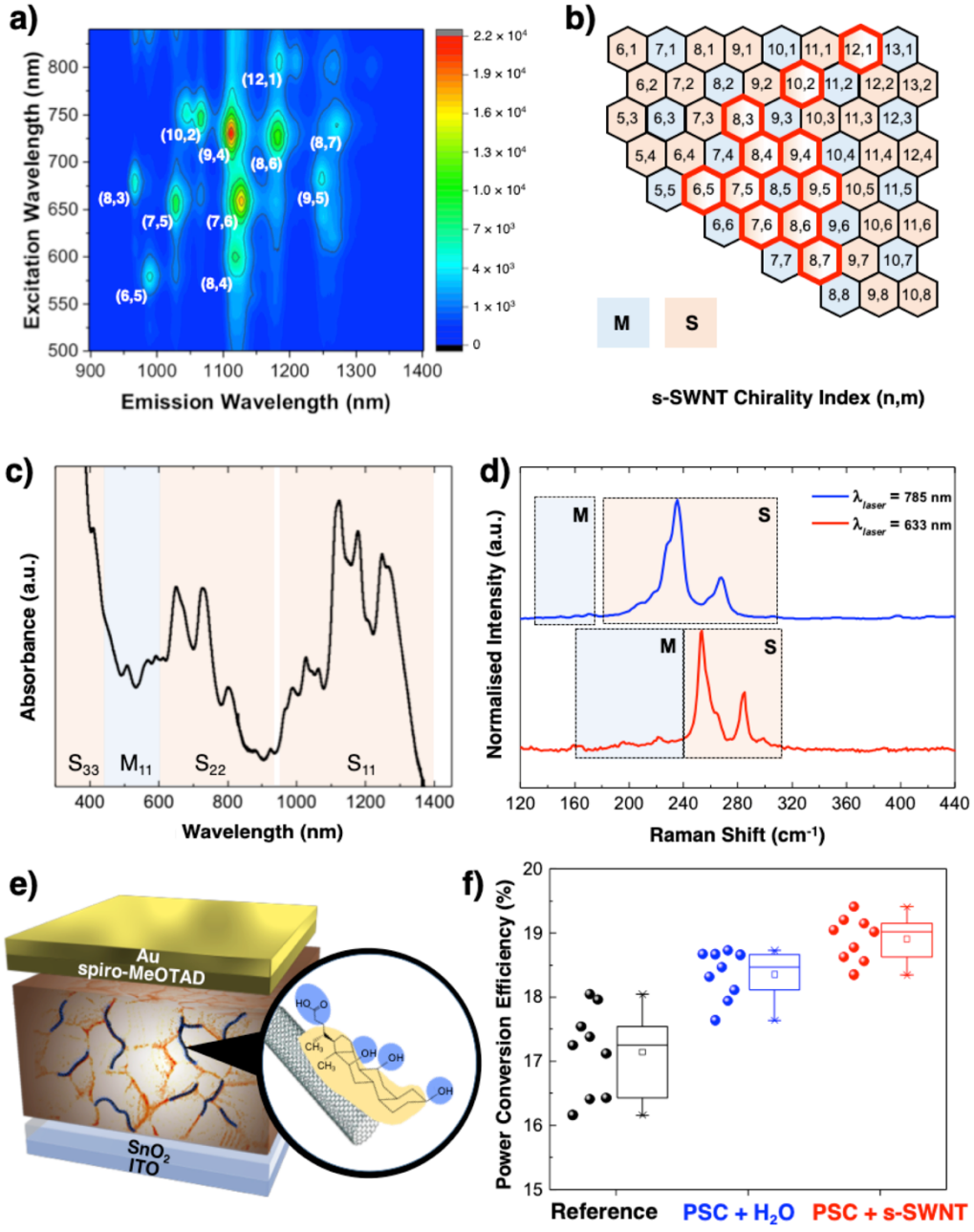

Figure 2.3.1 (a) PL mapping of the purified s-SWNTs. (b) Chirality index mapping of the s-SWNT solution with the corresponding chirality marked with red color. (c) UV-Vis-NIR Absorption spectroscopy of the s-SWNTs. (d) Raman spectroscopy of the s-SWNTs under the 785 nm laser line (blue) and 633 nm laser line (red). (e) Structure of the PSC fabricated in this work with an illustration of s-SWNT with an attached DOC surfactant. (f) Statistical analysis data of obtained PCEs from the reference devices (black), the water-added devices (blue), and the s-SWNT-added devices (red).

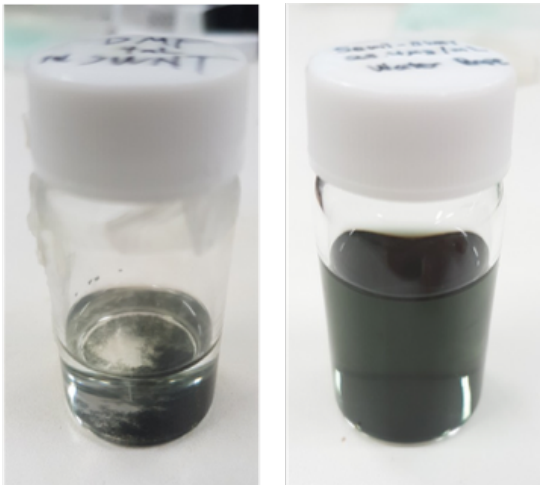

Figure 2.3.2. Pictures of SWNTs without surfactants in water (left) and our s-SWNTs with DOCs dispersed in water (right).

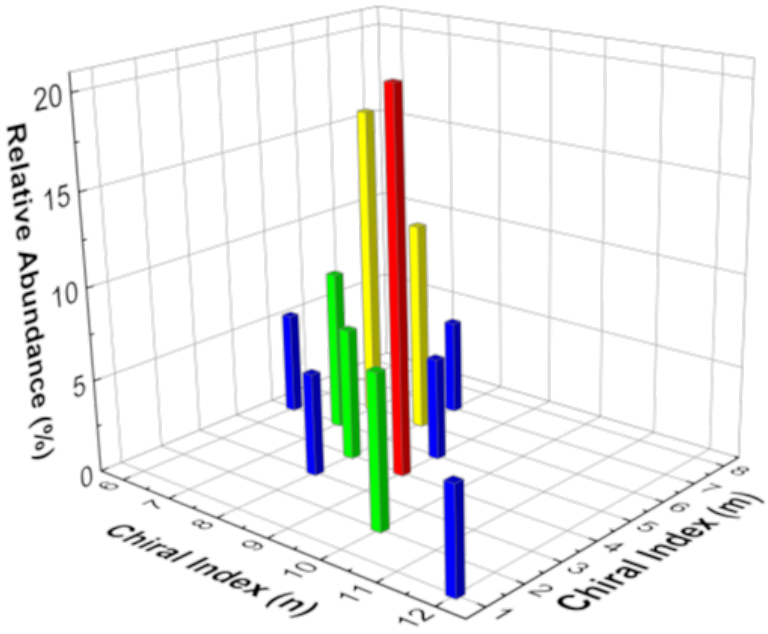

Figure 2.3.3. A 3D graph indicating the relative abundance and chirality index (n,m) of s-SWNTs we purified.

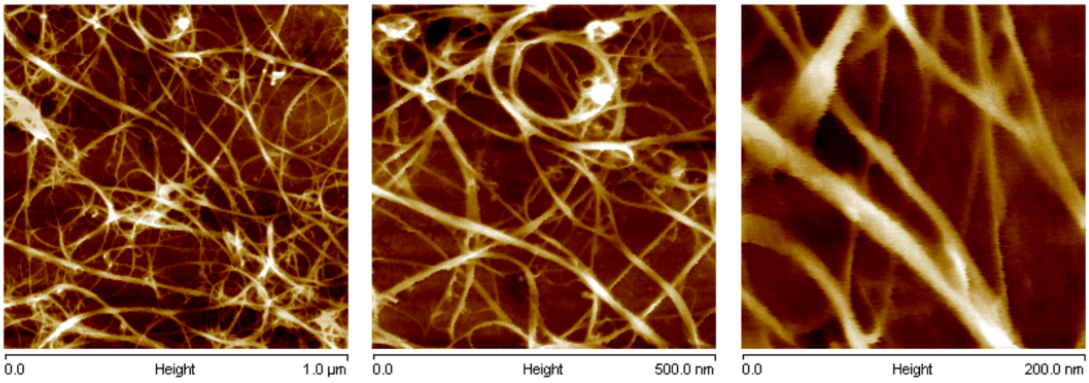

Figure 2.3.4. AFM images of the drop-casted s-SWNTs on glass substrates.

Table 2.3.1. Chirality mapping table of the s-SWNT solution we purified.

(n,m) index	Diameter (nm)	Chiral angle (θ°)	E11 (nm)	E22 (nm)	PL Intensity (counts)	Relative Abundance (%)
(6,5)	0.76	27.00	983	570	5883	5.53
(7,5)	0.83	24.50	1022	638	9183	8.63
(7,6)	0.90	27.46	1113	642	18060	16.98
(8,3)	0.78	15.30	952	663	5875	5.52
(8,4)	0.84	19.11	1102	578	7523	7.07
(8,6)	0.97	25.28	1165	718	12026	11.31
(8,7)	1.03	27.80	1263	726	5453	5.13
(9,4)	0.92	17.48	1101	720	21780	20.48
(9,5)	0.98	20.63	1244	671	5862	5.51
(10,2)	0.88	8.948	1053	734	8731	8.21
(12,1)	0.99	3.963	1171	797	5978	5.62

2.4 Device fabrication with s-SWNT additives

$MAPbI_3$ precursor solutions containing different concentrations of the s-$SWNT_{(aq)}$ were used for PSC fabrication (Fig. 2.3.1e and). The performance of s-SWNT-added PSCs were compared to that of conventional PSCs and water-added PSCs to differentiate the effect of s-SWNTs from water. The conventional PSCs exhibited a PCE of 18.1% with the short-circuit current (J_{SC}) of 23.1 mA cm^{-2}, the open-circuit voltage (V_{OC}) of 1.06 V, and the fill factor (FF) of 0.74 (Table 2.4.1, Fig. 2.3.1f, Fig. 2.4.1-5). The water-added PSCs showed a higher PCE of 18.7% with the J_{SC} of 22.9 mA cm^{-2}, V_{OC} of 1.08 V, and FF of 0.76. The s-$SWNT_{(aq)}$-added PSCs showed an even higher PCE of 19.5% with the J_{SC} of 23.7 mA cm^{-2}, V_{OC} of 1.14 V, and FF of 0.72. Water-added PSCs have previously been reported to provide higher PCEs than reference devices in both inverted-type[74–77] and normal-type[78] PSCs owing to improved perovskite film morphology and coverage. While the reported optimal concentration of the water additive differs among the literatures, 2 wt% was the optimal concentration in our case (Table 2.4.3). The same was true for the s-$SWNT_{(aq)}$-added PSCs. A concentration of 2 wt% gave the highest device performance (Table 2.4.2). A notable difference in the photovoltaic parameters between the s-SWNT-added PSCs and the water-added PSCs was that the s-SWNT-added PSCs exhibited higher J_{SC} and V_{OC}, but lower FF. Consequently, we conjectured that the s-SWNTs possibly functioned as an effective additive improving the crystal quality and charge carrier dynamics in the device. The decrease in FF was cause by the increase in R_S, indicating possible hinderance in charge flow upon the addition of s-SWNT.

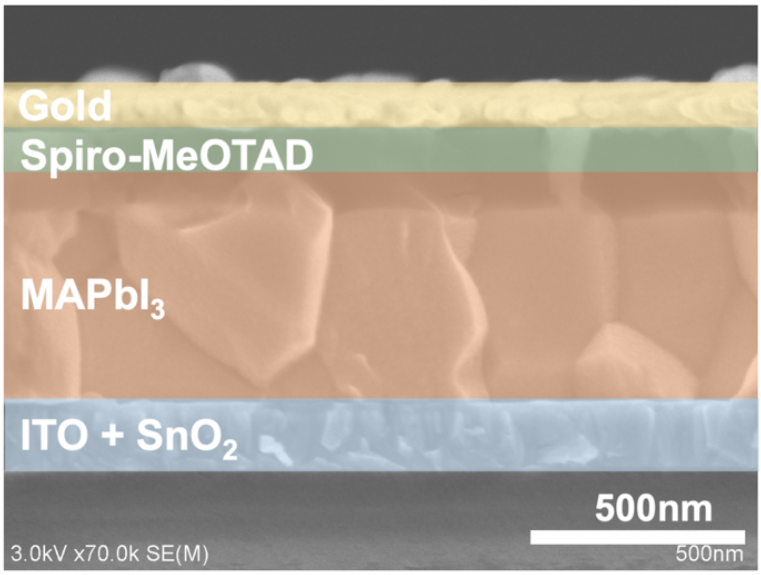

Figure 2.4.1. Cross-sectional SEM images of the fabricated PSCs.

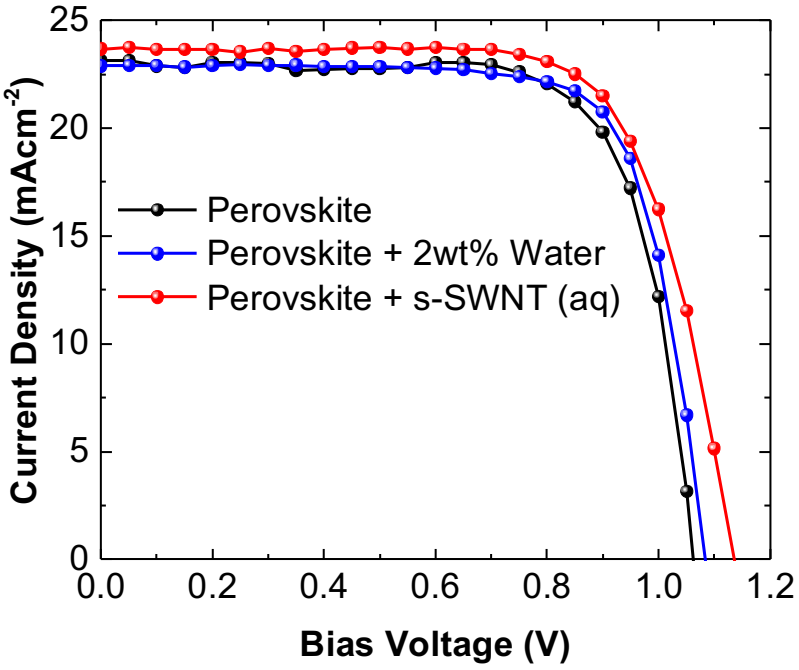

Figure 2.4.2. Current density–bias voltage (*J–V*) curves of the reference device (black), the water-added PSC (blue), and the s-SWNT-added PSC (red).

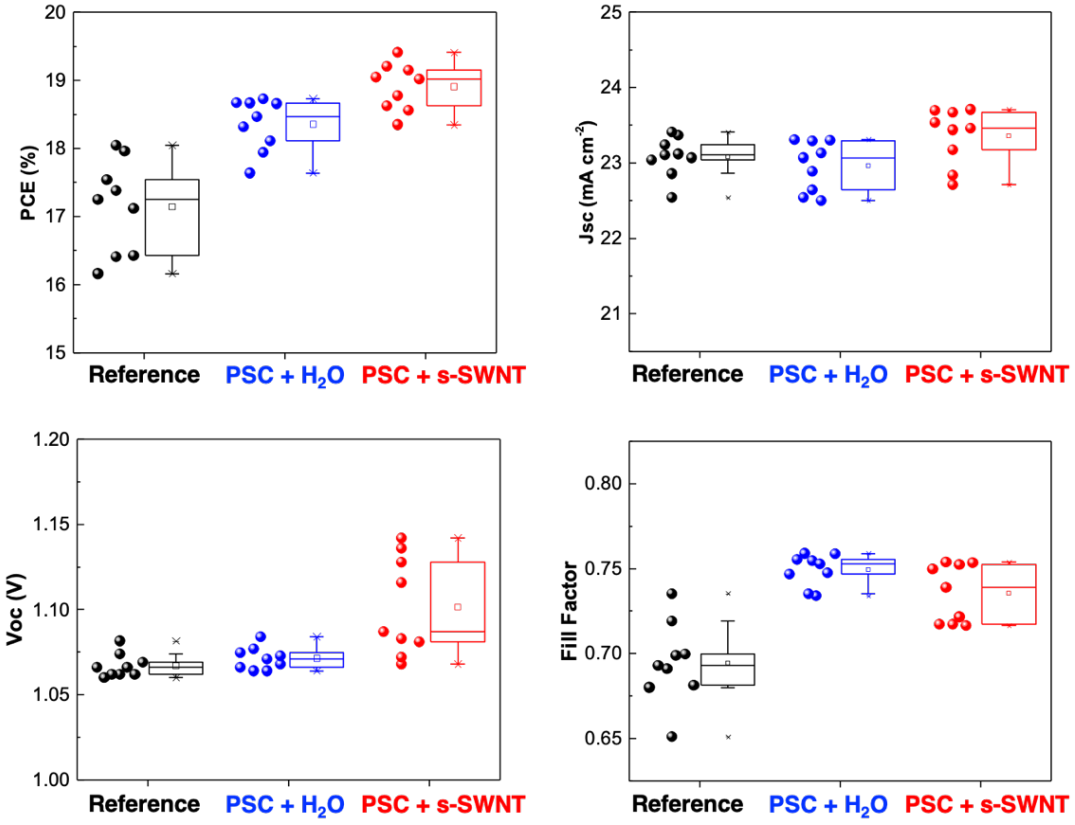

Figure 2.4.3. Statistical analyses of the photovoltaic parameters of the reference devices (black), the water-added PSCs (blue), and the s-SWNT-added PSCs (red).

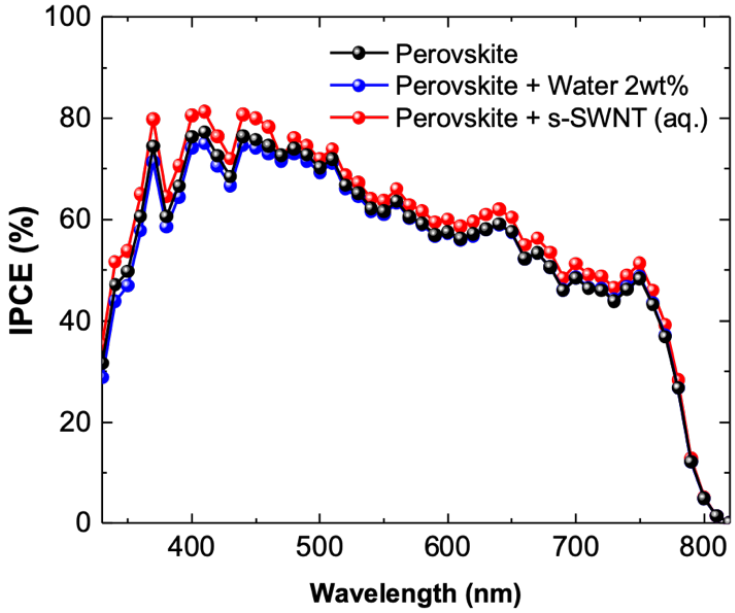

Figure 2.4.4. IPCE data of the reference devices (black), the water-added PSCs (blue), and the s-SWNT-added PSCs (red).

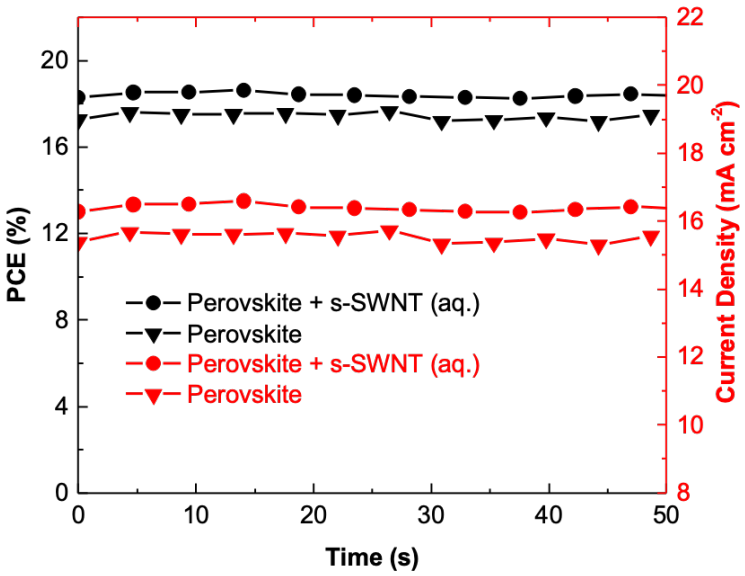

Figure 2.4.5. Maximum power point tracking of the reference devices and the s-SWNT-added PSCs.

Table 2.4.1 Photovoltaic parameters of the reference PSCs and the PSCs using water and s-SWNT$_{(aq)}$ as additives under 1 sun (AM 1.5 G, 100 mW cm-2), showing the best and average PCE values.

Active Layer	J_{SC} (mA cm^{-2})	V_{OC} (V)	FF	R_S (Ω cm^2)	R_{SH} (Ω cm^2)	PCE$_{best}$	PCE$_{average}$
$MAPbI_3$	23.1	1.06	0.74	29.7	4.53x10^4	18.1%	17.1±0.9%
$MAPbI_3$ + 2wt% water	22.9	1.08	0.76	58.5	1.94x10^5	18.7%	18.3±0.5%
$MAPbI_3$ + 2wt% s-SWNT$_{(aq)}$	23.7	1.14	0.72	92.6	8.87x10^4	19.5%	18.9±0.5%

Table 2.4.2 Photovoltaic performance of the s-SWNT-added PSCs with varying s-SWNT$_{(aq)}$ concentrations under 1 sun (AM 1.5 G, 100 mW cm^{-2}).

s-SWNT concentration	J_{SC} (mA cm^{-2})	V_{OC} (V)	FF	R_S (Ω cm^2)	R_{SH} (Ω cm^2)	PCE$_{best}$ (%)	PCE$_{average}$ (%)
1wt%	23.5	1.08	0.76	45.6	5.69x10^4	19.3	18.7 ±0.5
2wt%	23.7	1.14	0.72	72.6	1.87x10^4	19.5	19.1 ±0.3
3wt%	22.4	1.13	0.70	84.4	7.95x10^4	18.2	18.0 ±0.2
10wt%	20.5	1.15	0.68	93.5	2.28x10^4	15.4	14.5 ±0.8

Table 2.4.3 Photovoltaic performance of the water-added PSCs with varying water concentrations under 1 sun (AM 1.5 G, 100 mW cm^{-2}).

Water additive concentration	J_{SC} (mA cm^{-2})	V_{OC} (V)	FF	R_S (Ω cm^2)	R_{SH} (Ω cm^2)	PCE_{best} (%)	$PCE_{average}$ (%)
1 wt%	23.1	1.06	0.74	51.1	1.15x10^4	18.2	17.9 ±0.3
2 wt%	22.9	1.08	0.76	58.5	1.94x10^5	18.7	18.3 ±0.4
3 wt%	21.8	1.07	0.75	43.2	5.64x10^5	17.5	17.2 ±0.3
5 wt%	22.8	1.10	0.74	63.1	2.46x10^5	18.3	18.1 ±0.4
10 wt%	22.4	1.09	0.73	70.9	2.95x10^5	17.9	17.3 ±0.4

2.5 Enhanced perovskite thin film quality with s-SWNT additives

From the AFM images and their roughness average (R_a) values, we can observe that the conventional perovskite films display rough and inhomogeneous grain sizes (Fig. 2.5.1a-c). The water-added perovskite films show more uniform crystal grains, which is in par with the previous reports (Fig. 2.5.1b) [77]. The s-SWNT added perovskite films show a much larger grain size with the decreased grain boundaries (Fig. 2.5.1c), implying the influence of s-SWNTs on the crystal growth of the film. This explains the high J_{sc} values of the s-SWNT-added PSCs compared with the water-added PSCs and the reference devices, because large perovskite grains have known to give high J_{sc} values. Furthermore, our incident photon to current efficiency (IPCE) data show that there are higher IPCE values in the lower wavelength region between 350nm and 450nm (Fig. 2.4.4). We corroborate this to be from the excitation in s-SWNTs as they correspond to the band gaps of the chiralities found in Fig. 2.3.1a and b. Thus, the s-SWNTs may have also contributed to the high J_{sc}. SEM and TEM were conducted on the s-SWNT added perovskite films to characterize the s-SWNTs in the perovskite grain boundaries. The TEM image of the perovskite grain boundary (Zone 1) in fig. 2.5.1d shows that there are non-crystalline substances found at the surface of perovskite grains (Fig. 2.5.1e). These are suspected to be s-SWNTs and DOCs. There seem to be DOC aggregation (Zone 2) which probably contains both DOCs and sometimes a large aggregation which probably contains both DOCs and s-SWNTs as a bundle (Zone 3). Some images show a long trail of s-SWNTs along the perovskite grain, which are likely to be single strings of s-SWNTs passivating the grain boundary (Fig. 2.5.1f, 2.5.2b, d). The fast Fourier transform (FFT) analysis supports our point as the perovskite grain area has a cubic phase crystal with a spacing of approximately 3A, whereas the s-SWNT and DOC areas are totally amorphous. Such amorphous aggregations were not observed

in the reference perovskite (Fig. 2.5.2a,c). To understand the influence of the added water and s-SWNT on the perovskite crystal growth, environmental SEM (ESEM) was used to observe the perovskite crystal growth *in situ*. It is worth noting that due to the vacuum environment of the ESEM set up, actual crystal nucleation and growth conditions in the ambient atmosphere will be different. Therefore, the data are valid only for the comparison between the different experimental splits. Fig. shows that the water added perovskite films demonstrate much more uniform and circular perovskite seeds with a slower growth rate than the reference films. This implies that the influence of the water additive spans from the seed formation to the growth rate, which leads to a better morphology of the perovskite films. The s-SWNT-added perovskite films also display uniform and circular seeds owing to the added water, but the crystals are much larger and the crystal growth is slower compared with that of the water-added perovskite film. This proves that the added s-SWNTs function as crystal growth templates. The illustration in Fig. 2.5.1g depicts how the added water and s-SWNTs interact during the perovskite film formation.

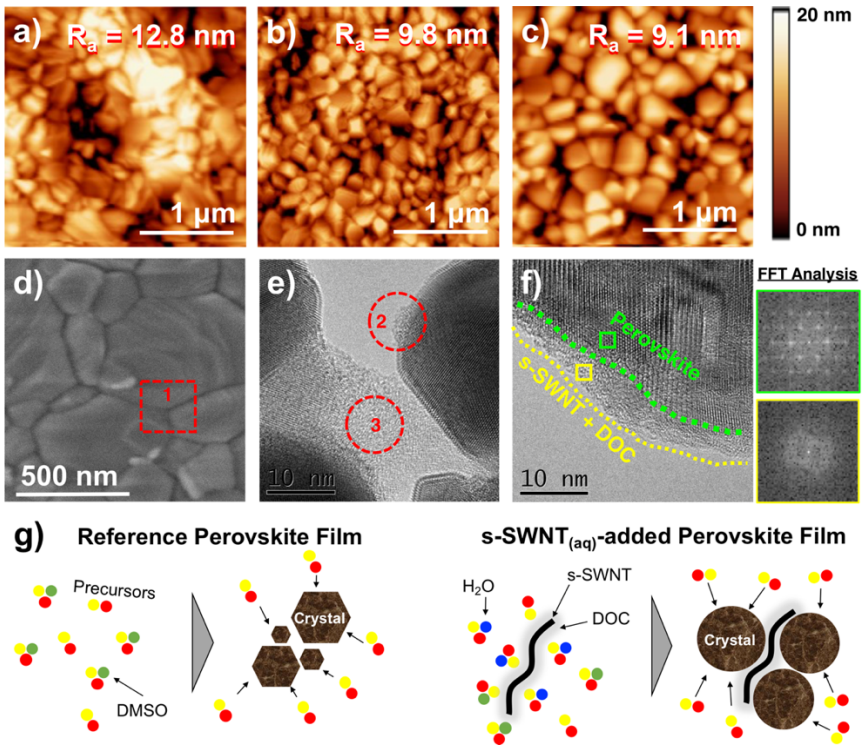

Figure 2.5.1 AFM images of (a) the reference MAPbI3 film, (b) the water-added MAPbI3 film, and (c) the s-SWNT-added MAPbI3 film. (d) SEM image and (e)(f) TEM images of the s-SWNT-added MAPbI3 film with the FFT analysis as insets. (g) Illustration depicting the role of water and s-SWNT additives during the perovskite growth of the s-SWNT-added MAPbI3 film compared with the reference.

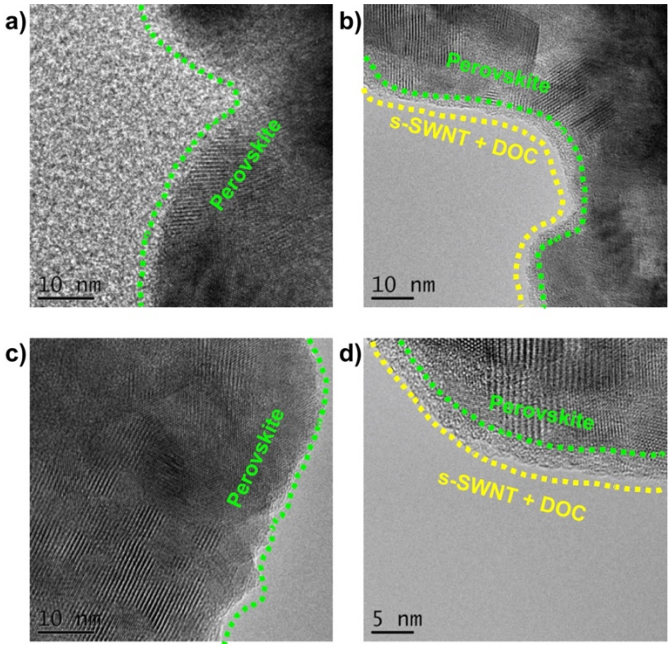

Figure 2.5.2. TEM images of (a), (c) the reference perovskite films and (b), (d) the s-SWNT-added perovskite films.

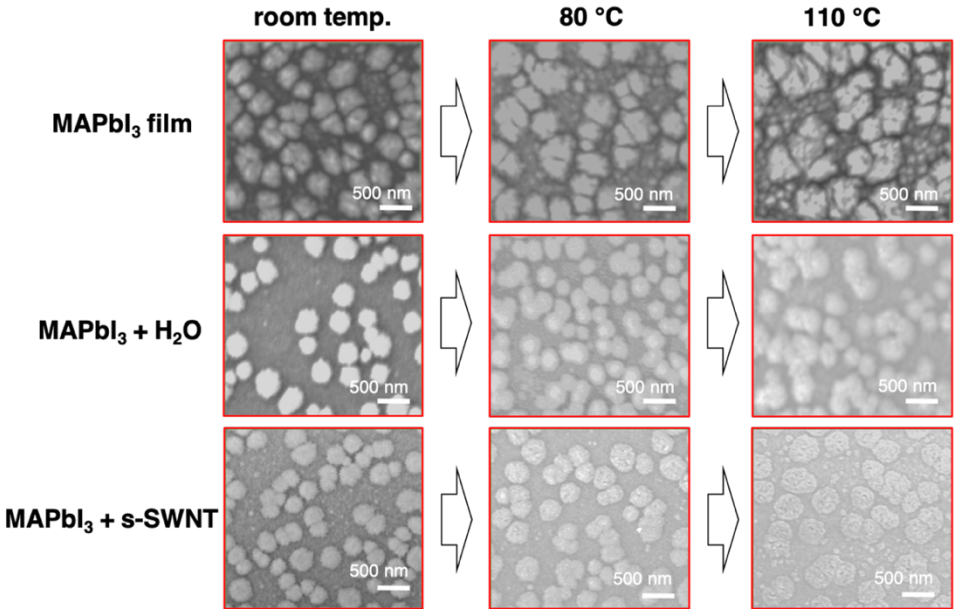

Figure 2.5.3. ESEM images of the reference $MAPbI_3$ films, the water-added $MAPbI_3$ films, and the s-SWNT-added $MAPbI_3$ films as we anneal the environmental temperature *in situ*.

2.6 Grain boundary passivation and enhanced grain size due to incorporation of purified s-SWNTs

Interactions of Lewis bases, namely, dimethyl sulfoxide (DMSO), water, methylammonium ion (MA), and DOC on Pb^{2+} was deduced from our density functional theory (DFT) calculation of (Fig. 2.6.2). The calculation results show that the interaction between DOC and Pb^{2+} is stronger compared to DMSO and water (Table 2.6.1). This means that DOC can effectively raise the nucleation energy, ΔG to slow down the crystal growth better than either DMSO or water. The ability for s-SWNTs to function as the crystal growth template comes from the Lewis base carbonyl groups with lone pair electrons on DOC, interacting with the nucleation sites of the Lewis acid perovskite precursors perovskite precursors.[79] This is an interesting concept as none of the reported s-SWNT applications to perovskite material does not involve surfactants, to the best of our knowledge.[80,81] Fourier-transform infrared (FTIR) spectroscopy data reveals that the C=O bond absorption peak of DOC powder at 1,560 cm^{-1} shifted to a lower vibration upon addition of PbI_2 (Fig. 2.6.1a).[82] The weakened C=O bond strength of DOCs indicates the formation of SWNT–DOC–PbI_2 adducts by formation of a dative bond mediated from the lone pair electrons on C=O. The formation of such adducts retards the crystal growth by elevating nucleation barrier of perovskite nuclei, thereby increasing the size of perovskite crystal grains.[83] Unlike dimethyl sulfoxide (DMSO), DOCs on SWNTs do not evaporate during the annealing step of the perovskite films, which implies that SWNT-DOCs remain in the films after completion of the crystal growth. As illustrated in Fig. 2.5.1g, the SWNT-DOCs and their adducts are probably repelled to the grain boundaries as the grain gets larger, subsequently sitting at the grain boundaries. X-ray diffraction spectroscopy (XRD) confirms the increase in the grain size and the passivation of the grain boundaries (Fig. 2.6.3 and 2.6.5, Table 2.6.2 and 2.6.3). The XRD spectra of the perovskite films indicate a tetragonal phase with a dominant (110) peak at 14.1°. The crystal grain size can be

estimated from full-width at half-maximum (FWHM) of the (110) peaks using the Debye-Scherrer equation.46 The reference film, the water-added perovskite film, and the s-SWNT-added perovskite film exhibit the (110) peaks with the FWHM values of 0.456, 0.469, and 0.448, respectively (Fig 2.6.3, Table 2.6.2). Therefore, the crystal grain size of the water-added perovskite films is the smallest and that of the s-SWNT-added perovskite films is the largest, which agree with the observation made from the AFM images in Figure 2.5.1. In addition, the intensity ratio of the (110) peak to the (220) peak indicates the growth of the (110)-oriented grains, [84] which is favorable for the hole injection from the perovskite to Spiro-MeOTAD. [85] The s-SWNT-added films exhibit the greatest ratio of 1.58 (Table 2.6.2). The XRD spectra with varying s-SWNT(aq) concentrations show that the grain size increases with the increase in the amount of s-SWNTs added (Fig. 2.6.4 and 2.6.5, Table 2.6.3). The small peak at 13.0° comes from the lattice planes of hexagonal PbI_2. [86] The peak is suppressed with the increase in the s-SWNT(aq) concentration, indicating that the hydrophobic s-SWNTs at the grain boundaries might be protecting the perovskite films from environmental degradation or dissociation (Fig. 2.6.4b). The existence of PbI_2 in perovskite film is known to increase J_{SC} and FF, but decrease V_{OC}. If PbI_2 is deficient, the opposite effect will take place. This indicates that the small amount of PbI_2 might have contributed to the high V_{OC} obtained from the s-SWNT-added devices (Fig. 2.4.3, Table 2.4.1). Trap-states at the grain boundaries induce non-radiative recombination, decreasing the charge carrier lifetime and broadening photoluminescence (PL) peak. [87,88] While both the water-added and the s-SWNT-added perovskite films exhibited blue shifts compared with the reference films, the s-SWNT-added perovskite films displayed marginally smaller FWHM, indicating possible passivation of the trap states by DOCs on SWNTs (Fig. 2.6.6). [89] Transient PL substantiates this by revealing that the s-SWNT-added perovskite films show longer average carrier lifetime (Fig. 2.6.7). Further evidence for the trap sites passivation can be found from the XPS data in Figure 2.6.1b. Both the water-added perovskite films and the s-SWNTs-added perovskite films

have the Pb 4f 5/2 and 4f 7/2 peaks shifted to a higher binding energy compared with those of the reference films. The shifts are due to the perovskite crystals containing less metallic Pb, which proves the higher quality of the perovskite films. [90–92] Notably, the peaks of the s-SWNTs-added perovskite films are narrower than the other films, because there are less Pb^{2+} species owing to the greater grain size and the passivation from the s-SWNTs. PSCs with DOCs as additives without s-SWNTs were fabricated. The devices exhibited significantly low PCEs with notably high series resistance (R_S) values (Table 2.6.4). This shows that DOCs alone cannot function as the charge transporters and s-SWNT backbones are necessary as they enhance the charge flow of the perovskite film (Fig. 2.6.7). Furthermore, conductive-AFM of the s-SWNT-added perovskite films show more highly conductive spots at the grain boundaries than the water-added perovskite films, corroborating the charge conductivity enhancement with the presence of s-SWNTs (Fig. 2.6.8). Time-resolved microwave conductivity (TRMC) measurement shows that the perovskite films with s-SWNTs exhibit much faster decay, suggesting improved charge extraction kinetics (mainly holes) from the perovskite active layer to the Spiro-MeOTAD layer (Fig. 2.6.1c). [93] This is related to the aforementioned enhancement of film hole mobility and (110)-oriented grains. To gain further insight into the roles of s-SWNT in the perovskite film, the electrical impedance spectroscopy (EIS) analysis was conducted. Figure 2.6.1d shows the Nyquist plots of the reference perovskite film, the water-added perovskite film, and the s-SWNT-added perovskite films under illumination, with the equivalent circuit shown in the inset. It is known that in the EIS analysis, the high frequency component represents the charge transfer resistance (R_{ct}).60 In the present study, the only variable affecting R_{ct} is the additives in perovskite films. The numerical fitting of EIS data gives the parameters as listed in Table 2.6.5. Obviously, compared with the R_{ct} of 248.3 Ω from the reference sample, the water-added and s-SWNT-added samples show smaller R_{ct} of 121.2 Ω and 95.8 Ω, respectively. The smaller R_{ct} implies more efficient charge extraction from the perovskite active layer, which can arise from the improved morphology and coverage

of perovskite film due to the water additive. Furthermore, even smaller R_{ct} of 95.8 Ω upon addition of s-SWNTs due to more efficient charge extraction by passivation of the grain boundaries and reduced trap sites. As complementary experiments, we tested PSCs with pure metallic single-walled carbon nanotubes rather than semiconducting carbon nanotubes. PSCs with metallic single-walled carbon nanotubes exhibited poor PCEs with extremely low R_{SH}, indicating the importance of s-SWNT purity (Table 2.6.6). It is worth noting that the addition of s-SWNTs did not manifest any significant change in the device stability. [94] We suspect that this is due to the s-SWNT added being too small to have a noticeable effect.

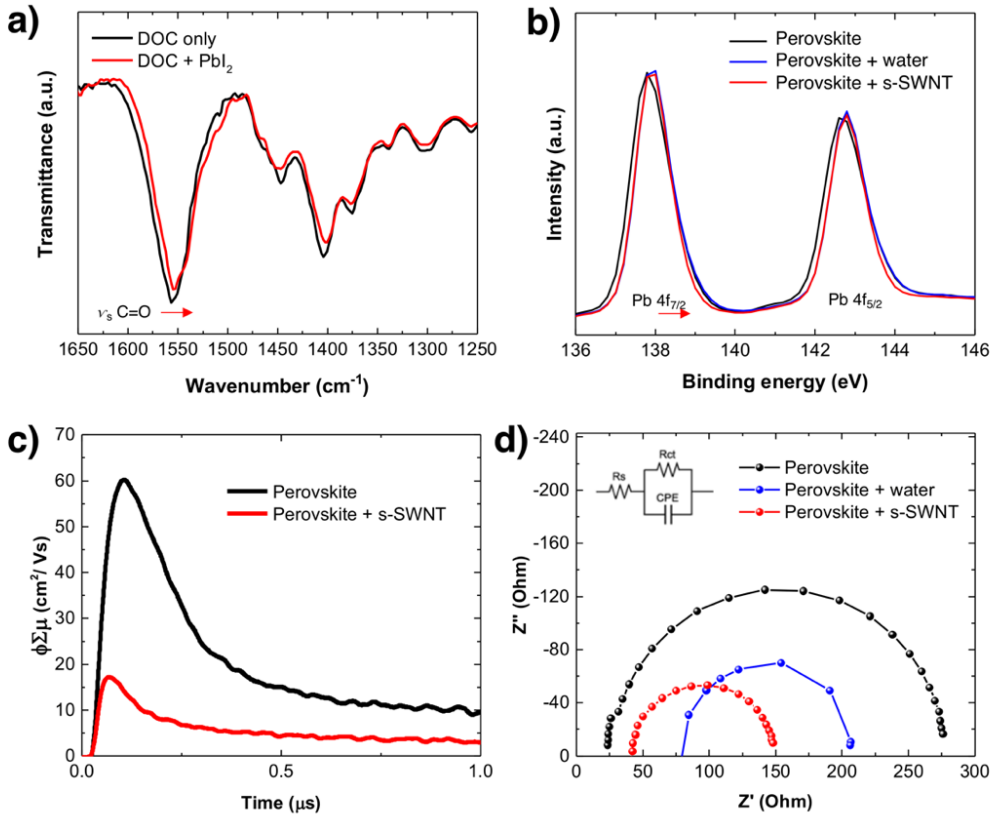

Figure 2.6.1 (a) FTIR spectra of DOC pellet (black) and DOC pellet containing PbI_2 (red). (b) Pb 4f 7/2 and Pb 4f 5/2 peaks of the XPS spectra of the $MAPbI_3$ film (black), the water-added $MAPbI_3$ film (blue), and the s-SWNT-added $MAPbI_3$ film (red). (c) The yield of free charge carriers (Φ) multiplied by the sum of the carrier mobilities ($\Sigma\mu = \mu_e + \mu_h$) giving the yield-mobility product ($\Phi\Sigma\mu$) over time for the $MAPbI_3$ film (black) and the s-SWNT-added $MAPbI_3$ film (red) with the Spiro-MeOTAD coated on top. (d) Nyquist plots of $MAPbI_3$ film (black), the water-added $MAPbI_3$ film (blue), and the s-SWNT-added $MAPbI_3$ film (red) obtained from the impedance measurement.

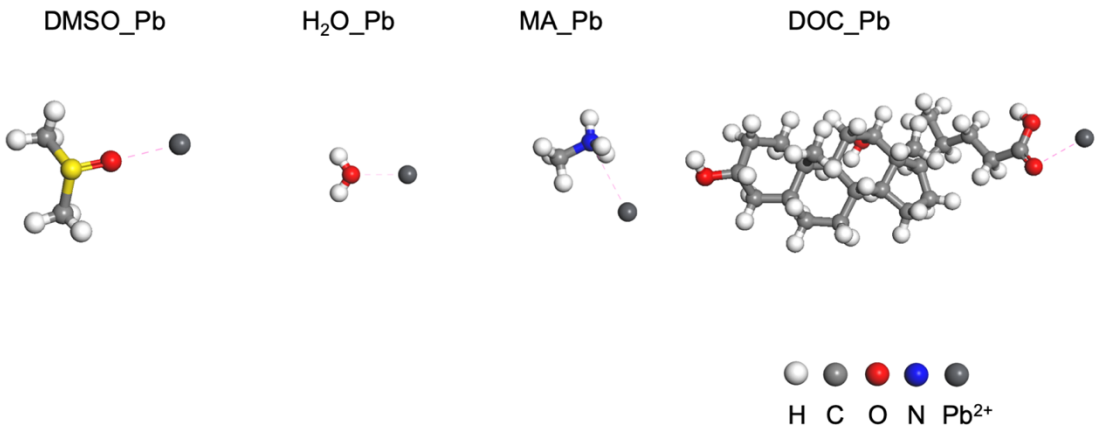

Figure 2.6.2. DFT calculation modelling of interaction between Pb^{2+} and the Lewis donors.

Table 2.6.1. DFT calculation of interaction between Pb^{2+} and the Lewis donors.

	DMSO	H_2O	MA	DOC
Energy	**-50.2**	**-14.2**	**-37.1**	**-392**
Energy next to Pb^{2+}	**-51.3**	**-15.2**	**-39.1**	**-393**
Interaction energy (eV)	**-0.506**	**-0.388**	**-1.331**	**-0.525**

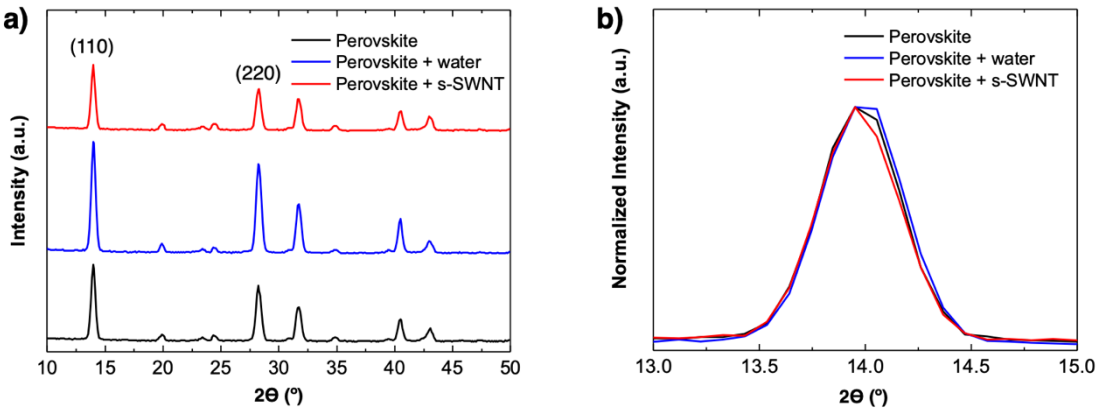

Figure 2.6.3. (a) XRD spectra of the reference $MAPbI_3$ films (black), the water-added $MAPbI_3$ films (red), and the s-SWNT-added $MAPbI_3$ films (blue). (b) Normalized (110) peak showing the FWHM trend.

Table 2.6.2. XRD peak characterizations and information for the reference $MAPbI_3$ films, the water-added $MAPbI_3$ films, and the s-SWNT-added $MAPbI_3$ films.

Sample	Peak	Position (°)	Intensity	Peak Area	FWHM	Peak Ratio
Perovskite (ref.)	<110>	14.0	1242.87	604.41	0.456	1.37
	<220>	28.2	905.02	517.53	0.548	
Perovskite + Water	<110>	14.0	1799.25	900.18	0.469	1.24
	<220>	28.2	1456.85	860.55	0.571	
Perovskite + s-SWNT	<110>	14.0	1799.25	492.46	0.448	1.58
	<220>	28.3	1456.85	374.86	0.539	

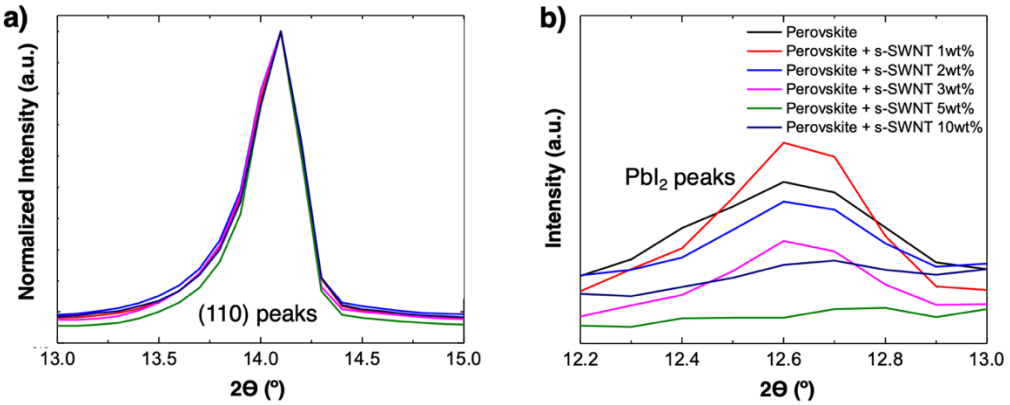

Figure 2.6.4. (a) Normalized (110) peak showing the FWHM trend of perovskite films with the increase in the s-SWNT concentration. (b) Magnified PbI_2 peaks of the perovskite films with the increase in the s-SWNT concentration.

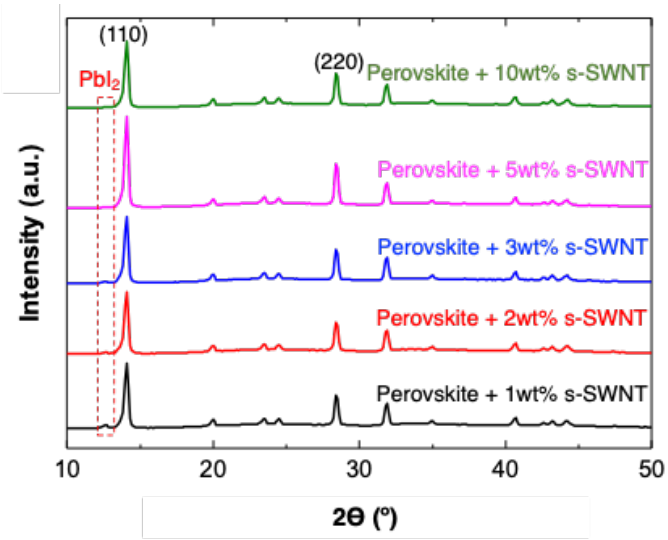

Figure 2.6.5. XRD spectra of perovskite films with the increase in the s-SWNT concentration.

Table 2.6.3. XRD peak characterizations and information for the s-SWNT-added $MAPbI_3$ film with varying s-$SWNT_{(aq)}$ concentrations.

Sample	Peak	Position (°)	Intensity	Peak Area	FWHM	Peak Ratio
Perovskite +	<110>	14.1	374653	39607	0.401	2.18
1wt% s-SWNT	<220>	28.4	320750	15818	0.388	
Perovskite +	<110>	14.1	501915	37888	0.398	2.16
2wt% s-SWNT	<220>	28.4	451442	15172	0.402	
Perovskite +	<110>	14.1	637150	39691	0.392	2.19
3wt% s-SWNT	<220>	28.4	582173	15736	0.403	
Perovskite +	<110>	14.1	813492	51066	0.388	2.24
5wt% s-SWNT	<220>	28.4	734450	20489	0.386	
	<110>	14.1	948474	39449	0.391	2.13

Perovskite + 10wt% s-SWNT	<220>	28.4	894635	16531	0.385	

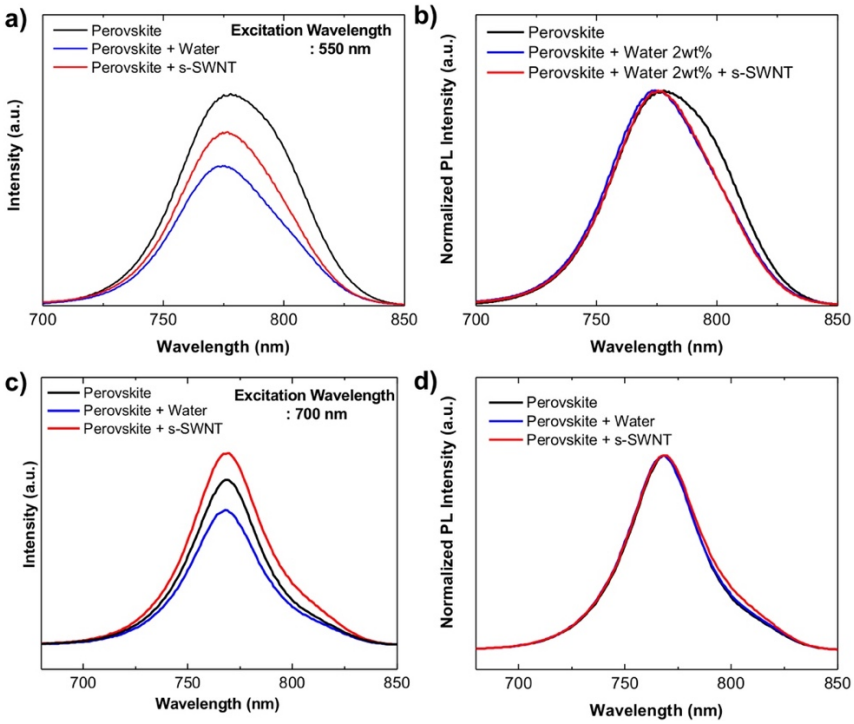

Figure 2.6.6. (a), (c) Raw and (b), (d) their normalized PL spectra with the different excitation wavelength of the reference $MAPbI_3$ films (black), the water-added $MAPbI_3$ films (blue), and the s-SWNT-added $MAPbI_3$ films (red).

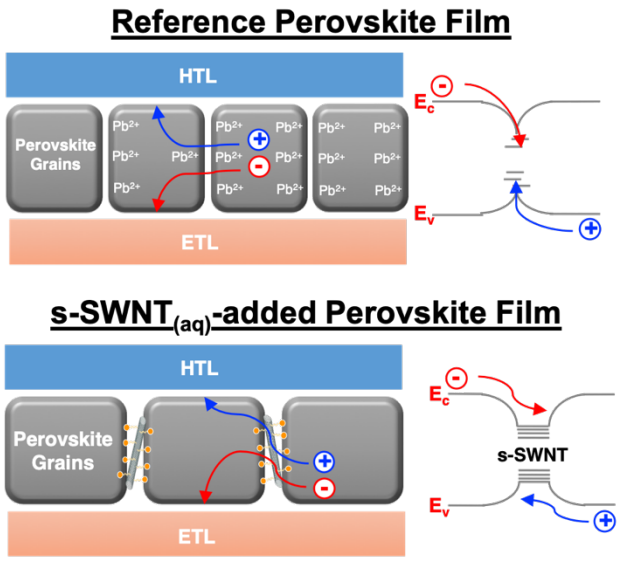

Figure 2.6.7. Cross-sectional illustration of MAPbI3 films (above) and the s-SWNT-added MAPbI3 films (below).

Table 2.6.4. Photovoltaic performance of the DOC-added PSCs.

DOC concentration	J_{SC} (mA cm^{-2})	V_{OC} (V)	FF	R_S (Ω cm^2)	PCE_{best} (%)	$PCE_{average}$ (%)
0.1 wt%	9.82	1.02	0.33	567	3.38	2.85 ±0.37
1.00 wt%	8.72	0.95	0.27	671	2.21	1.77 ±0.32

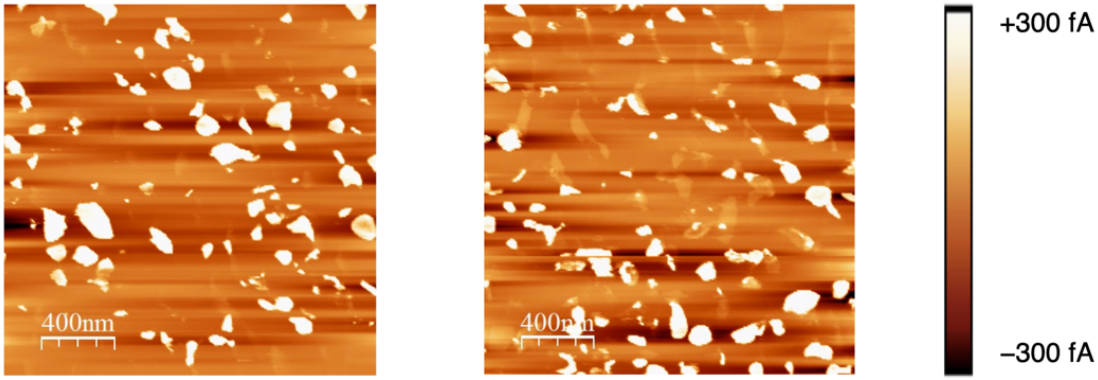

Figure 2.6.8. Conductive AFM images of the water-added $MAPbI_3$ films (left), and the s-SWNT-added $MAPbI_3$ films (right).

Table 2.6.5. EIS parameters for the PSCs of the reference $MAPbI_3$, the water-added $MAPbI_3$, and the s-SWNT added $MAPbI_3$.

Sample	Rs (Ω)	Rct (Ω)
Perovskite (ref.)	24.3	248.3
Perovskite + Water	82.1	121.2
Perovskite + s-SWNT	45.3	95.8

Table 2.6.6. Photovoltaic performance of the m-SWNT-added PSCs.

m-SWNT concentration	J_{SC} (mA cm^{-2})	V_{OC} (V)	FF	R_S (Ω cm^2)	PCE_{best} (%)	$PCE_{average}$ (%)
2 wt%	15.28	0.91	0.47	44.4	1.43x10^2	6.6

2.7 Summary

By incorporating a small amount of s-SWNTs in deionised water, a PSC PCE of 18.1% increased to 19.5%. The added s-SWNTs worked as both crystal growth templates and grain boundary passivators thanks to the attached DOC surfactants. The s-SWNTs themselves functioned as charge bridges at the grain boundaries as well, increasing the mobility of the perovskite film. The resulting effects were increased grain size and reduced charge trap, which were reflected by the increased J_{SC} and V_{OC}. The FF improvement was limited in comparison with the water-added control devices, which, we predict, can be resolved by using purer s-SWNTs and surfactants with higher mobility than DOC. As the technology of this work does not require a large amount of s-SWNTs which are costly, the potential feasibility of this work can be said to be excellent. Therefore, we expect further follow-ups of this work in near future.

Chapter 3:

Highly Efficient Metal-Free Semi-Transparent Perovskite Solar Cells enabled by MoO_3-doped Transparent Carbon Nanotube Top Electrodes and Four-Terminal Perovskite Silicon Tandem Applications

3.1 Research Background and Introduction

Organic-inorganic lead halide perovskite solar cells (PSCs), since the first report in 2009, have emerged as promising next-generation thin-film photovoltaics with the high power conversion efficiency (PCE), low material cost, and facile solution processing. Today, the certified PCE of PSCs on a laboratory scale reads over 25%. To supersede the commercially available silicon solar cells (SiSCs), thin-film photovoltaics such as PSCs should extend the application to solar panel windows and tandem solar cells. Micrometer-thinness, light-weight and bandgap tunability of PSCs enable solar energy-harvesting windows which SiSCs cannot achieve. In addition, by combining PSCs with SiSCs in a tandem structure, the theoretical Shockley-Queisser (SQ) of ~33% [95,96] can be surpassed thanks to the larger band gap of PSCs compared with that of SiSCs

[33,97–104]. However, both of those applications require PSCs to be semi-transparent while having high PCE.

To achieve highly transparent and efficient semi-transparent PSCs, the transparent top electrode plays a crucial role. To date, transparent conductive oxide (TCO) electrodes, such as indium tin oxide (ITO), indium zinc oxide, and Al-doped zinc oxide have been widely used. Nevertheless, they are deposited by a magnetron sputtering in which high energetic particles often damage the underlying layers and high-cost vacuum atmosphere is necessary. Furthermore, these TCOs mandate oxygen flow and high temperature annealing for high optical transmittance and electrical conductivity, [105] both of which undermine the sublayers. Metal nanowires could provide a solution to this, but their reflective nature [106] and metal-migration-induced device degradation [107,108] deter them from being the alternative.

Recently, single-walled carbon nanotube (CNT) transparent electrode [29,109] has been reported as the top electrode in semi-transparent PSCs and demonstrated high PCE surpassing even that of the metal electrode-based PSCs. [33,34,110,111] Use of CNT electrodes drastically reduces the fabrication cost as they are made from abundant carbon sources and can easily be laminated onto devices by a simple mechanical transfer [32,112,113] The prospect of such CNT top electrode-based PSCs will be boosted if the efficiency and the transparency of the devices improve even further. The most effective strategies to achieve this is threefold: (1) tuning the work function of the CNT electrode to align with the energy levels of the active perovskite layer and hole-transporting layer and thereby maximizing the open-circuit voltage (V_{OC}), (2) increasing the conductivity of the CNT electrode to maximize the fill factor (FF) and the short-circuit current (J_{SC}), (3) reducing the optical loss between the layers to maximize the transparency of the device. Chemical *p*-doping of the CNT electrode can tune the work function as well as boosting the conductivity. [35,39] However, it is an

extremely challenging task as applying dopants to CNT top electrode can damage the underlying sublayers. [28,114] While chemical doping of CNT top electrode in PSCs has been reported, the previous work of both solution-based [34] and vapor-based [35] doping showed serious shortcomings in controllability and reproducibility of the doping process. Using a fair amount of acidic dopants leads to either deterioration of the perovskite layer[34] or reaction with the 4-tert-butylpyridine (*t*-BP) in the 2,2',7,7'-Tetrakis[N,N-di(4-methoxyphenyl)amino]-9,9'-spirobifluorene (Spiro-MeOTAD) hole-transporting layer. Therefore, both of those approaches rely on modicum amounts of dopants, which, as a result, limit the doping effect.

Molybdenum trioxide (MoO_3) has been reported as an effective and stable dopant for carbon electrodes [29,42,115–117] and other nanomaterials [118]. MoO_3 is relatively inexpensive, microelectronic-compatible, and much safer to handle than acids. Further, MoO_3 itself can function as an effective hole-transporting material even after inducing a strong and durable doping effect. Moreover, MoO_3 has been reported to exhibit anti-reflection effect when used as a top layer in solar cells. [119]

Herein, we report multifunctional effects of MoO_3 doping on CNT electrode in semi-transparent metal electrode-free PSCs (CNT-PSCs). MoO_3 is thermally deposited onto the CNT top electrodes. The MoO_3 reduces to MoO_x where x is 2–3 upon doping the CNTs and still function as an effective hole-transporter along with the added spiro-MeOTAD. The MoO_3 doping boosts the conductivity of the CNT electrode without damaging the sublayers nor reacting with the spiro-MeOTAD solution. This is attributed to the fact that the stable nature of MoO_3, which is solvent-free and non-acidic. The controllability of the *p*-doping strength enables tuning of the CNT work function. By optimizing the thickness of MoO_3, 8-nm-thick MoO_3 layer was found to give the highest PCE of 20.25% when deposited on CNT-PSCs, in which 70% transparent CNT electrode at the wavelength of 550nm was used. The devices showed

increases in all of the photovoltaic parameters upon MoO_3 doping, namely, V_{OC} of 1.162 V, J_{SC} of 23.09 mA/cm^2, and FF of 0.755. All of which are ascribed to the better aligned energy level, the enhanced electron-blocking ability and the conductivity of the CNT electrodes. The achieved PCE is the highest among the reported CNT-PSCs to date as far as we are concerned. In addition to this, the presence of MoO_3 heightens the device transparency owing to the reduced parasitic optical loss at the CNT interface. The full potential of the MoO_3-doped CNT-PSCs were assessed by stacking them to SiSCs using a computational model and simulating the 4-terminal tandem solar cells. The enhanced transparency in both visible and near-infrared region through the minimum parasitic absorption of MoO_3 demonstrated expected higher performance of the MoO_3-doped CNT-PSCs compared with ITO-based semi-transparent PSCs [33] as well as the other semi-transparent PSCs reported thus far.

3.2 Materials and Methods

3.2.1 Synthesis of SWNT Films

Randomly oriented CNT networks with high purity and long nanotube bundle length can be synthesized by the aerosol chemical vapor deposition (CVD) method. Floating-catalyst (FC) aerosol CVD was carried out in a scaled-up reaction tube with a diameter of 150 mm. The catalyst precursor was vaporized by passing ambient-temperature CO through a cartridge filled with ferrocene powder. To obtain stable growth of CNTs, a controlled amount of CO2 was added with the carbon source (CO). CNTs were directly collected downstream of the reactor by filtering the flow through a nitrocellulose or silver membrane filter (Millipore Corp., Billerica, MA; HAWP, 0.45-μm pore diameter). The flow containing ferrocene vapor was then introduced into the high-temperature zone of a ceramic tube reactor through a water-cooled probe and mixed with additional CO. Ferrocene vapor was thermally decomposed in the gas phase

of the aerosol CVD reactor at 880 °C. The CO gas was supplied at 4 L min^{-1} and decomposed on the iron nanoparticles, resulting in the growth of CNTs. The as-synthesized CNTs were collected by passing the flow through microporous filters downstream of the reactor, and the transparency and sheet resistance were controlled by varying the collection time. The collected CNT networks were transferred to a variety of substrates through the dry press- transfer process. The FC-CVD-synthesized and dry-deposited CNT networks were of high purity. Furthermore, as the process requires no sonication-based dispersion steps, the resulting CNT network consisted of exceptionally long CNTs.

3.2.2 Fabrication of Perovskite Solar Cell with CNT top electrode

ITO patterned glass substrates were cleaned and sonicated with detergent, distilled water, acetone, and isopropanol in an ultrasonic bath for 15 min, respectively. The cleaned substrates underwent the UV-ozone for wettability enhancement and removal of any organic contamination. 30 millimolar $SnCl_2 \cdot 2H_2O$ (Aldrich, >99.995%) solution in ethanol (anhydrous, Fujifilm Wako Pure Chemical Co.) as a precursor solution was used for deposition of a compact SnO_2 layer. The solution was filtered by a 0.2 μm syringe filter, followed by spin-coating on the cleaned substrate at 3000 rpm for 30 s. The spin-coated film was annealed at 165 °C for 30 min. After cooling down to room temperature, another cycle of the spin-coating process was repeated, which was followed by annealing at 150 °C for 5 min and 190 °C for 1 h. The SnO_2-coated ITO glass was treated with UV-ozone before spin-coating of the prepared perovskite solution. Then, 20 μL of perovskite precursor solution was spin-coated onto the SnO_2 layer at 4000 rpm for 20 s, with 0.15–0.30 mL of anhydrous diethyl ether slowly dripped onto the substrate 12 s after the start of the spin-coating process. Next, the film

was annealed at 100 °C for 10 min to obtain a dense brown $MAPbI_3$ film. For the CNT-based devices, pre-cut CNT films (active area 5x2 mm^2) were laminated on the top of the prepared $MAPbI_3/SnO_2$/ITO/glass substrates to room temperature by applying press-transfer method on the perovskite surface just after cooling. Before depositing the hole transporting layer (HTL), different thickness of MoO_3 was thermally evaporated on the CNT-laminated PSCs. Then, the HTL solution was prepared by dissolving 85.8 mg of spiro- MeOTAD (Merck) in 1 mL of chlorobenzene (anhydrous, 99.8%, Sigma-Aldrich) which was mixed with 33.8 μL of 4-tert-butylpyridine (96%, Aldrich) and 19.3 μL of Li-TFSI (99.95%, Aldrich, 520 mg mL^{-1} in acetonitrile) solution. The fabrication was finally completed by thermal evaporation of a 50-nm-thick film of gold contact for electrically probing purpose at a constant evaporation rate of 0.05 nm s.

3.2.3 Characterization

The *J*−*V* curves were measured using a software-controlled source meter (Keithley 2400 Source-Meter) under dark conditions and the simulated sunlight irradiation of 1 sun (AM 1.5G; 100 mW cm^{-2}) using a solar simulator (EMS- 35AAA, Ushio Spax Inc.) with a Ushio Xe short arc lamp 500. The source meter was calibrated using a silicon diode (BS-520BK, Bunkokeiki). By using Agilent 4156C analyzer with a four-probe station, the sheet resistance of CNT films was measured (van der Pauw method). The SEM analysis of the CNTs and device cross-section were performed using an S-4800 (Hitachi) electron microscope. An inVia Raman microscope (Renishaw) was employed for the vibrational spectra observation of CNT and doped-CNT electrodes with 532 nm laser wavelength. Shimadzu UV-3150 was used for the UV−Vis−NIR measurement. The PL measurements were performed using JASCO Spectrofluorometer (FP-8300). The valence band and the Fermi levels measurements were performed using Riken Keiki PYS-A AC-2 and Kelvin probe spectroscopy in air (ESA), respectively. A source

measurement unit was used to record the current at each specific wavelength. Solartron SI1287 Electrochemical Interface and Solartron 1255B Frequency Response Analyzer were used for the Impedance Measurement.

3.2.4 Bottom Si Solar Cell Simulation

1D silicon p-n junction model with carrier generation and Shockley-Read-Hall recombination was analyzed using the COMSOL Multiphysics® semiconductor module. The p-n junction is formed by p-doping (doping concentration of $1 \cdot 10^{19}$ cm^{-3}) the front surface of an n-type (doping concentration of $1 \cdot 10^{16}$ cm^{-3}) Si wafer. The front surface p-doping is assumed to have a peak concentration of $1 \cdot 10^{19}$ cm^{-3}, and a Gaussian drop off with a junction depth of 0.25 mm. Under normal operating conditions, photo-generated carriers are swept to each side of the depletion region of the p-n junction. A small forward bias voltage is applied to extract the electrical power, given by the product of the photocurrent and the applied voltage.

3.3 Evaporated MoO_3 as an efficient p-type dopant for SWNT Top electrodes

Doping of CNT electrodes in PSCs have been widely used for enhancing the conductivity and modifying the work function to match with perovskite absorber and charge selective contacts. This improves PSC performance by reducing voltage loss and series resistance within the PSC device. Nevertheless, the doping of top carbon-based electrodes in organic or perovskite solar cells are especially difficult because the chemical dopant, often to be strong oxidants could damage the underlying devices by unwanted chemical reactions with photoactive layers [34] or charge transport layers

[35]. MoO_3, which is inorganic high work function metal oxide, have been reported as an efficient hole dopant for carbon-based electrodes, but their application was limited to bottom CNT electrodes. Here, a successful doping of a CNT top electrode was achieved without damaging the underlying device by incorporating thermally evaporated MoO_3 onto CNT top electrode and CNT morphologies. A basic CNT doping process with MoO_3 is shown in Fig. 3.3.1a. As-prepared CNT film was first mechanically dry-transferred on glass. The optical transparency of CNT film ranged from 70% to 90% at 550 nm wavelength owing to CNT collection time during aerosol CVD (Fig. 3.3.1b). They were highly crystalline with low defects as D/G ratio from raman spectra was < 0.1 (Fig. 3.3.2). After thermal deposition of MoO_3 on CNT film, the hole doping ability of MoO_3 was analyzed. The four-probe measurement was employed to measure sheet resistance of the CNT films upon MoO_3 doping. According to Figure 3.3.1c, the bare CNT film of T70%, T80% and 90% has a sheet resistance of approximately 65.4, 259.8 and 322.1 $\Omega\ sq^{-1}$ respectively. The gradual decrease in sheet resistance is observed with an increase in the MoO_3 deposition thickness over all CNT films. There is a particularly sharp decrease in the sheet resistance to 4 nm of the MoO_3 thickness, followed by saturation or slight increase of the sheet resistance with MoO_3 thickness more than 4 nm. Although the decrease in the sheet resistance is not as significant as the reported acid drop-cast, this MoO_3 deposition successfully induces doping of the CNT films. Raman spectra can also show the *p*-type doping effects of CNTs. Figure 3.3.1d reveals the blue shift of 2D band and relative suppression of 2D band intensity after MoO_3 deposition on CNTs. This indicates the substantial charge withdrawal from the CNTs [120]. From optical absorbance spectra, we also observed a slight quenching of the optical transitions of the van Hove singularities ($^{M}E_{11}$, $^{S}E_{22}$, $^{S}E_{11}$) after MoO_3 deposition. This implies that the interband optical transitions were suppressed due to the shift of the Fermi level by the deposited MoO_3. Doping stability of MoO_3 on CNTs were further analyzed with measuring the sheet resistance of MoO_3

deposited CNT film for 7 weeks. The sheet resistance was maintained under 35 Ω sq^{-1} for 7 weeks, which indicates stable p-doping of CNTs.

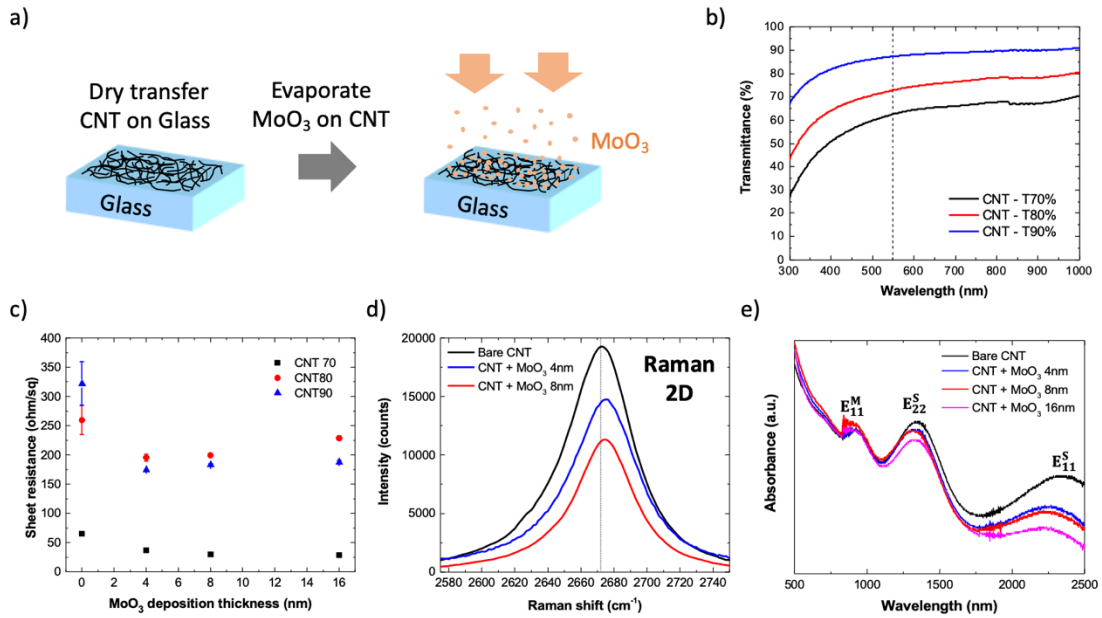

Figure 3.3.1 (a) Schematic illustration showing the fabrication of hole doping of carbon nanotube (CNT) by thermally evaporated MoO_3 under vacuum. (b) Optical transmittance of 70T%-CNT film (black), 80T%-CNT film (red), 90T%-CNT film (red). (c) Measured sheet resistance of 70T%-CNT film (black), 80T%-CNT film (red), 90T%-CNT film (red) with different thickness of deposited MoO_3. (d) Raman spectra 2D band of bare CNT (black), CNT with 4 nm MoO_3 (blue) and CNT with 8 nm MoO_3 (red). (e) Vis-NIR spectra of bare CNT (black), CNT with 4nm MoO_3 (blue), CNT with 8 nm MoO_3 (red), and CNT with 16 nm MoO_3 (Pink).

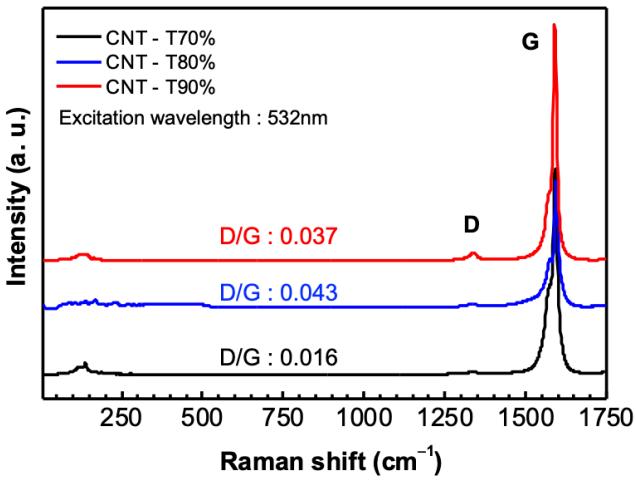

Figure 3.3.2 Raman spectra of as-prepared 70T%-CNT film (black), 80T%-CNT film (red), 90T%-CNT film (red).

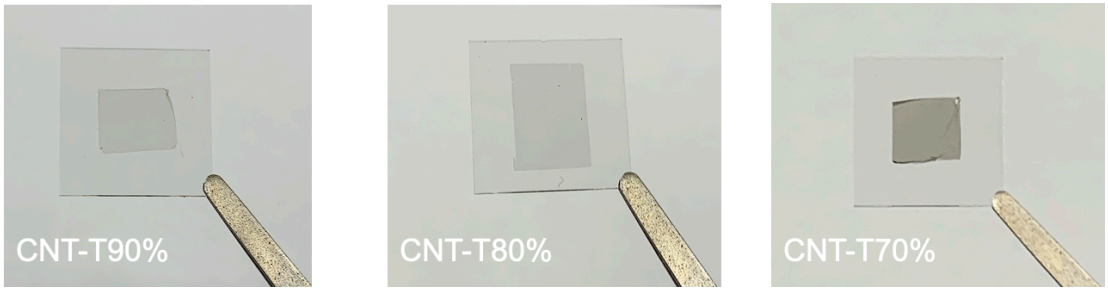

Figure 3.3.3 CNT film having different optical transparency (70T%, 80T%, and 90T%) on 1.5 cm x 1.5 cm glass substrate.

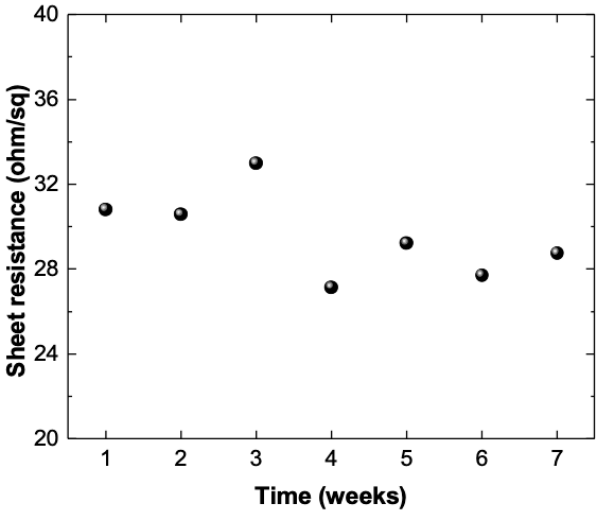

Figure 3.3.4 Measured sheet resistance of 8 nm MoO_3 deposited CNT-T70% film for 7 weeks.

3.4 TEM observation of MoO_3 deposition on CNTs

TEM was conducted on the 4 nm MoO_3-deposited CNT to analyze how MoO_3 develops on CNT. The TEM image in Fig. 3.4.1a shows MoO_3-deposited CNTs over a large area. It shows some partially covered CNTs and fully-covered CNTs with MoO_3. Also, we can see that MoO_3 can be efficiently deposited on single CNT as well as CNT bundles. Fig. 3.4.1b shows the enlarged TEM image of partially-covered CNTs with MoO_3. Local nanoscale domains (area 1, area 2, area 3) of MoO_3 with different crystal orientation is observed on CNTs. Lattice spacing of local nanoscale domain was 0.279

nm and 0.271 nm. TEM image of fully-covered CNT with MoO_3 is shown at Fig. 3.4.1c. We can mainly observe amorphous MoO_3 crystals with a few crystalline domains. From this observation, we suspect that during thermal deposition of MoO_3, MoO_3 crystal on CNT develops as follows (Fig. 3.4.1d). First, separate crystalline nano-domains of MoO_3 grow on CNT. However, since thermal deposition provides relatively high supply rate of precursors, it is hard to slowly grow further nano-crystal domains maintaining crystalline nature. Furthermore, owing to the extra bending energy of 2D layers of MoO_3 by high-curvature CNT surfaces, followed MoO_3 grows in amorphous structure. Therefore, most of MoO_3 crystals surrounding CNTs grow as amorphous.

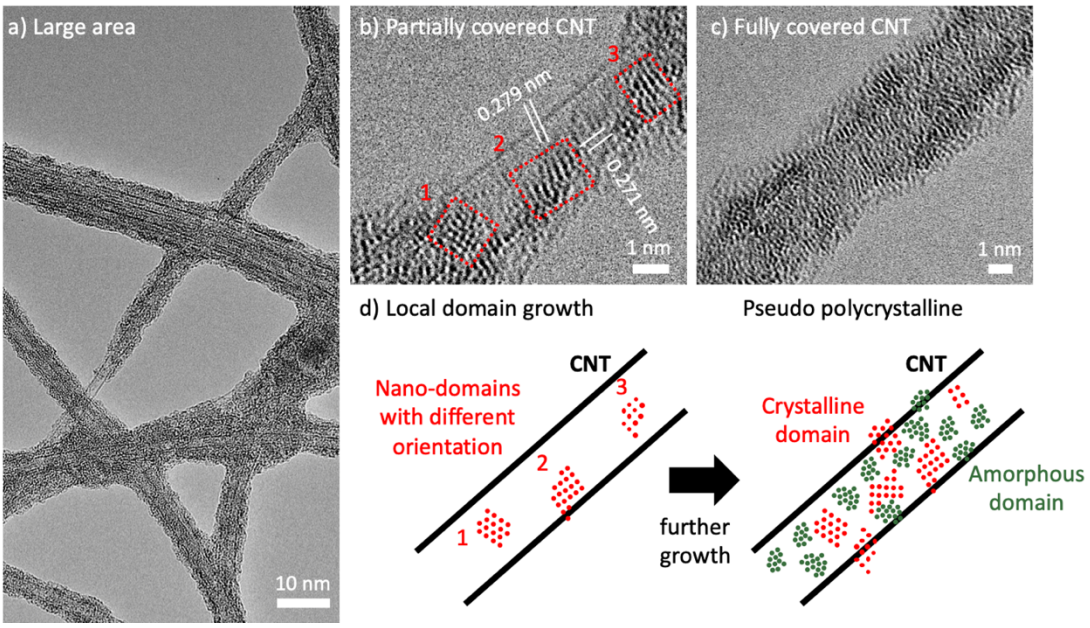

Figure 3.4.1. TEM images of 4 nm MoO_3 deposited CNT. TEM images of (a) Large area, (b) partially covered CNT with MoO_3, (c) fully covered CNT with MoO_3. (d) Illustration depicting the MoO_3 deposition on CNT starting from local domain to pseudo polycrystalline tube.

3.5 Top-laminated CNT film porosity and its doping compatibility with MoO_3

CNTs with different optical transparency synthesized by aerosol CVD have different CNT density owing to the difference in the collection time of aerosol CNT, thus having

different pore size at network structure [34]. This can be also seen from SEM images in Fig. 3.5.1a-c. This means that depending on the CNT density of CNT film, the amount of MoO_3 travelling through CNT network is different. This is important as MoO_3 was previously reported to form unwanted interface state when in direct contact with perovskite [121,122] and the amount of the penetrated MoO_3 through CNT film will harm the underlying perovskite absorber. To analyze the impact of excessive MoO_3 that travels through CNT network on perovskite film, we prepared the CNT-laminated perovskite film on glass and deposited MoO_3 (Fig. 3.5.1d, Fig. 3.5.2). X-ray photoelectron spectroscopy (XPS) was used to characterize interface state formed between the $MAPbI_3$ and MoO_3. We can observe that Pb 4f peaks shift toward lower binding energy as the CNT density of the film decreases. This indicates the formation of metallic Pb^{2+} at the interface induced by chemical reaction between MoO_3 and $MAPbI_3$. This is consistent with Mo 3d peak shifting toward lower binding energy as the CNT density decreases. This implies that more MoO_3 is being reduced upon the direct contact with $MAPbI_3$ where CNT density is lower. Therefore, we can conclude that dense CNT film is more compatible with the direct deposition of MoO_3 on CNT where CNTs are laminated on top of the perovskite absorber, minimizing the perovskite degradation.

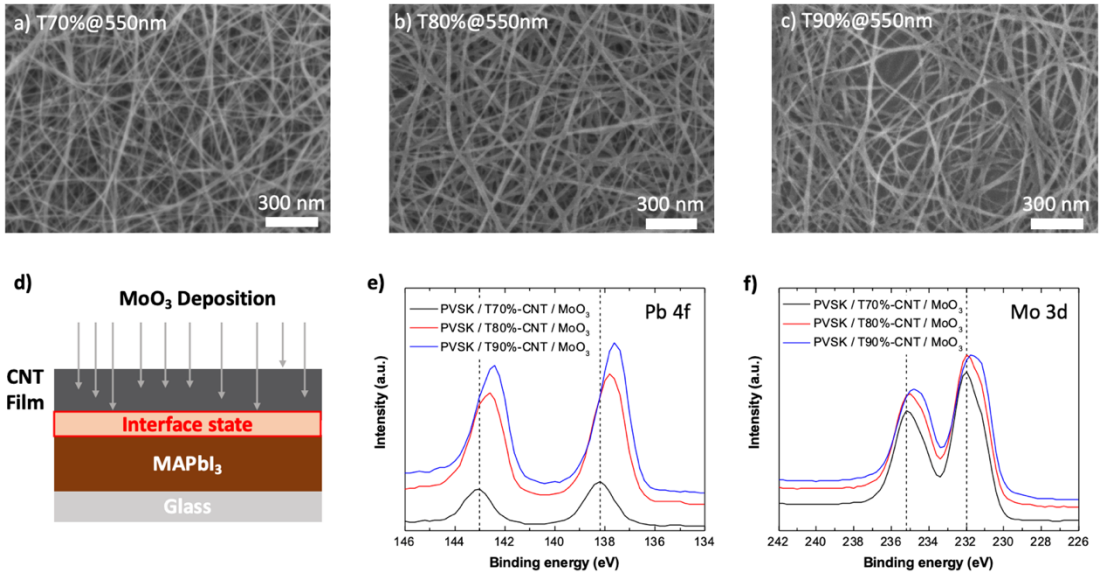

Figure 3.5.1. SEM images of (a) T70% CNT film, (b) T80% CNT film, (c) T90% CNT film. (d) illustration of MoO_3 deposition on CNT/$MAPbI_3$/Glass sample.

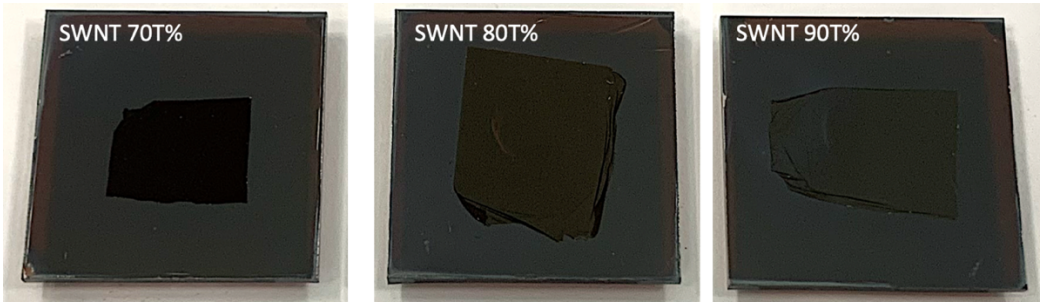

Figure 3.5.2. CNT-laminated-$MAPbI_3$ samples of CNT that has different optical transparency.

3.6 Optimization of the CNT-laminated-PSC fabrication step for MoO_3 doping compatibility.

To further investigate MoO_3 doping compatibility with porous CNT film laminated on perovskite film, we first fabricated CNT-laminated PSCs with MoO_3 deposition. MoO_3 was deposited after CNT lamination on perovskite absorber, followed by deposition hole transport material, Spiro-OMeTAD. However, when less dense CNT films of T80% and T90% were employed, we observed severe performance drop in

PSCs from 17.80 % to 2.83 % in T80% CNT and 16.16 % to 2.44 % in T90% CNT (Fig. 3.6.1c, Table 3.6.1). This arises from the pronounced formation of interface state between $MAPbI_3$ and MoO_3, discussed in Chapter 3.5. Thus, to minimize direct contact between deposited MoO_3 and bare perovskite film, we first drop-casted Spiro-OMeTAD after CNT lamination and deposited MoO_3 on top of CNT / HTL composite (Fig. 3.6.1a-b). This was able to inhibit the formation undesirable interface state as well as achieve efficient doping of laminated CNTs. Successful doping of CNTs can be confirmed by enhanced open-circuit voltage (V_{oc}) and fill factor (FF) (Table 3.6.1., Fig. 3.6.1c) compared to reference devices.

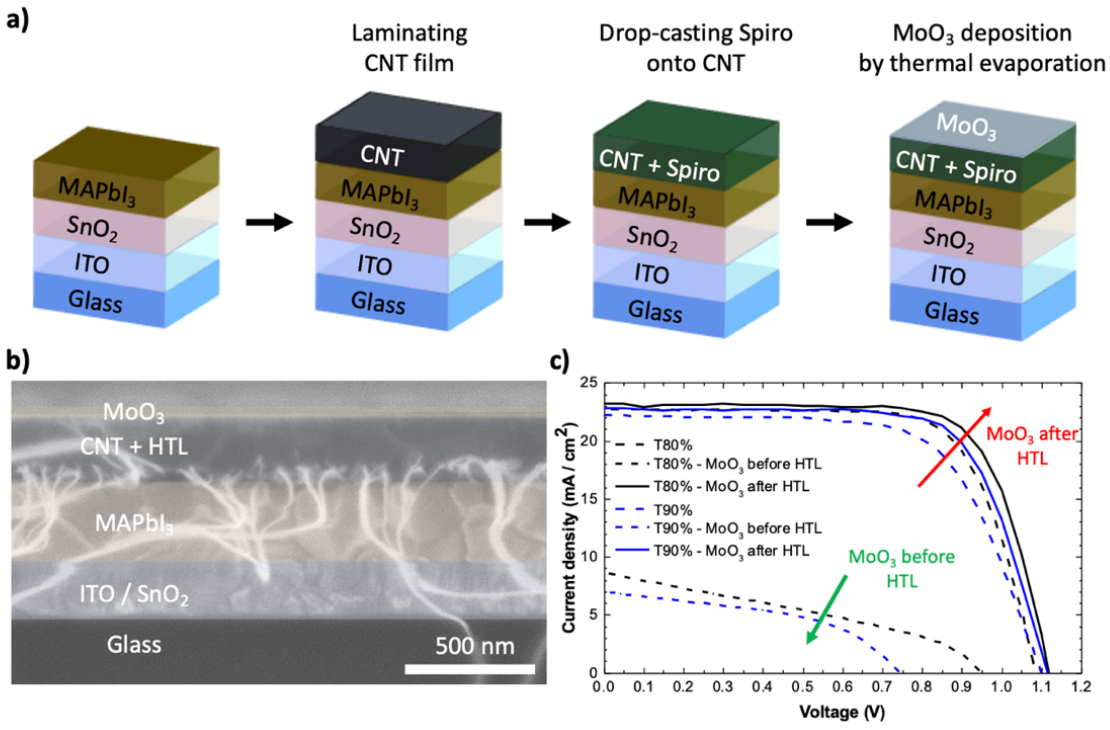

Figure 3.6.1. (a) Schematic illustration showing lamination of carbon nanotube (CNT) on perovskite thin films followed by thermally evaporating MoO_3 under vacuum onto CNT and drop-casting of a spiro-MeOTAD solution for device fabrication. (b) Measured sheet resistance of CNT film with different evaporated MoO3 thickness. (c) Raman spectra of bare CNT (black) and CNT with 4 nm (blue) and 8 nm (red) thermally evaporated MoO_3. (d) Vis-NIR spectra of bare CNT (black), CNT with 8nm thermally evaporated MoO_3 (red) and CNT with 8 nm thermally evaporated MoO_3 (blue).

Table 3.6.1. Photovoltaic Performance of CNT Top Electrode-Based PSCs with

4nm MoO_3 applied before and after HTL deposition under 1 sun (AM 1.5 G, 100 mW / cm^2)

	Device ID	J_{sc} (mA /cm^2)	V_{oc} (V)	FF	PCE (%)
CNT T80%	Bare	22.68	1.09	0.72	17.80
	4 nm MoO_3 before HTL deposition	8.65	0.95	0.34	2.83
	4 nm MoO_3 after HTL deposition	23.17	1.12	0.73	19.05
CNT T90%	Bare	22.24	1.10	0.66	16.16
	4 nm MoO_3 before HTL deposition	7.00	0.74	0.47	2.44
	4 nm MoO_3 after HTL deposition	22.77	1.12	0.71	18.14

3.7 Perovskite solar cell fabrication with MoO3-doped SWNT Top electrode

Although CNT films of T80% and T90% was not dense enough to allow direct MoO_3 deposition on bare CNTs, more dense CNT film of T70% was able to accompany the direct MoO_3 deposition on bare CNTs. This is because dense CNTs with small pore size can efficiently trap the MoO_3 inside CNT film, preventing the direct contact of MoO_3 with perovskite photoactive layer. Further, we optimized MoO_3 deposition thickness on top of CNT T70%. Although higher deposition thickness of MoO_3 leads to higher doping impact on CNTs, we cannot merely employ thicker MoO_3 on CNT. This is because thick MoO_3 will fill up the pores of CNT film. They limit the hole-transporting ability as they accommodate small amounts of Spiro-MeOTAD. We analyzed the SEM and AFM images of CNT T70% with 8 nm, 16 nm MoO_3 deposition thickness (Fig. 3.7.2). The pores of CNT film with 16 nm MoO_3 were found to be mostly filled with lowest rms value of 6.53 nm (Fig. 3.7.2c, f). As expected, CNT-laminated PSCs with 16nm MoO_3 gave the lowest device performance compared to 0 nm (reference), 4 nm, 8nm MoO_3 CNT laminated-PSCs. CNT-laminated PSCs with 8 nm MoO_3 gave the

highest PCE of 20.25 %. This was the highest PCE achieved CNT-based PSCs (Fig. 3.7.3).

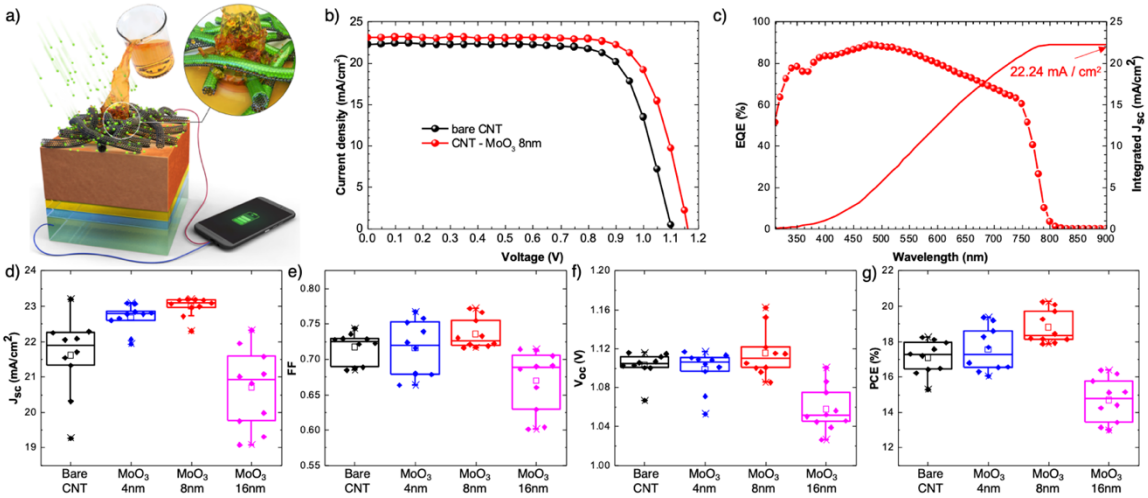

Figure 3.7.1 (a) A schematic illustration showing CNT-laminated perovskite solar cells with MoO_3 doping. (b) Current density- voltage (*J-V*) curves of the highest efficiency perovskite solar cells incorporating bare CNT and CNT doped with MoO_3 8 nm. (c) EQE spectra and corresponding integrated short-circuit current density (J_{sc}) of the device based on CNT doped by 8 nm thick MoO_3. (d) short-circuit current (J_{sc}), (e) open circuit voltage (V_{oc}), (f) fill factor (FF) and (g) power conversion efficiency (PCE) of the perovskite solar cells incorporating bare CNT and CNTs doped with MoO_3 (4, 8 and 16 nm of MoO_3).

Table 3.7.1 Photovoltaic Performance of CNT Top Electrode-Based PSCs with different MoO3 thickness under 1 sun (AM 1.5 G, 100 mW / cm²)[a]

Device ID	J_{sc} (mA /cm²) [average]	V_{oc} (V) [average]	FF [average]	PCE (%) [average]
Bare CNT	22.25 [21.80±1.11]	1.103 [1.103±0.014]	0.743 [0.717±0.022]	18.24 [16.71±0.84]
MoO_3 4 nm	22.78 [22.31±1.14]	1.109 [1.098±0.020]	0.767 [0.715±0.038]	19.37 [17.54±2.83]
MoO_3 8 nm	23.09 [22.92±0.31]	1.162 [1.120±0.028]	0.755 [0.739±0.022]	20.25 [18.80±0.93]
MoO_3 16 nm	21.58 [19.67±1.11]	1.052 [1.058±0.264]	0.713 [0.669±0.043]	16.18 [14.64±1.18]

[a]The photovoltaic parameters are the best values with averages and error ranges in parentheses.

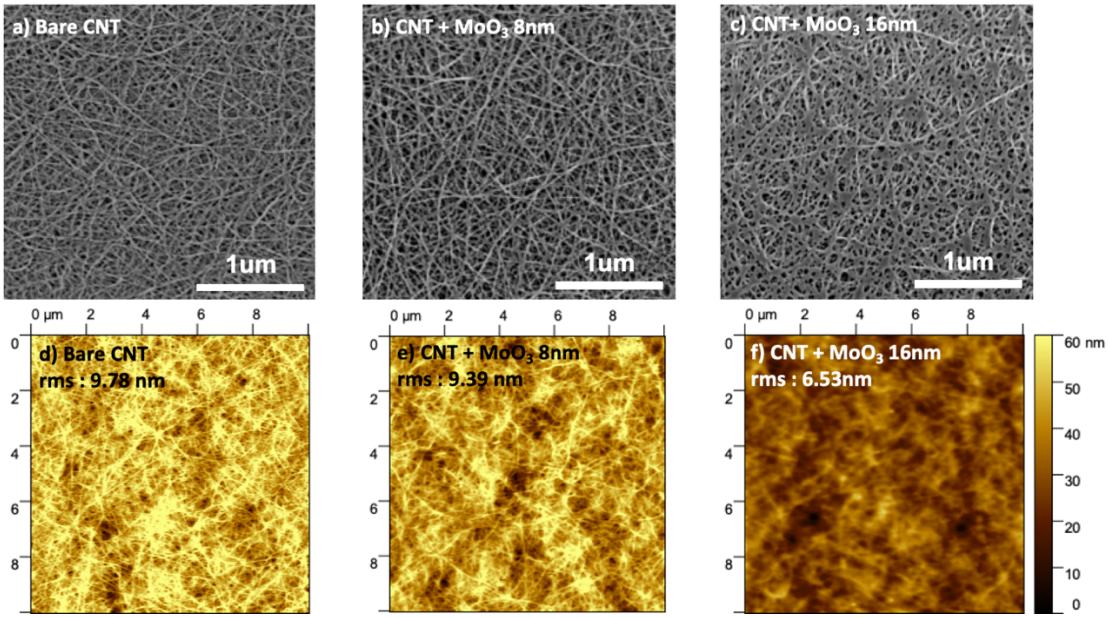

Figure 3.7.2 SEM images of (a) Bare CNT, (b) CNT with MoO_3 8 nm, (c) CNT with MoO_3 16 nm.

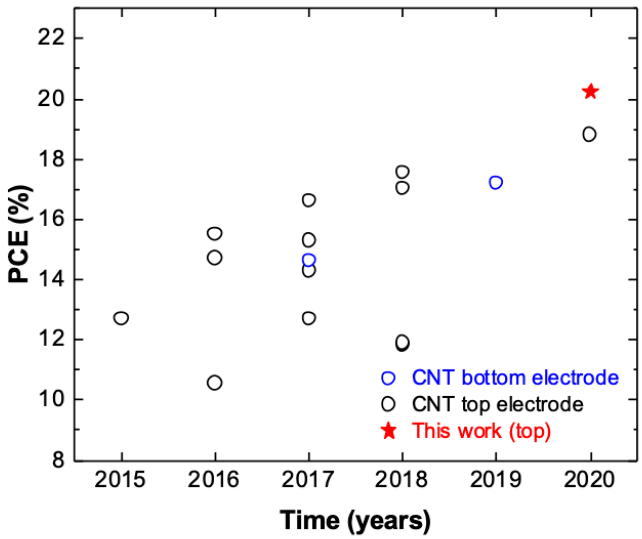

Figure 3.7.3 PCE chart of CNT-based PSCs from 2015.

3.8 Enhanced charge extraction from favorable band alignment of MoO_3-doped SWNT Top electrode

To clarify the reasons behind the improved device parameters, we studied the work functions of CNTs and resulting charge transport properties by photoelectron yield

spectroscopy (PYS) and photoluminescence (PL) measurement. PYS data of MoO_3-doped CNT films reveals that the Fermi level of CNT decreases with the increase in the MoO_3 deposition thickness. As the deposition thickness increases, the Fermi level of the CNT shifted from 4.87 (bare) to 4.98, 5.05, and 5.17 on 4, 8 and 16 nm MoO_3 thickness. The increased work function with the increased deposition thickness can arise from the increase in hole concentration, owing to the thicker MoO_3, which is in good agreement with the sheet resistance and optical absorption analysis in Fig. 3.3.1. According to the energy diagram in Fig. 3.8.1b, the higher work function induced by thicker MoO_3 deposition is energetically favorable in decreasing the potential loss with regard to hole extraction, which can be the origin of the improved V_{oc}. The charge transfer dynamic was analyzed by steady-state PL measurement in Fig. 3.8.1c. The PL intensity of bare perovskite film in contact with a glass substrate significantly quenched when in contact with bare CNT. With 8 nm MoO_3 deposition, the PL quenching became more significant, implying better hole transfer capability of the CNT with MoO_3 doping. The better hole extraction ability after MoO_3 was further confirmed by electrochemical impedance spectroscopy (EIS) measurement. Figure 3.8.1 shows the Nyquist plots of the bare CNT-laminated PSCs and MoO_3-doped-CNT-laminated PSCs under illumination. The corresponding equivalent circuit is shown at Figure 3.8.3a. It is known that in the EIS analysis, the high frequency component implies the series resistance (R_s) and lower frequency components represents charge recombination resistance (R_{rec}). The numerical fitting of EIS data gives the parameters shown in Figure 3.8.3b-c. Obviously, compared with the R_{rec} from the bare CNT sample, MoO_3-doped CNT sample shows higher R_{rec} under all voltage bias conditions. This higher R_{rec} indicates the reduced non-radiative recombination of charges within the PSC devices, again owing to higher charge extraction ability from MoO_3-doped CNTs. This is consistent with dark current measurement, showing MoO_3-doped-CNT-based PSC lower dark current than bare CNT-based PSC, indicating reduced non-radiative recombination owing to MoO_3 doping on CNT.

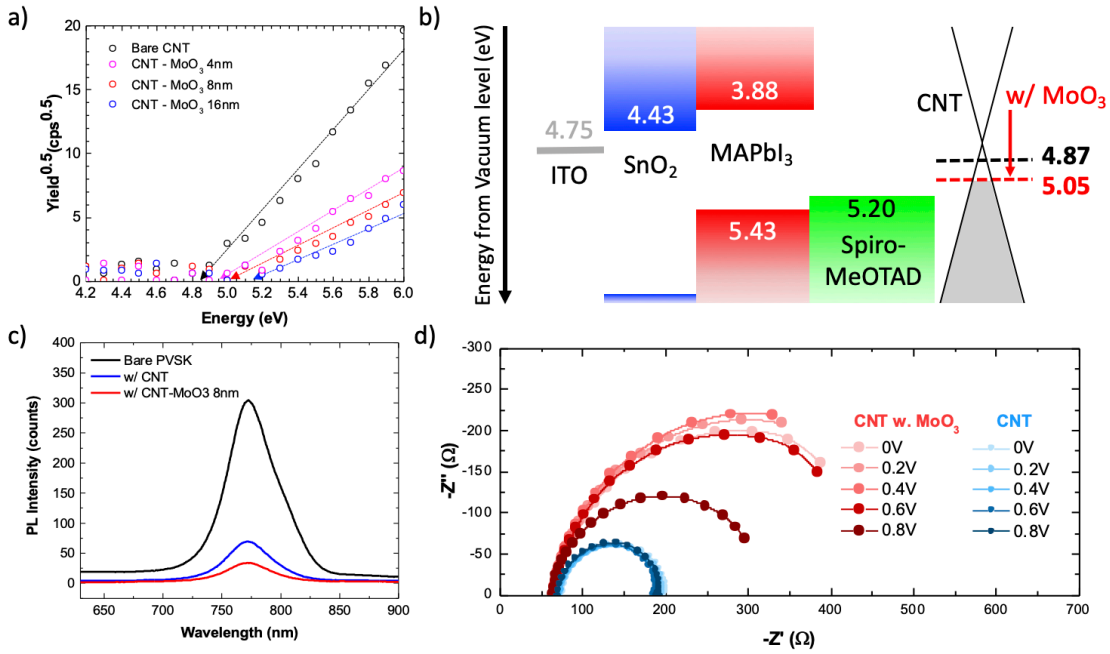

Figure 3.8.1 (a) Photoelectron yield spectroscopy (PYS) measurement data of bare CNT, CNT with 4 nm, 8 nm, and 16 nm MoO_3. (b) Band alignment in the planar heterojunction perovskite solar cells without and with doping of the CNT. (c) Steady-state photoluminescence (PL) spectra of bare perovskite film and perovskite films in contact with bared CNT and CNT doped by MoO_3. (d) Nyquist plots of bare CNT and CNT doped by MoO_3 from the impedance measurement under 0, 0.2, 0.4, 0.6, and 0.8 V voltage bias.

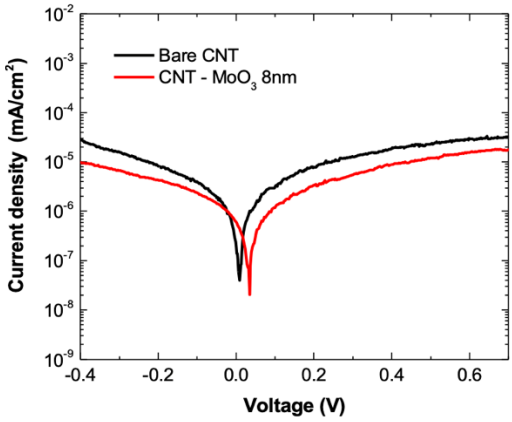

Figure 3.8.2 Dark current measurement of bare-CNT-laminated PSCs and 8 nm-MoO_3-deposited CNT-laminated PSCs.

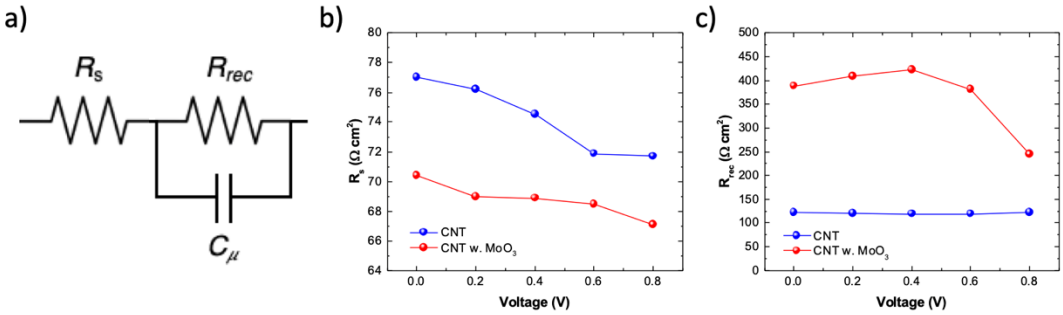

Figure 3.8.3 (a) Equivalent circuit of EIS measurement used for fitting parameters. (b) R_s (c) R_{rec} from EIS measurement with bare CNT-based PSC (blue) and 8 nm-MoO_3-doped-CNT-based PSC (red).

3.9 Four-terminal perovskite/Si tandem application

In addition to the increased efficiency of CNT-laminated PSCs upon MoO_3 doping, we further investigated the integration of CNT-laminated PSCs in tandem with Si solar cells (Fig. 3.9.1a). First, optical transmittance of top CNT-laminated PSCs with MoO_3 doping on CNT films of T70%, T80% and T90% was measured ranging from visible to near infrared region and was compared with that ITO-based PSCs, which was reported in previous report [33]. The transmittance spectra shows that CNT film of T80%, T90% shows higher optical transmittance over 1000 nm wavelength regime. This is ascribed to the parasitic absorption of ITO in infra-red region. Also, as expected, CNT film of T70% exhibited the lowest optical transmittance over all wavelength regime, owing to the highest thickness of the film. To elucidate the feasibility when in conjunction with bottom Si solar cell, we simulated bottom Si solar cell using COMSOL Multiphysics® semiconductor module under 1 sun illumination. As compared to 14.84 % PCE when illuminated 1 sun, Si bottom cell showed 3.01, 4.18, 4.15 and 3.96 % PCE when filtered PSCs with CNT film of T70%, T80%, T90% and ITO, respectively. Regarding total PCE as perovskite/Si tandem, MoO_3-doped-CNT-T70%-laminated PSCs with Si bottom cell showed the highest PCE of 23.26 %, despite the lowest optical transmittance of top PSC subcell. This is because of extremely

efficient top PSC subcell having 20.25 % PCE. Tandem PCE of MoO_3-doped-CNT-T80%-laminated PSC was almost in par with that of MoO_3-doped-CNT-T70%-laminated PSC, owing to high optical transparency of top PSC subcell. It is worth noting that the top PSC subcell with CNT-T80%, CNT-T90% is not optimized, which, we predict by further improving the top PSC subcell with CNT-T80%, CNT-T90%, we can definitely aim for higher PCE.

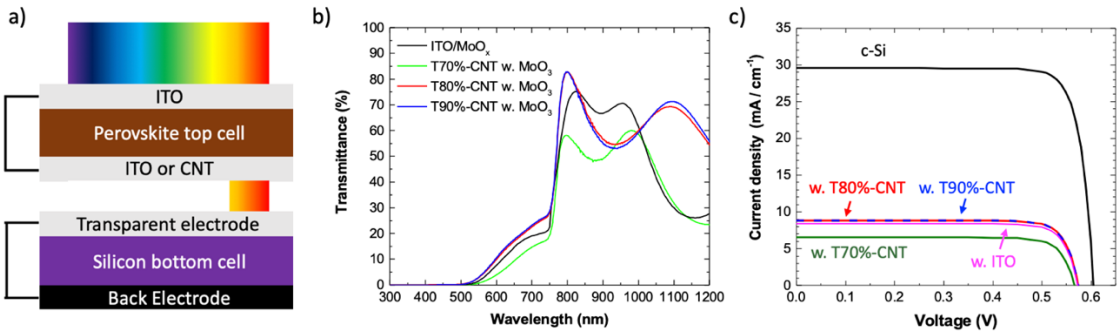

Figure 3.9.1 (a) Schematics of CNT transparent electrode laminated perovskite in tandem with silicon bottom cell (b) Transmittance of top perovskite sub cell, (c) Simulated J-V curve of bare Si, filtered Si with T70%-CNT top cell, filtered Si with T80%-CNT top cell, filtered Si with T90%-CNT top cell, filtered Si with ITO top cell.

Table 3.9.1 Photovoltaic Performance of CNT Top Electrode-Based PSC in tandem with simulated SiSC under 1 sun (AM 1.5 G, 100 mW / cm^2)

	Device ID	J_{sc} (mA /cm^2)	V_{oc} (V)	FF	PCE (%)
	Si	29.52	0.60	0.82	14.84
	Filtered Si	6.49	0.57	0.81	3.01
CNT-T70	Semi-transparent top perovskite	23.09	1.16	0.76	20.25
	Tandem	-	-	-	23.26
	Filtered Si	8.82	0.58	0.82	4.18
CNT-T80	Semi-transparent top perovskite	23.17	1.12	0.73	19.05
	Tandem	-	-	-	23.23
	Filtered Si	8.81	0.58	0.81	4.15
CNT-T90	Semi-transparent top perovskite	22.77	1.12	0.71	18.14
	Tandem	-	-	-	22.29
	Filtered Si	8.38	0.58	0.81	3.96
ITO	Semi-transparent top perovskite	21.7	1.01	0.72	15.96
	Tandem	-	-	-	19.92

3.10 Summary

In summary, we introduced an effective MoO_3 doping of CNT top electrode for implementation of efficient semi-transparent perovskite solar cells. The MoO_3 doping by thermal deposition on CNTs enabled enhancement of conductivity with a favorable alignment of work function without damaging underlying organic charge selective layer and perovskite absorbers. Owing to improved conductivity with a favorable energy alignment, we achieved a PCE of 20.25 % from CNT-electrode-laminated PSCs. It is worth mentioning that our method is simple, reproducible, and easily applicable to large area module process. As the record-high PCE showcases, we successfully offered a solution to tacking with the efficiency limit in CNT-laminated PSCs. Further incorporation with bottom Si solar cell, the total PCE can be even higher. We believe this method can provide the pathway for achieving higher performance and their potential versatile application for flexible and stretchable devices.

Chapter 4:

Conclusions

4.1 Conclusions

In conclusion, this thesis focused on the application of functionalized CNTs into solar cells by designing the functionalization method and fabricating the subsequent solar cells. Moreover, their roles within the solar cell devices were analyzed with various characterization methods.

First, we first reported the application of highly purified and functionalized s-SWNTs to improve the crystal quality of perovskite film. A small addition of DOC functionalized s-SWNTs into perovskite precursor was found to efficiently induce Lewis-adduct formation with perovskite precursor PbI_2, thus resulting larger and smoother perovskite grains with escalated nucleation energy. Furthermore, the s-SWNTs as cross linkers embedded between the grain boundaries benefited the charge extraction from perovskite absorbers, reducing non-radiative recombination in PSCs, resulting increased open circuit voltage (V_{oc}). Analyzing the role of functionalized s-SWNTs as growth template during nucleation stage provided a comprehensive understanding of the functionalized CNTs as efficient additive to perovskite precursor. This was able to boost up the PCE of PSCs from 18.1 % to 19.5 %.

Second, the efficient p-doping of CNT top electrodes with MoO_3 thermal deposition was achieved without damaging underlying PSC devices. This is attributed to the stable nature of MoO_3, which is solvent-free and non-acidic. MoO_3 doping of CNTs enabled the increased conductivity with suitable energy alignment of CNTs. The improved

charge dynamics was observed with the pronounced PL quenching from MoO_3-doped-CNT sample, as well as lower starting point and large semi-circle from the Nyquist plots in EIS measurement. The obtained PCE of 20.25 % currently stands as the highest PCE among the reported CNT-based PSC solar cells. The potential of the MoO_3-doped CNT-PSCs were evaluated by stacking them to SiSCs and simulating the 4-terminal tandem solar cells. The enhanced transparency in both visible and near-infrared region through the minimum parasitic absorption of MoO_3 demonstrated expected higher performance of the MoO_3-doped CNT-PSCs compared with ITO-based semi-transparent PSCs.

4.2 Prospects

The additive scheme with the functionalized CNTs employed here for the first time was very successful. The compatibility of this technique with other functionalized CNTs will pave a new pathway to incorporate the dispersed and functionalized CNTs into perovskite film. Follow-up project of the work reported in this thesis was also reported by further designing dispersing agent with high mobility and more Lewis base sites [36]. Also, functionalizing CNTs with conventional organic hole transport polymers can be an ideal combination that already ensures efficient charge transfer.

MoO_3 CNT top electrode doping technique is available on any solar cell devices with CNT top electrodes. This could be also efficient for graphene transparent top electrode if the reproducible transfer method is developed. The CNT-laminated-perovskite / Si tandem can be further optimized through employing antireflection layer on top of both CNT electrodes and glass in top perovskite subcell. This will reduce the optical loss from the top perovskite subcell, which will benefit more efficient light transmission to bottom Si solar cell. In addition, applying antireflection layer on top of MoO_3-doped-CNT will also provide the encapsulation effect, that can enable long term doping stability of MoO_3.

Chapter 5:

Appendix:

Tailoring the surface morphology of carbon nanotube forest by plasma etching: a parametric study

5.1 Research Background and Introduction

Carbon nanotube (CNT) forests, which represent arrays of vertically aligned CNTs, have initiated great potentials as a functional material due to their tunable electrical, thermal and mechanical properties. The structural alignment, size and density of CNTs can be well controlled by many pre- [123,124] and post-treatments [125], providing interesting nanoporous backbone structures for different applications. Accordingly, CNT forests have been reported as a promising material in the fields of lithium-ion battery electrodes [126], energy storage [127], thermal interface materials [128], gas sensors [129], adhesive joining [130], filtration membranes [131,132], and others.

CNT forests are typically produced by chemical vapor deposition (CVD) [133]. During the CVD process, the close proximity between the neighboring CNTs induces van der Waals interaction and enforces the CNTs to self-align perpendicular to the

substrate [134]. Such CNT forest growth kinetics accompany the formation of a "crust" layer [135] on the top of the forest (i.e., the initial stage of growth), encompassing randomly oriented entangled CNTs [136] and carbonaceous impurities [137]. It has been suggested that the entanglement of CNTs in the crust improves height uniformity of the CNT forest [138].

However, tailoring of the top surface of CNT forests is important to engineering of many applications. For instance, use of CNT forests as thermal and electrical contacts relies on the compliance and the morphology of the outward-facing CNTs, and presenting a surface with vertically oriented CNTs that can individually act as nanoscale contacts is key to achieve low overall contact resistance. Further, the stiffness of the top crust is significantly greater than the vertically aligned portion (i.e., the bulk of the forest), which is not desirable for compliant CNT-based electrical and thermal interface materials. Further, CNT forests can be used as high resolution printing stamps [139], but the crust layer should first be removed to enable appropriate contact and ink transfer. In processes using elastocapillarity to densify CNT forests into solids [140,141], the crust layer should be also removed beforehand since it constrains lateral movement of CNTs during densification. The density and morphology of CNTs in films and forests is also a key parameter for engineering their adhesive properties, such as for use in robotic manipulation and reversible mechanical interfaces [142,143].

Therefore, removal of the crust layer without adversely altering the structure of the CNT forest is of interest for understanding the fundamental surface properties, and for application-oriented engineering of CNT forests. Several methods including oxidation in air [144] and chemical oxidation in solution [145] have been developed for the removal of amorphous carbon. Nevertheless, these techniques can damage CNTs and distort the alignment [146]. On the other hand, plasma treatment [147] can remove the carbon impurities with a solvent-free, time-efficient process. In addition, plasma treatment can provide a wide range of chemical functionality by utilizing diverse gas sources such as N_2, Ar and O_2. For example, O_2 plasma can offer oxygen functional

groups to CNT surfaces which can act as active sites for biochemical sensing [148] and biomedical applications [149].

Herein, we study the use of Ar / O_2 plasma to controllably remove the crust layer from CNT forests synthesized by atmospheric pressure CVD. We investigate the effect of plasma etching parameters, including power, exposure time, gas flow rate and mixture composition, on the etching behavior using both qualitative (SEM and optical microscopy) and quantitative (AFM, Raman spectroscopy and XPS) characterization. We discuss the optimal plasma conditions for the crust removal without changing the structural shape and internal CNT alignment. Furthermore, we assess the correlation between the etching rate and the initial CNT forest density, leading to guidelines for controlled surface modification of CNT forests.

5.2 Materials and methods

5.2.1 CNT forest synthesis

CNT forests were grown by thermal CVD in a tube furnace (Thermo Fisher Minimite, 22 mm inner diameter quartz tube). The catalyst for CNT growth was patterned by photolithography on a (100) silicon wafer with 300 nm of thermally grown silicon dioxide, followed by lift-off processing using ultrasonic agitation in acetone. The supported catalyst layer, 10 nm of Al_2O_3 beneath 1 nm of Fe, was deposited by electron-beam evaporation. The wafer with the deposited catalyst was diced into 20×20 mm pieces and placed in the tube furnace for CNT growth.

CNT forest samples were prepared by three different CVD recipes, referred to as Reference, Decoupled, and Carbon-assisted. The Decoupled growth recipe [124] started with flowing 100 / 400 sccm of He / H_2 while heating the furnace up to 775 °C for 10 min (ramping step) and then inserting the wafer into the furnace with a magnetically coupled transfer arm. The system was then held at 775 °C for 10 min with the same gas flow rates (annealing step). For CNT growth, the gas flow was changed

to 100 / 400 / 100 sccm of C_2H_4 / He / H_2 at 775 °C for 3 min. After CNT growth, the furnace was cooled to <100 °C with the same gas flow and finally purged with 1000 sccm of He for 5 min, before removing the sample. The Reference growth recipe [150] ran with the same annealing and growth conditions with the Decoupled recipe, but the sample was stationary inside the furnace during the entire growth process. The Carbon-assisted growth [123] recipe also ran with the same annealing and growth conditions with the Decoupled recipe, but prior to the annealing step, the furnace tube was "pre-loaded" with carbon deposits from thermal decomposition of C_2H_4, which results in a higher nucleation density of CNTs.

5.2.2 Plasma treatment.

The CVD-grown CNTs were exposed to Ar / O_2 plasma using a Diener Femto Plasma system with following parameters: Argon and Oxygen gas flow rates of 0-30 sccm, plasma power of 0-100 W, exposure time of 0-30 min at ~200 mTorr. CNT forests were placed in a vacuum chamber on the cathode of plasma generator and feed gases were introduced to initiate the reaction while the volatile by-products from plasma etching are removed by the vacuum system.

5.2.3 Characterization of CNT forests.

Scanning electron microscopy (SEM) were carried out to visualize the CNT surface morphology and alignment. Raman scattering measurements (inVia, Renishaw) were used to characterize the CNTs with the excitation laser wavelength of 532 nm. Atomic force microscopy (AFM; SPI3800N, Seiko Instrument Inc.) topography images were recorded in tapping mode. AFM images were further analyzed with Gwyddion software to calculate the roughness and CNT tip density. Core level photoemission measurements were performed by XPS (PHI 5000 VersaProbe) using monochromatic

Al Kα radiation. The XPS resolution was estimated to be ≈1 eV and the energy offset was calibrated using the surface C 1s peak. The XPS C 1s peak was deconvoluted into five components employing the Gaussian and Lorentzian functions. Optical images were collected by optical microscope (Olympus, BX-53) under both bright and dark field illumination.

5.3 Result and discussion

5.3.1 Modifying the morphology of CNT forests via Ar / O_2 plasma etching

As shown in Fig. 5.3.1a, surface modification by plasma etching occurs by both ion bombardment and chemical reaction, Fig. 5.3.1a. Charged ions, neutral atoms and radicals are excited by high voltage applied across the process chamber. The excited ions then collide and react with the atoms of the target surface. Plasma etching using Ar as the feed gas, which is chemically inert, is dominated by the physical effect where its etching is largely based on the ion bombardment through directional momentum transfer. Physical etching is anisotropic but has limitation of low selectivity [151]. On the other hand, plasma etching using O_2 as the feed gas, which is in general highly reactive, is dominated by chemical effects where the process involves transport of reactive species through diffusion and reaction with the target surface. Because the diffusion of reactive species takes place in all directions, O_2 plasma etching is isotropic but can have high selectivity [152].

Depending on the plasma conditions, the result of CNT forest etching (Fig. 5.3.1b) can be 'light' upon which no apparent change occurs, 'modest' where the top crust layer is removed yet the forest structure remains the same, and 'aggressive' where the structure exhibits severe alternation accompanied by significant material removal. We plasma-treated CNT forests for different durations (1min, 5min, 30min) and compared with the as-grown CNTs, Fig. 5.3.1c-j. With longer duration of CNT exposure to the

plasma, excessive etching causes distortion in the microstructure; the plasma "drills" into the forest, and CNTs at the top of the forest aggregate into clusters [153,154]. As such, we can classify the etching conditions as "light" "modest" and "aggressive", spanning various combinations of plasma power, gas flow rate, or mixture composition, for the same plasma exposure time. Therefore, it is necessary to understand the effect of process parameters and control appropriately.

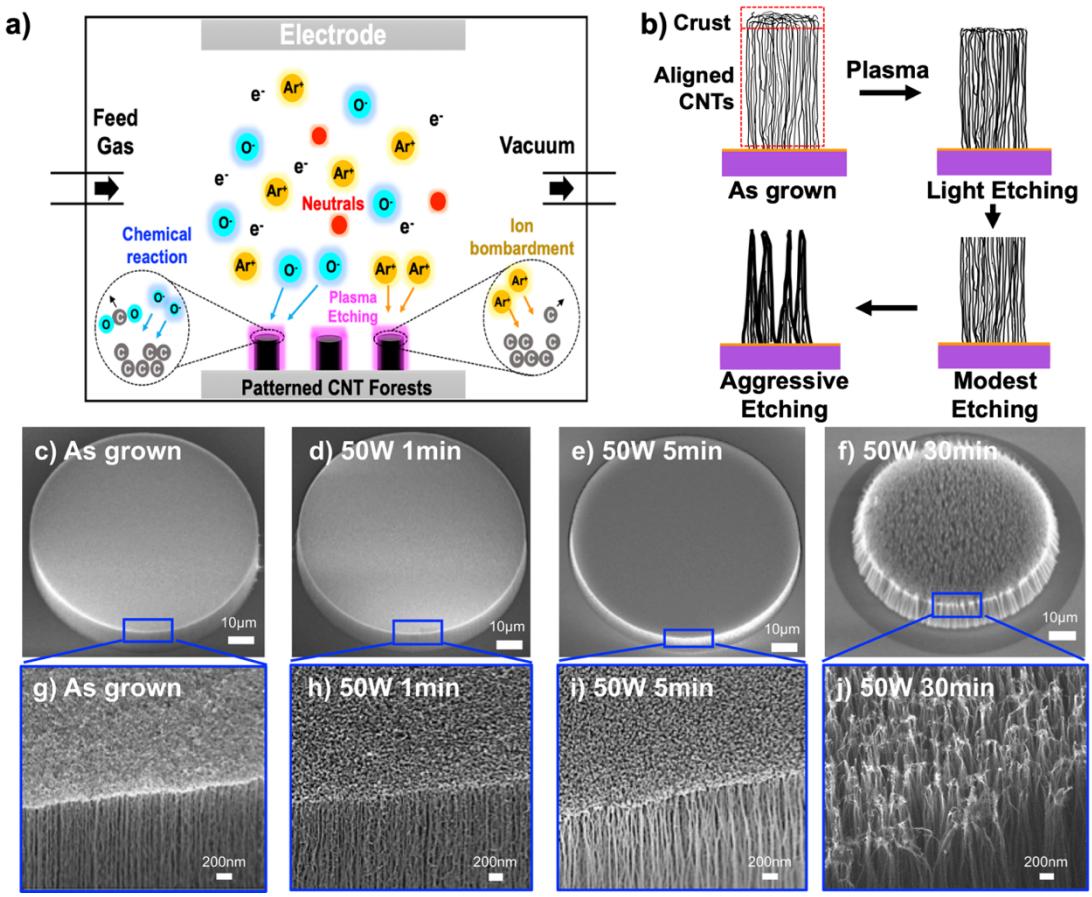

Figure 5.2.1 Modifying the morphology of CNT forests via Ar / O_2 plasma etching. Schematics of (a) plasma etching by excited Ar and O_2 atoms and (b) CNT forests after exposure different etching conditions: as-grown, light etching, modest etching, aggressive etching. (c)-(f) SEM images (tilted view) of plasma-etched CNT forest pillars. (g)-(j) SEM images of enlarged areas (blue rectangles) from (c)-(f).

5.3.2 Effect of plasma power on crust removal and surface modification of the CNT forest

First, plasma power results controls etching behavior at the same plasma exposure time. We exposed the as-grown CNT forests to plasma powers of 30 W, 50 W, 70 W, 100 W for 5 minutes and compared the structural change of top surface, as shown in Fig. 5.3.2. Flows of Ar and O_2 were fixed at 8 sccm and 2 sccm respectively, to exclude the effect of flow rate and gas composition. After plasma treatment at 30 W, the crust layer is still present at the top of the forest, yet the root mean square (RMS) roughness decreases from 30.6 nm (as-grown) to 12.8 nm (Fig. 5.3.2.a and 5.3.2.b). This suggests removal of amorphous carbon from the CNT forest crust [155], and is categorized as light etching. Using higher power of 50 W and 70 W, the RMS roughness increases back to 24.6 nm and 25.8 nm respectively, which accompanies the removal of the crust, exposing the tips of vertically aligned CNTs (Fig. 5.3.2.c). At power of 100 W, the roughness increases significantly, to 211.2 nm, representing aggressive etching. Under this condition, AFM and SEM images show the spiky CNT aggregates on the surface, along with large voids. Dark-field optical microscopy also provides a quick means to interrogate the surface morphology of CNT forests, as the reflectivity decreases due to removal of amorphous carbon on the surface at light and modest etching condition (Fig. 5.3.2.i, 5.3.2.j, and 5.3.2.k) and increases due to the aggregation of CNTs at aggressive etching condition (Fig. 5.3.2.l).

X-ray photoelectron spectroscopy (XPS) analysis was performed to trace the change of surface chemistry due to plasma etching (Fig. 5.3.2.m). Applying 30 W plasma, we observe that the XPS intensity ratio between O 1s and C 1s (I_{O1s} / I_{C1s}) increases, indicating that the CNT forest surface accepted oxygen radicals. At 50 W, I_{O1s} / I_{C1s} drops in a manner consistent with removal of the defective crust layer. Further plasma etching on CNTs with more than 50W power induces defects, distortion and

aggregation of CNTs, as supported by the increased RMS roughness, and increased I_{O1s} / I_{C1s} (Fig. 5.3.2.m, Fig. 5.3.2.n).

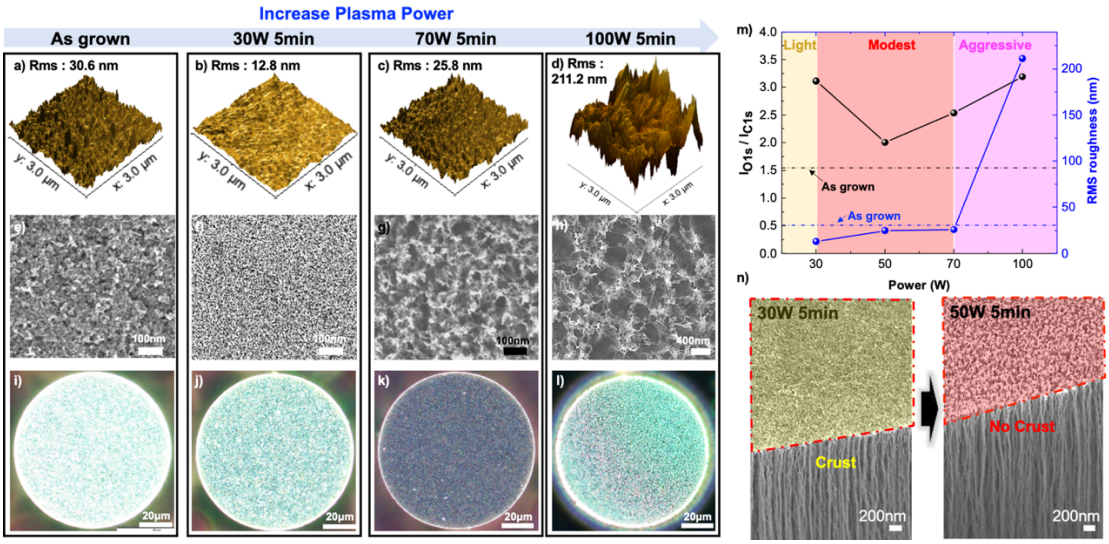

Figure 5.3.3 Effect of plasma power on crust removal and surface modification of the CNT forest. (a)-(d) AFM, (e)-(h) SEM and (i)-(l) optical images of top surface of CNT forests (CVD grown via decoupled recipe), (a), (e), (i) as-grown, and etched using power of (b), (f), (j) 30W, (c), (g), (k) 70W, and (d), (h), (l) 100W for 5 min (same Z-scale). (m) XPS intensity ratio between O 1s and C 1s and corresponding RMS roughness values of plasma treated CNT forests according to plasma power. (n) SEM images of crust removal of CNT pillars after plasma treatment. Exposure time, gas composition and flow rate were 5 min, Ar 8 sccm and O_2 2 sccm respectively.

5.3.3 Effect of gas flow rate on crust removal and surface modification of CNT forests

In addition to the plasma power and exposure time, the etching behavior significantly depends on the flow rate of the feed gas. We compared CNTs after plasma treated with different gas flow rates of 5, 10, and 30 sccm, (Fig. 5.3.3). The gas mixture of 20% O_2 and 80% Ar, plasma power of 50 W and plasma time of 5 min were fixed in this series. The degree of modification was inversely proportional to the flow rate. This is because at flow rates greater than 15 sccm, the active plasma species are pumped away before reacting with the CNTs [156] (Fig. 5.3.3c, 5.3.3f, and 5.3.3i)and the slow flow rate allows active plasma species to react more with the CNT pillar surface (Fig. 5.3.3a, 5.3.3d and 5.3.3g). Therefore, the flow rate regime around 10 sccm corresponds to “modest” etching (Fig. 5.3.3b, 5.3.3e, 5.3.3h, 5.3.3j and 5.3.3k).

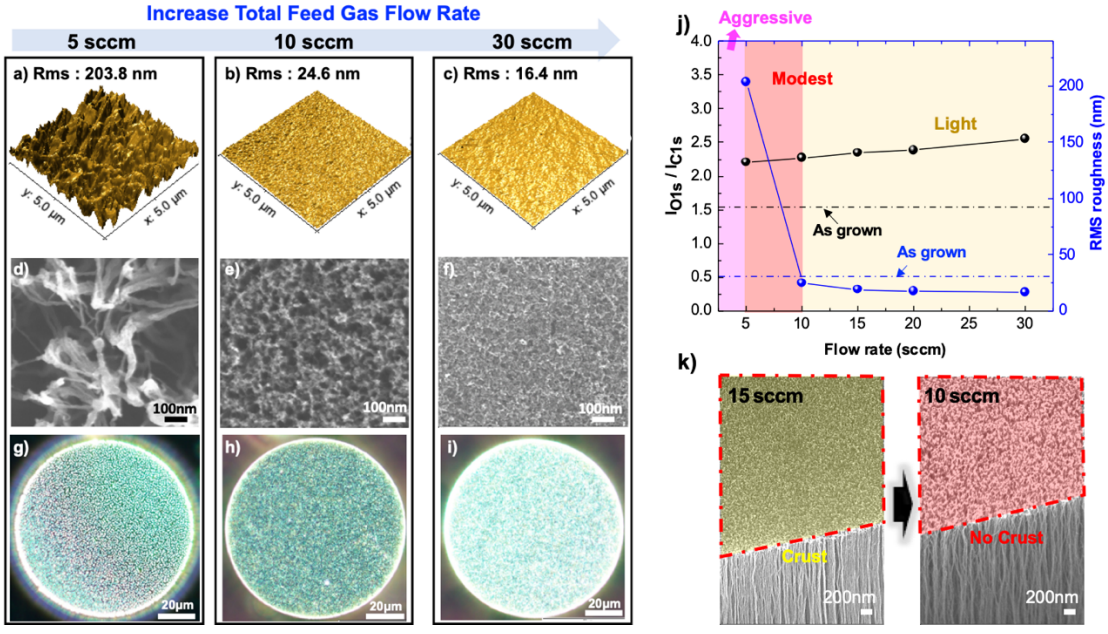

Figure 5.3.4 Effect of gas flow rate on crust removal and surface modification of CNT forests. (a)-(c) AFM, (d)-(f) SEM and (g)-(i) optical images of CNT forest top surfaces after plasma treatment using total gas flow rate of (a), (d), (g) 5 sccm, (b), (e), (h) 10 sccm, and (c), (f), (i) 30 sccm (all with same Z-scale). (m) XPS intensity ratio

between O 1s and C 1s and corresponding RMS roughness values of plasma treated CNT forests according to gas flow rate. (n) SEM images of crust removal of CNT pillars after plasma treatment. Plasma power, exposure time, gas composition were 70 W, 5 min, Ar : O_2 = 4:1, respectively.

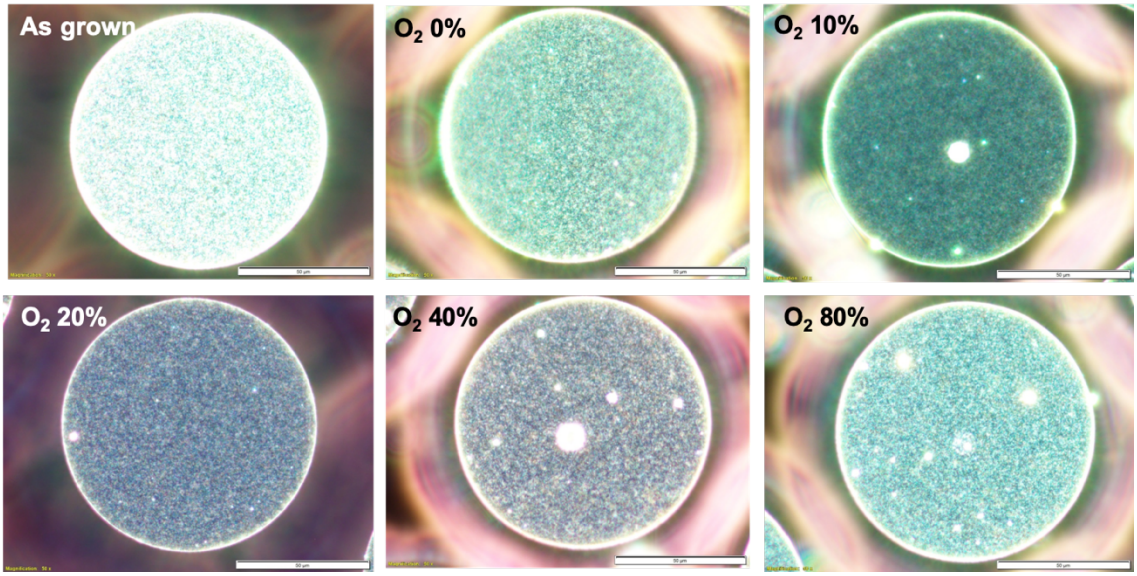

Figure 5.3.3.2 Optical microscope images of Ar / O_2 plasma treated CNT pillar surface grown by Decoupled recipe under different oxygen composition ratio. (Total flow rate was fixed at 10 sccm and exposure time for optical microscopy measurement was 1.25 s.)

5.3.4 Effect of feed gas composition on crust removal and surface modification of CNT forests

The composition of gas mixture is another factor that influences the CNT plasma etching. We treated CNT pillars with different O_2 fraction from 0% to 80%, at 50W, 5 min and 10 sccm. In all cases, plasma etching decreased the RMS roughness, as shown Fig. 5.3.3b and 5.3.4a-c. The O_2 rich (80%) condition (Fig. 5.3.4f and 5.3.4i) was less aggressive than pure Ar (O_2 0%) condition (Fig. 4d and 4g). The plasma density of pure Ar can exceed that of pure O_2 by a factor of 2, owing to the lower collisional energy

loss per electron-ion pair of an inert gas Ar than a molecular gas like O_2 at the same electron temperature[157]. The slightly higher RMS roughness and the qualitative comparison using SEM observation, Fig. 5.3.4e and 5.3.3e, indicate the transition from 'light' etching to 'modest' etching with the introduction of 10% and 20% O_2 gas. The optical microscopy images, Fig. 5.3.4h and 5.3.3h, also show less light scattering on the CNT surface. When the O_2 gas fraction is 40% or greater, we again observe that the CNT crust remains ('light' etching behavior). Therefore, the O_2 fraction for crust removal without degradation to the forest was determined to be ~20% , Fig. 5.3.3e and 5.3.3.2. In Ar rich condition in Ar / O_2 plasma system, chemical etching by O_2 can be accelerated by the help of physical etching from the ion bombardment induced by the Ar plasma, destroying the carbon bonds and therefore reducing the reaction threshold of chemical etching [158,159]. Therefore, we find that a saturation exists for which the active plasma source is not anymore able to accept new O_2 species from the plasma environment because of the oxidation level and molecular steric hindrance [159]. The XPS I_{O1s} / I_{C1s} characterization, Fig. 5.3.4j, also supports such etching behavior. The XPS I_{O1s} / I_{C1s} drops when O_2 fraction is over 10% and this could arise from the removal of crust as well as the CNTs retaining active oxygen species.

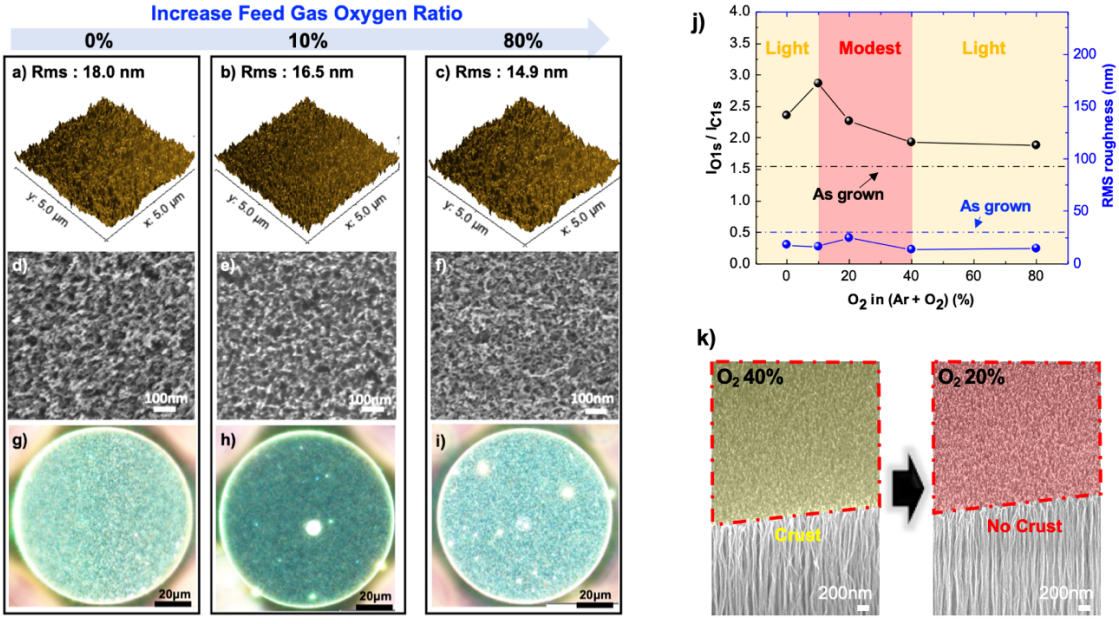

Figure 5.3.5 Effect of feed gas composition on crust removal and surface modification of CNT forests. (a)-(c) AFM, (d)-(f) SEM and (g)-(i) optical images of CNT forest top surfaces (CVD grown via decoupled recipe), after plasma treatment using different oxygen composition ratio of (a), (d), (g) 0 %, (b), (e), (h) 10 %, and (c), (f), (i) 80 %. j) XPS intensity ratio between O 1s and C 1s and corresponding RMS roughness values of plasma treated CNT forests under different O_2 fraction in feed gas. (k) SEM images of crust removal of CNT pillars after plasma treatment under different O_2 fraction in feed gas.

5.3.5 Surface chemistry of CNT forests after Ar / O_2 plasma

To further clarify the chemical reaction between CNTs and Ar / O_2 plasma under different O_2 fraction, we performed XPS C1s peak deconvolution of Ar / O_2 plasma treated CNT pillars under various O_2 fraction. The pristine asymmetric C1s peak is located at the binding energy of 284.0 eV, which is from sp^2-hybridized graphite-like structure (C=C), as shown in Fig. 5.3.51a. The peak located at 284.8 eV is attributed to sp^3-hybridized carbon atoms in amorphous carbon (C-C). And the peaks at 285.8 eV, 287.3 eV, and 288.7 eV correspond to C-O, C=O, -COO functionalities, respectively. Fig. 5.3.5.2 and Table 5.3.5 demonstrates the detailed composition of the five components forming the XPS C 1s spectra. The plasma-treated CNT pillar exhibits significant decrease in C=C and increase in other four compositions as compared to as-grown CNT pillar. Pure Ar condition showed the least O_2 containing chemical species of 25% compared to any other Ar / O_2 plasma system as the physical etching is dominant over chemical reaction. Increasing the O_2 concentration greater than 20% results in decrease in C=C chemical species due to chemical instability from lack of rotation around C=C bonds and nonsaturation of C=C bonds[160]. This also supports that increased O_2 plasma contributes to chemical reaction around the surface of CNT pillars. Plasma with O_2 80% condition showed the most oxygen containing chemical species where the crust layer was not sufficiently removed. This implies that excessive

concentration of 80% O_2 can hinder the actual etching of the crust layer and only chemically react with the very surface of the crust on the CNT forests. Therefore, an appropriate mixture of Ar and O_2 can be more effective for crust layer removal rather using pure Ar or pure O_2 plasma.

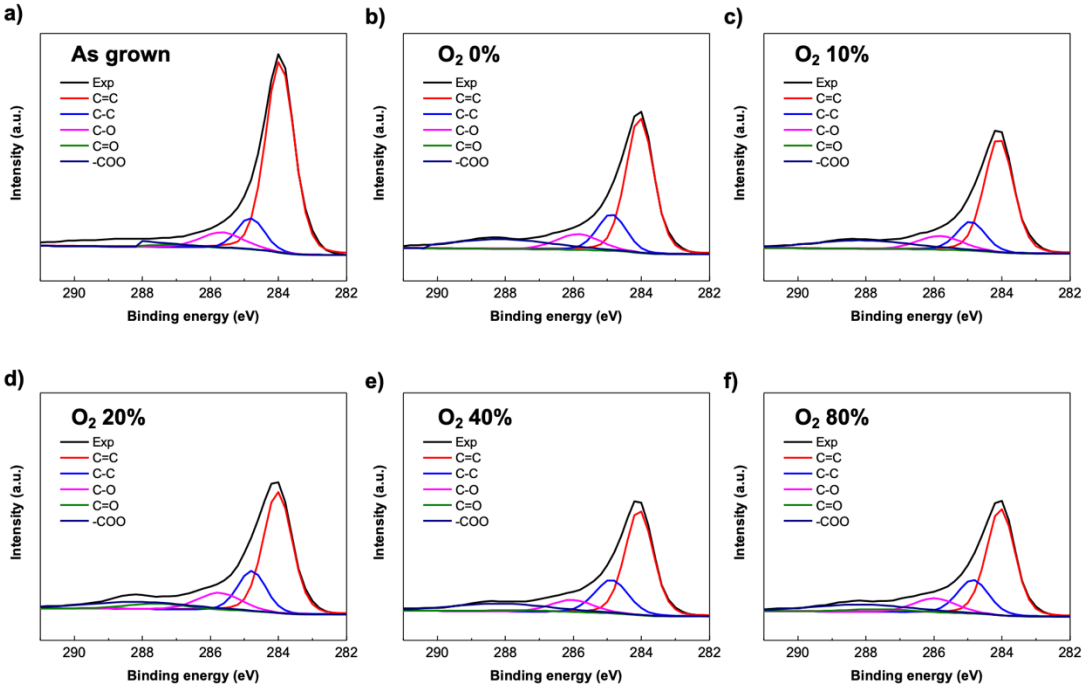

Figure 5.3.5 XPS C 1s peak deconvolution spectra of CNT forest top surface (a) as grown, after plasma treatment using different oxygen composition ratio of (b) 0 %, (c) 10 %, (d) 20 %, (e) 40 % and (f) 80 %. (CNT forest was grown by Decoupled recipe, total flow rate was fixed at 10 sccm)

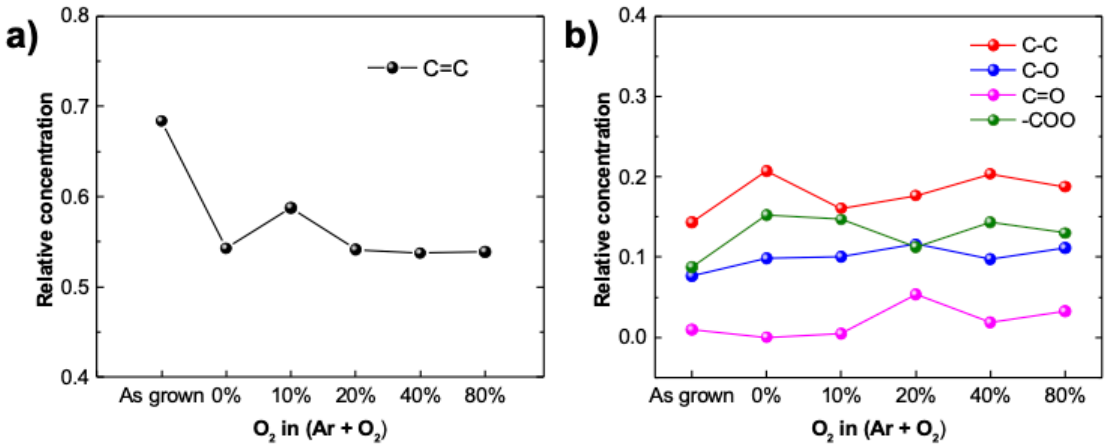

Figure 5.3.5.2 Relative concentration of chemical species after Ar / O_2 plasma under different oxygen composition ratio. (a) C=C, (b) C-C, C-O, C=O, -COO (CNT forests grown by Decoupled recipe)

Table 5.3.5 XPS C 1s peak deconvolution result of as grown CNT, Ar / O_2 plasma treated under different oxygen composition ratio. (CNT forests grown by Decoupled recipe)

Sample group	Concentration of chemical species (%)				
	C=C 284.0 eV	C-C 284.8 eV	C-O 285.8 eV	C=O 287.3 eV	-COO 288.7 eV
As grown	68.4	14.3	7.7	0.93	8.8
O_2 0 % plasma treated	54.3	20.7	9.8	0	15.2
O_2 10 % plasma treated	58.8	16.1	10.0	0.43	14.7
O_2 20 % plasma treated	54.1	17.7	11.6	5.3	11.3
O_2 40 % plasma treated	53.7	20.4	9.8	1.8	14.3
O_2 80 % plasma treated	53.9	18.8	11.1	3.2	13.0

5.3.6 Morphology changes of CNT forest pillars produced by different CVD recipes, after equivalent plasma etch exposure

Importantly, the as-grown morphology of the CNT forest can influence the etching results. As such, we now compare the etching of CNT pillars produced by different synthesis recipes (see experimental section), which we denote as the Reference, Decoupled, and Carbon-assisted recipes. Note that although the growth times were identical, CNT pillars grown by the Reference recipe reach ~100 μm in height (Fig. 5.3.6e), whereas the Decoupled and Carbon-assisted CNT pillars are ~20 μm high (Figs. 5.3.1c and 5.3.6g). Raman spectroscopy of Reference CNTs shows the lowest I_D / I_G ratio ~ 0.4 compared to Decoupled CNTs (0.73) or Carbon-assisted CNTs (0.75). This data is shown in Fig. 5.3.6.2, and implies the Reference CNT recipe gives the lease defective top surface of the forest. The Reference recipe is also the only one with radial breathing mode peaks observed, indicating some presence of single-walled CNTs in the forest. The defect quality is also confirmed by XPS, showing that Reference CNTs have the highest C 1s intensity and lowest O 1s intensity among the three recipes (Fig. 5.3.6.3). In terms of the CNT alignment, Carbon-assisted CNTs exhibit the highest degree of alignment (Fig. 5.3.6.4). In terms of top crust density, Reference CNTs show the least (Fig. 5.3.6.5), comprising less entangled CNTs on the top (Fig. 5.3.6a, 5.3.6i and 5.3.6m). We note that the degree of alignment of the sidewall correlates with the CNT crust density observed in SEM.

Now, we compare the plasma etching sensitivity of each CNT forest, under identical etch conditions (80 W, 5 min, Ar / O_2 = 8 / 2 sccm). Despite their higher relative quality, CNT forests with lower packing density and a less dense crust (Reference CNTs) are more vulnerable to the plasma; etching results in deep penetration and aggregation under the above condition (Fig. 5.3.6b, 5.3.6j, and 5.3.6n). In contrast, for the denser CNTs (Decoupled and Carbon-assisted recipes), the plasma removes the crust while preserving the CNT alignment (Fig. S8 and Fig. 5.3.6d, 5.3.6l, and 5.3.6p). Additional

results showing the conditions that result in modest etching are shown in Fig. 5.3.6.6 Fig. Fig. 5.3.6.7 and Fig. Fig. 5.3.6.8.

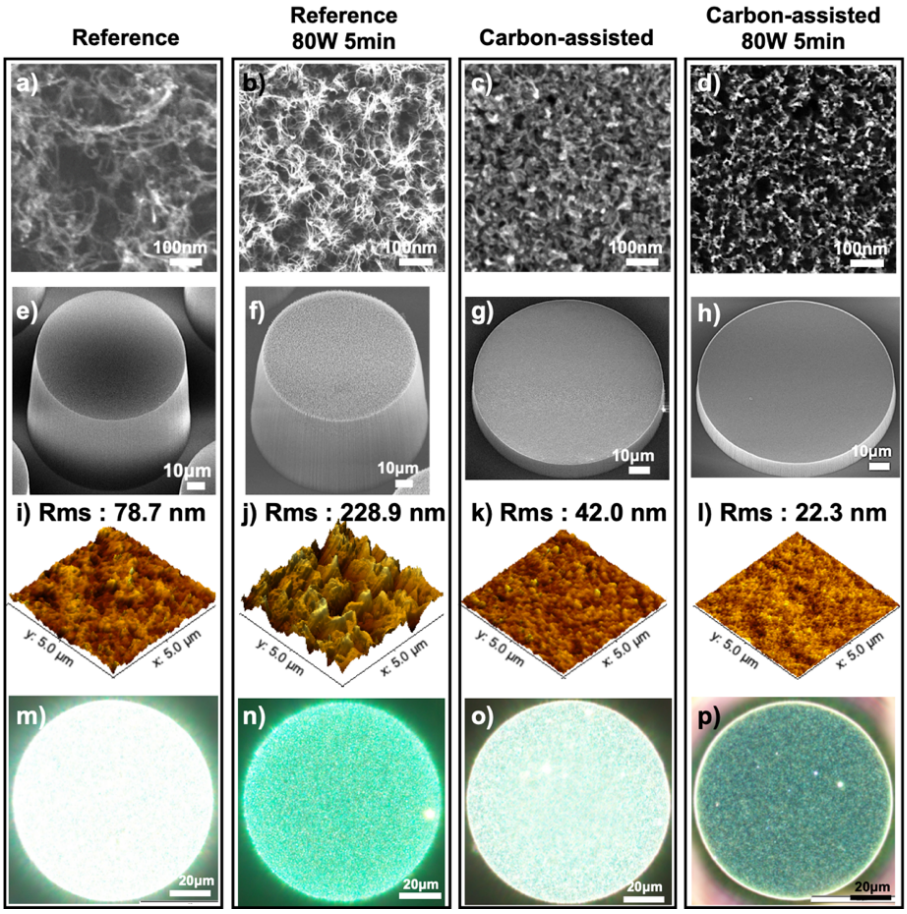

Figure 5.3.6 Morphology changes of CNT forest pillars produced by different CVD recipes, after equivalent plasma etch exposure. SEM images of top surface of (a) as-grown (Reference), (b) 80W 5 min plasma treated (Reference), (c) as-grown (Carbon-assisted), and (d) 80W 5 min plasma treated (Carbon-assisted) CNT pillars. Tilted SEM images of (e) as-grown (Reference), (f) 80W 5 min plasma treated (Reference), (g) as-grown (Carbon-assisted), and (h) 80W 5 min plasma treated (Carbon-assisted) CNT pillars.

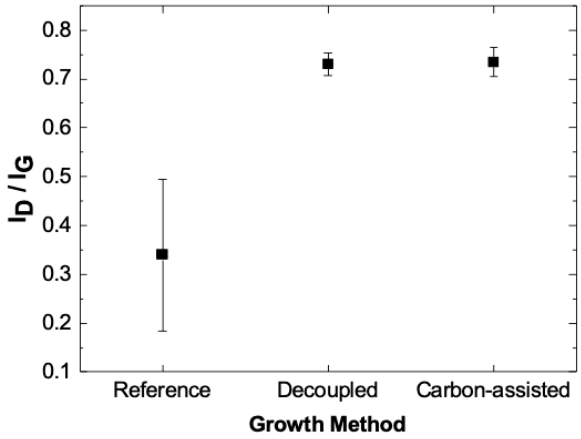

Figure 5.3.6.2 Raman DG ratio of CNT forests grown by different recipe. (n=5)

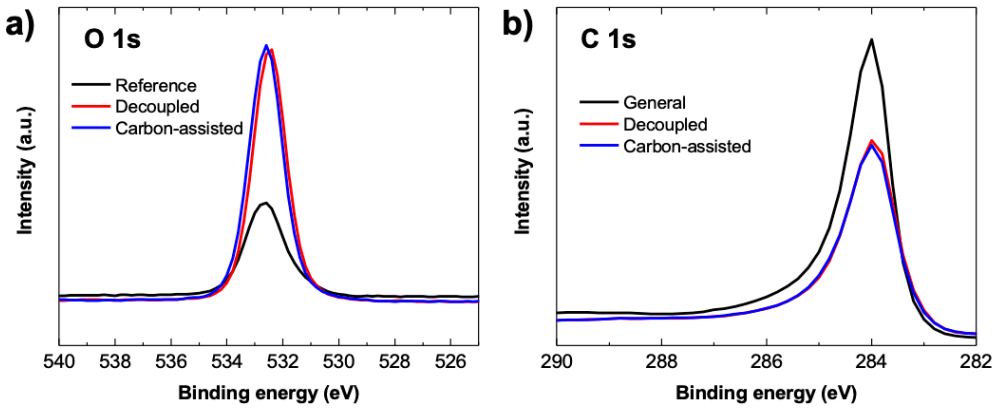

Figure 5.3.6.3 XPS spectra of (a) C 1s and (b) O 1s peaks from CNT forests grown by Reference, Decoupled, Carbon-assisted recipe.

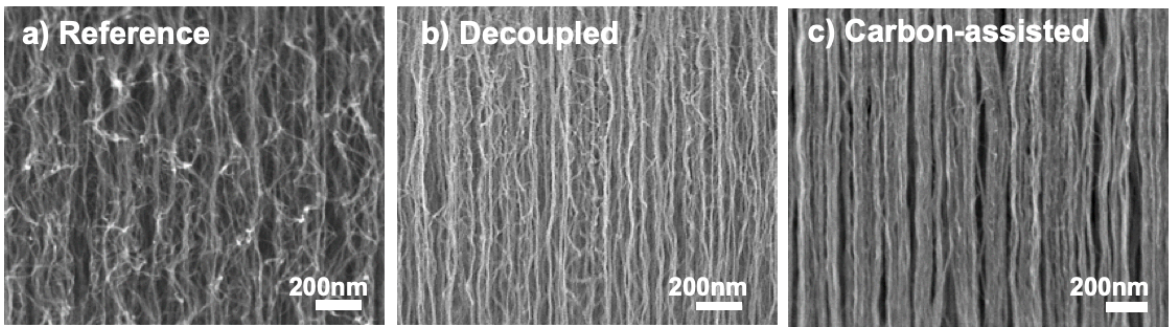

Figure 5.3.6.4 SEM images of CNT forest side walls grown by (a) Reference, (b) Decoupled, (c) Carbon-assisted recipe.

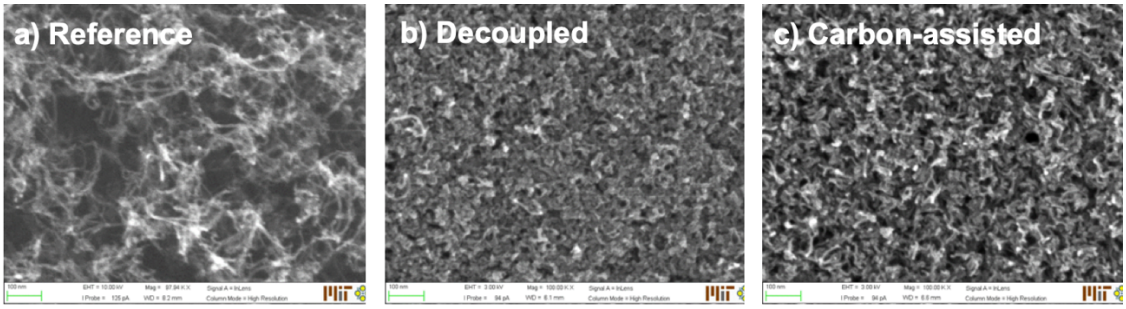

Figure 5.3.6.5 SEM images of surface crust layer of CNT forests grown by (a) Reference, (b) Decoupled, (c) Carbon-assisted recipe.

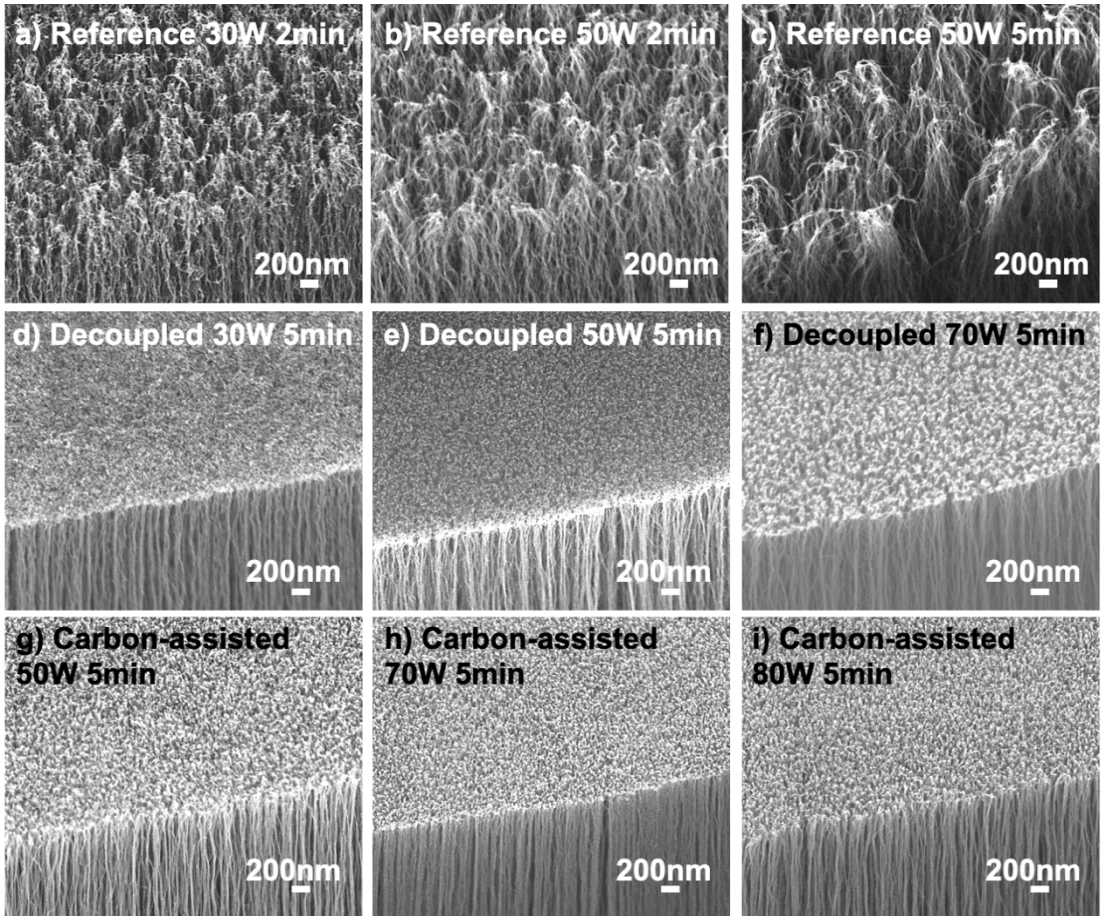

Figure 5.3.6.6 SEM images (tilted view) of Ar / O_2 plasma treated CNT pillars grown by Reference, Decoupled and Carbon-assisted recipes under different plasma power and time: Reference (a) 30 W 2 min, (b) 50 W 2 min, (c) 50 W 5 min. Decoupled (d) 30 W 5 min, (e) 50 W 5 min, (f) 70 W 5 min. Carbon-assisted (g) 50 W 5 min, (h) 70 W 5 min, (i) 80 W 5min. (Flow rate was Ar: 8 sccm, O_2: 2 sccm.)

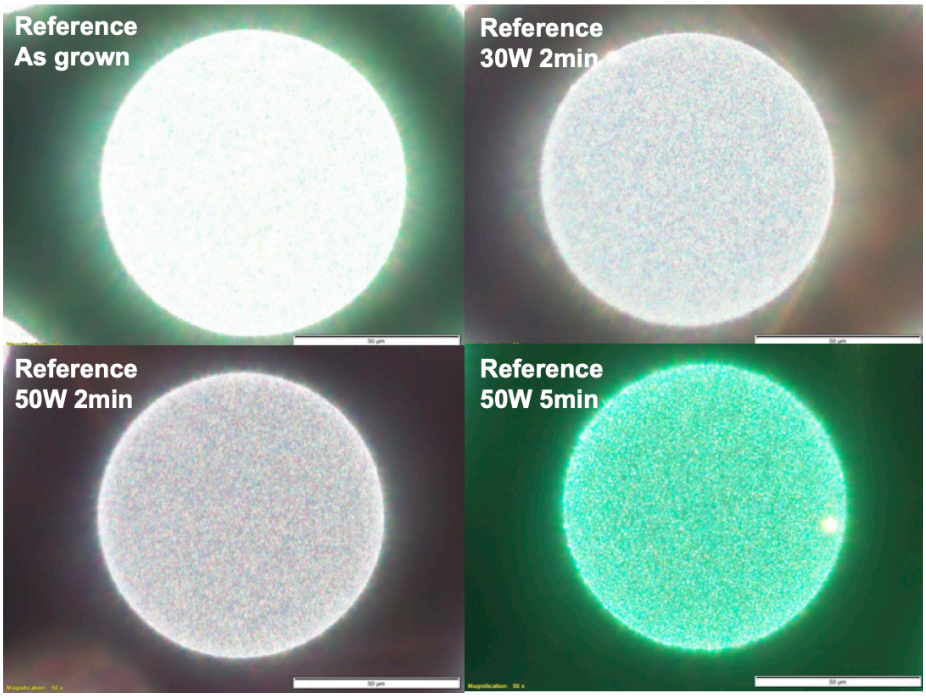

Figure 5.3.6.7 Optical microscopy images of top surface of CNT pillar grown by Reference recipe before and after Ar / O_2 plasma treatment under different time and power. (Exposure time for optical microscopy measurement was 1.25 s).

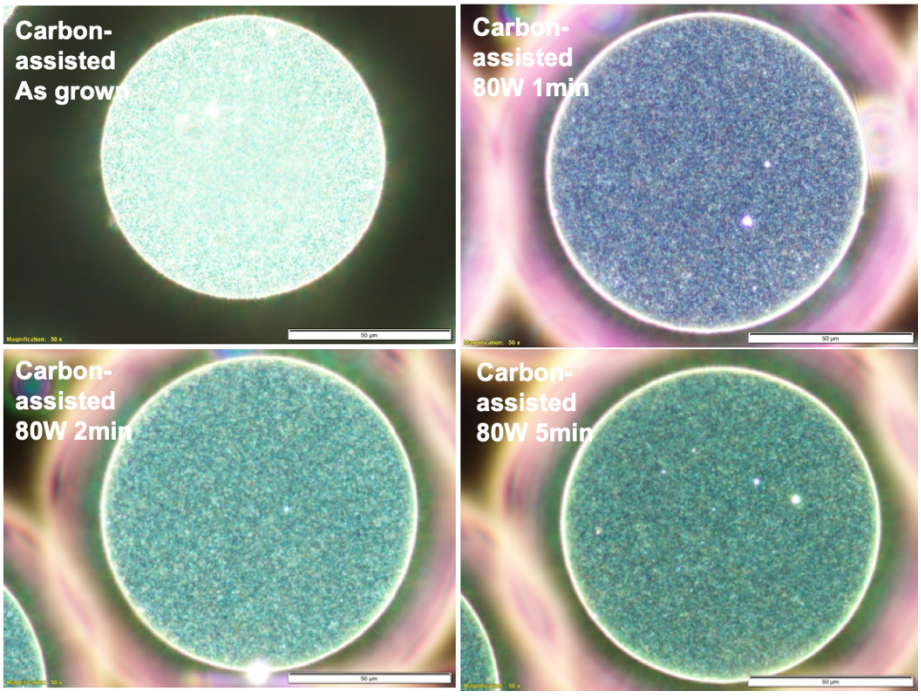

Figure 5.3.6.8 Optical microscopy images of top surface of CNT pillar grown by Carbon-assisted recipe before and after 80 W Ar / O_2 plasma treatment under different time. (Exposure time for optical microscopy measurement was 1.25 s)

5.3.7 Exposed tip density of the CNTs after plasma treatment

The exposed tip density of the CNTs after plasma treatment was analyzed from AFM images (Fig. 5.3.7) as an indication of the ability of the plasma etching to create isolated aligned tips (Fig. 5.3.8). With increasing plasma power, the exposed tip density of the CNTs decreases as they agglomerate with excessive plasma exposure, which is consistent with SEM images in Fig. 5.3.2g and 5.3.2h. Further, the tip density of Carbon-assisted CNTs was higher than that of Decoupled CNTs, owing to the higher CNT packing density. However, it should be noted that our AFM analysis can only be used for qualitative analysis between samples, thereby more accurate analysis with higher resolution images will be needed for quantitative analysis of the CNT tip density.

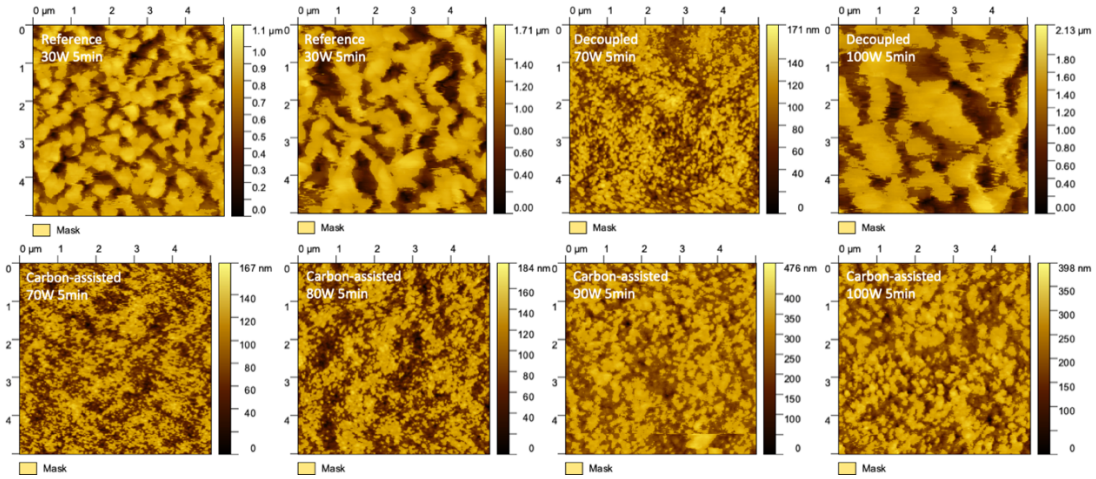

Figure 5.3.7 Masked AFM images of top surface of CNT pillars grown by different recipes (Reference, Decoupled, and Carbon-assisted) through Gwyddion software. Mask threshold was done by Otsu's algorithm.

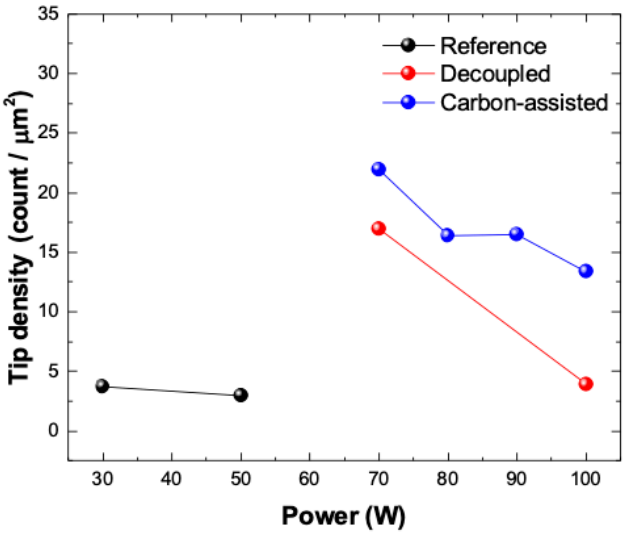

Figure 5.3.7.2 Tip density of CNT forests grown with different recipes versus plasma power (Plasma duration time was fixed at 5 min). Tip density was calculated from masked AFM images in Figure 5.3.7.1.

5.3.8 Lateral and vertical etching rates of CNT forests under Ar / O_2 plasma

Now, we quantitatively evaluate the etching rates by assessing the size reduction of CNT pillars due to the plasma, in both the vertical and lateral directions as defined in Fig. 5.3.8a and Fig. 5.3.8b. The power and time dependency in lateral and vertical directions, Fig. 5.3.8c, 5.3.8e and Fig. 5.3.8d, 5.3.8f, respectively. Reference CNTs revealed about 3 and 10-fold greater etching rates compared to Decoupled and Carbon-assisted CNTs, respectively. Also, in general the vertical etching rate is greater than the lateral etching rate. The vertical and lateral etching rates of Carbon-assisted CNTs are the lowest, at ~ 50 nm / min and ~100 nm / min respectively (80 W, measured over 5 min etch time). Interestingly, structural collapse did not occur for Carbon-assisted CNTs even with higher power of 100 W and longer plasma duration of 30 minutes, which implies that CNT forests with highly packed nature provide enough robustness

to maintain the forest structures but require greater power or duration to remove the top crust.

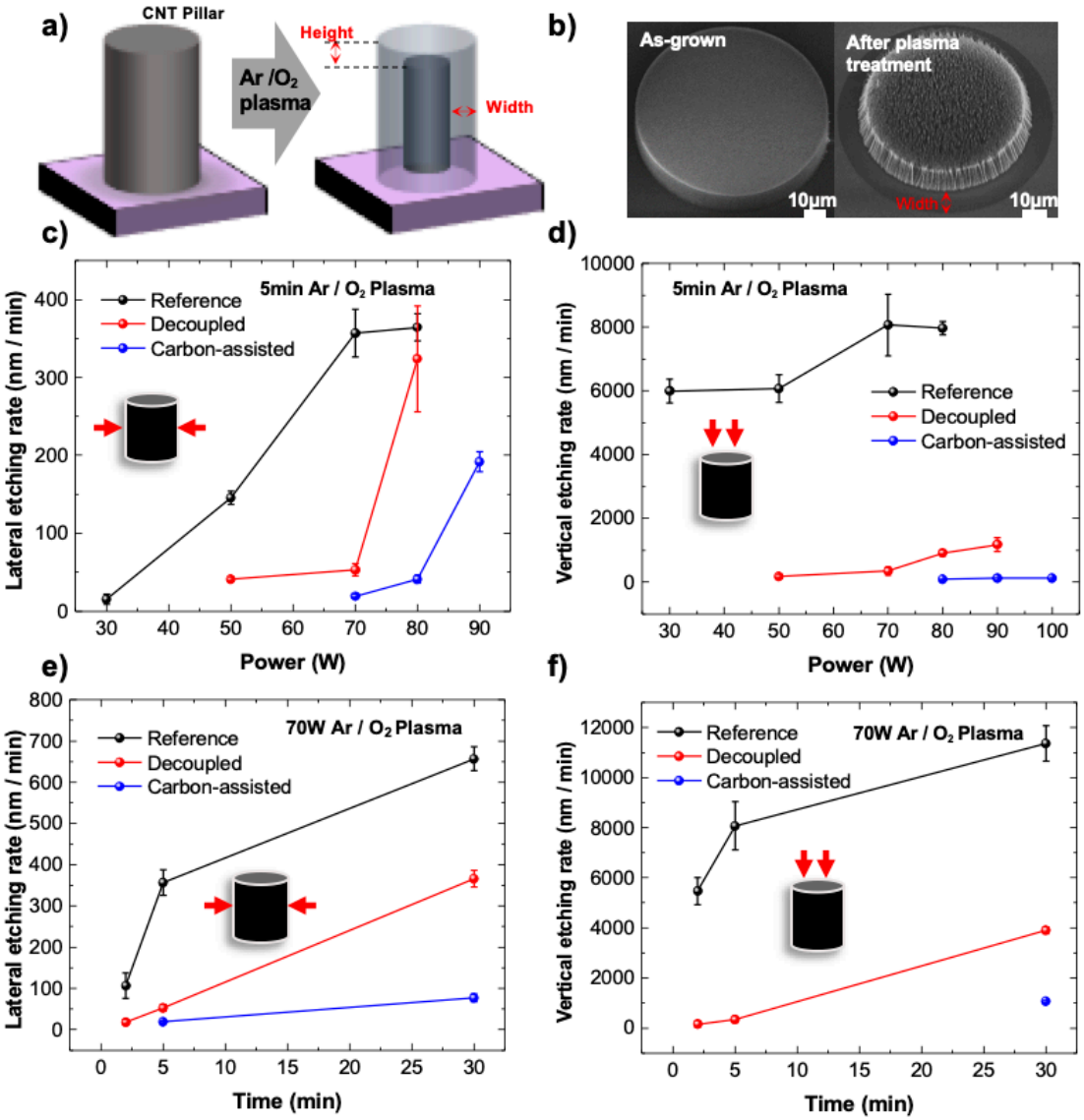

Figure 5.3.8 Lateral and vertical etching rates of CNT forests under Ar / O_2 plasma. (a) Schematics showing measurement definitions. (b) SEM images of an exemplary CNT pillar before and after plasma treatment. Lateral etch rate of CNT forests grown by Reference, Decoupled, and Carbon-assisted recipes versus etching (c) power and (d) time (n=5). Vertical etch rates versus etching (e) power and (f) time (n=5).

5.3.9 Lateral and vertical etching rates of CNT forests under Ar / O_2 plasma

In addition to physical etching, the Ar / O_2 plasma treatment provides spatial uniformity of chemical characteristics along the surface of the CNT forests. Raman mapping is used to perform spatial analysis of the CNT pillar surface. Fig. 5.3.9a shows the G-band intensity mapping of Raman spectra from the surface of an as-grown Decoupled CNT pillar; this has a spatial variation of G-band intensity ranging from 550 to 700, that can imply irregular distribution of carbonaceous impurities across the surface. After the Ar / O_2 plasma treatment (Ar : 2 sccm, O_2 : 8 sccm, 50W 5min), the surface shows uniform distribution of G-band intensity from 600 to 650.

Further, we quantitatively confirm that the Ar / O_2 plasma treatment does not deteriorate the alignment of CNTs during plasma treatment at modest etching condition. This is essential for subsequent application of CNT forests' microstructures since the different alignment degrees may provide different physical properties in one-dimensional materials [161]. Using the cross-sectional SEM images taken at the sidewall of different CNT forest samples (Reference, Decoupled, Carbon-assisted), we calculate the Herman orientation factor (HOF) and compare the degree of alignment before and after the plasma treatment [162]. SEM images of CNTs were taken at the middle sidewall of each CNT forest, Fig. 5.3.9c-e. The Carbon-assisted CNT pillar exhibits the highest HOF of 0.30 among the samples followed by 0.26 and 0.19 for Decoupled and Reference sample, respectively. After applying Ar / O_2 plasma treatment reflecting modest etching conditions for each sample, interestingly we find that the HOFs of all samples increased, to 0.31, 0.31 and 0.31 (Carbon-assisted, Decoupled, and Reference, respectively). The improvement in vertical alignment by 'modest' plasma etching can be explained by two reasons. First, as-grown CNTs with poor alignment are due to the mechanical constraint established by the crust layer, and they can relaxed

by release of residual stress one the crust is removed [163–165]. Second, aggregation of individual CNTs by the plasma enhances the vertical alignment.

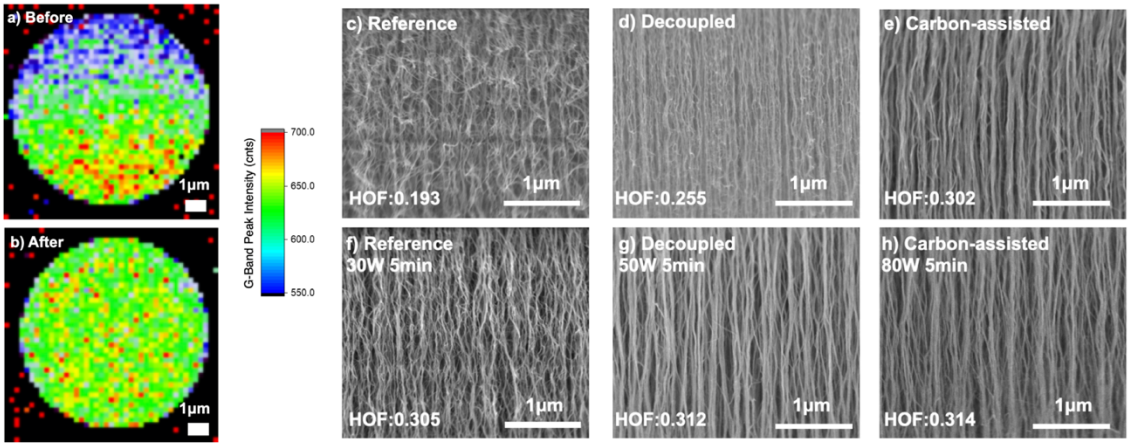

Figure 5.3.9 Spatial uniformity and vertical alignment of CNT forests before and after plasma treatment. Raman mapping images of top surface of CNT pillar (a) as-grown by Decoupled CVD recipe (b) after 50W 5min Ar / O_2 plasma treatment. SEM images of as-grown CNT pillar sidewalls (c) Reference (d) Decoupled (e) Carbon-assisted. SEM images of as-grown CNT pillars after Ar / O_2 plasma treatment (f) Reference 30W 5min (g) Decoupled 50W 5min (h) Carbon-assisted 80W 5min.

5.3.10 Surface modification 2D and 3D structured CNT forests via Ar / O_2 plasma

Based on the result above, we demonstrate the translation of our findings in this study to the surface modification of CNT microstructures that are useful in applications of CNT microstructures. For instance, a honeycomb structure CNT forest (Fig. 8a) can be a high-resolution stamp for flexographic printing of transparent electrode patterns [139], and slanted pillars of CNT forests (Fig. 8b) can be useful as anisotropic adhesives [166]. In both cases, delicate surface modification to reveal the CNT "tips" is useful to improve the performance of the CNTs. Using the appropriate process parameter control, plasma etching can be effective tool for crust removal of large-area, 2D or even 3D patterned CNT forests [167,168] with different surface morphologies.

Finally, in terms of surface roughness, we were not able to achieve less than 12.8 nm rms roughness with Ar / O_2 plasma treatment at 30W 5min Ar: 2 sccm O_2: 8 sccm condition. Considering the radius of individual CNTs used in this study ranges from 10 to 20 nm [123,169], such minimum surface roughness we can achieve might be limited by the curvature of the individual CNTs. This implies that smoother surfaces are achievable for vertically aligned SWCNTs having ~1 nm or smaller radius [170–172]. A smaller rms roughness also indicates greater coverage of CNTs at the top surface (fewer pores). Engineering both CNT growth and plasma treatment to leave a dense and smooth layer of CNTs at the top surface, could be ideal to minimize the thermal and electrical contact resistance accompanied by the intrinsically superb thermal and electrical properties of CNTs [173–176].

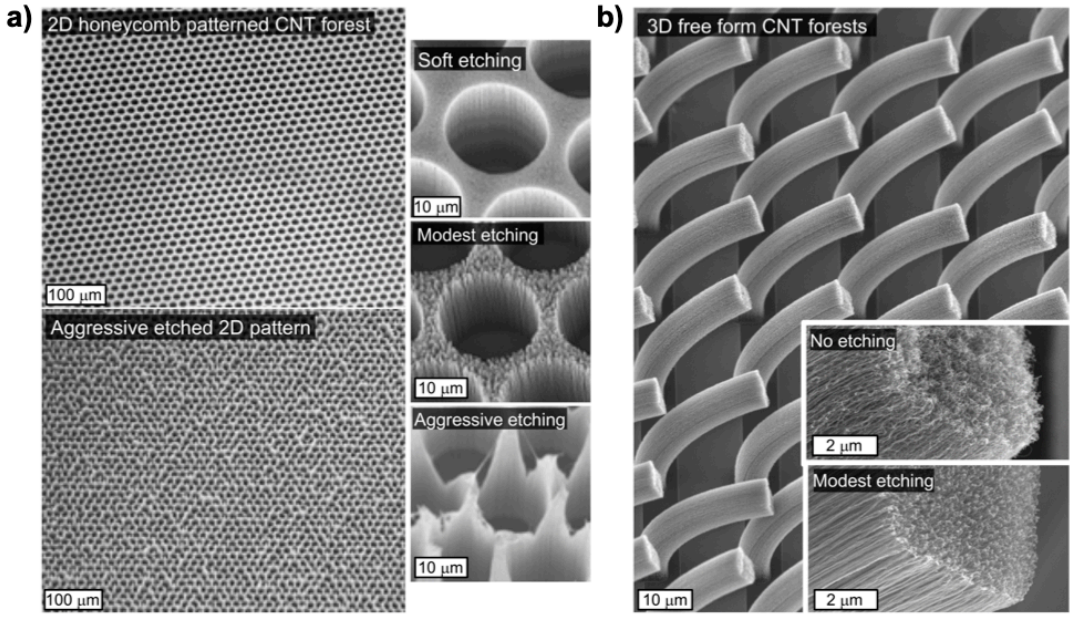

Figure 5.3.10 Surface modification 2D and 3D structured CNT forests via Ar / O_2 plasma. SEM images of (a) large-area honeycomb structures having 15 μm holes and (b) free-form CNT architectures, before and after plasma etching.

5.4 Conclusion

Herein we reported a parametric study of the surface modification of CNT forests using Ar / O_2 plasma etching, focusing on removal of the 'crust' layer without degrading the structural shape and alignment of the forest. Etching conditions are categorized according to the degree of modification of the surface, and we term 'modest' etching as achieving sufficient crust removal without structural collapse, when the power and exposure time are appropriately controlled. Flow rate and gas composition of Ar / O_2 gas mixture were also investigated as important parameters that affect the etching behavior. A low flow rate provides enough time for the active plasma sources to collide and react with the target surface, and ~20% of O_2 fraction provided an effective combination effect of both physical and chemical etching by Ar and O_2, respectively. Moreover, the etching behavior is sensitive to the initial status of CNT

forests, including the morphology, density, and defect ratio. We further investigated the plasma etching of CNT grown by three different CVD methods and compared the etch rates in both vertical and lateral directions. The findings of this study can be applied to tailor CNT forest surfaces for applications such as thermal interfaces, electrical contacts, and dynamic adhesives.

Bibliography

[1] S. Ijima, "Helical microtubules of graphitic carbon," *Nature* **354**, 56 (1991).

[2] R. H. B. and De Volder,Michael F. L. Sameh H. Tawfick and A. J. Hart, "Carbon Nanotubes : Present and Future Commercial Applications," *Science* **339**, 535 (2013).

[3] N. Ahn, I. Jeon, J. Yoon, E. I. Kauppinen, Y. Matsuo, S. Maruyama, and M. Choi, "Carbon-sandwiched perovskite solar cell," *J. Mater. Chem. A* **6**, 1382 (2018).

[4] K. Cui, Y. Qian, I. Jeon, A. Anisimov, Y. Matsuo, E. I. Kauppinen, and S. Maruyama, "Scalable and Solid-State Redox Functionalization of Transparent Single-Walled Carbon Nanotube Films for Highly Efficient and Stable Solar Cells," *Adv. Energy Mater.* **7**, 1 (2017).

[5] J. Chen, L. Wan, H. Li, J. Yan, J. Ma, B. Sun, F. Li, and B. S. Flavel, "A Polymer/Carbon-Nanotube Ink as a Boron-Dopant/Inorganic-Passivation Free Carrier Selective Contact for Silicon Solar Cells with over 21% Efficiency," *Adv. Funct. Mater.* **2004476**, 1 (2020).

[6] J. Chen, D. D. Tune, K. Ge, H. Li, and B. S. Flavel, "Front and Back-Junction Carbon Nanotube-Silicon Solar Cells with an Industrial Architecture," *Adv. Funct. Mater.* (2020).

[7] Y. Liu, S. Wang, and L. M. Peng, "Toward High-Performance Carbon Nanotube Photovoltaic Devices," *Adv. Energy Mater.* **6**, 1 (2016).

[8] P. Avouris, M. Freitag, and V. Perebeinos, "Carbon-nanotube photonics and optoelectronics," *Nat. Photonics* **2**, 341 (2008).

[9] A. Kaskela, A. G. Nasibulin, M. Y. Timmermans, B. Aitchison, A. Papadimitratos, Y. Tian, Z. Zhu, H. Jiang, D. P. Brown, A. Zakhidov, and E. I. Kauppinen, "Aerosol-synthesized SWCNT networks with tunable conductivity and transparency by a dry transfer technique," *Nano Lett.* **10**, 4349 (2010).

[10] S. M. Bachilo, M. S. Strano, C. Kittrell, R. H. Hauge, R. E. Smalley, and R. B. Weisman, "Structure-assigned optical spectra of single-walled carbon nanotubes," *Science* **298**, 2361 (2002).

[11] F. Wang, G. Dukovic, L. E. Brus, and T. F. Heinz, "The optical resonances in carbon nanotubes arise from excitons," *Science* **308**, 838 (2005).

[12] S. Ghosh, S. M. Bachilo, and R. B. Weisman, "Advanced sorting of single-walled carbon nanotubes by nonlinear density-gradient ultracentrifugation," *Nat. Nanotechnol.* **5**, 443 (2010).

[13] H. Liu, D. Nishide, T. Tanaka, and H. Kataura, "Large-scale single-chirality separation of single-wall carbon nanotubes by simple gel chromatography," *Nat. Commun.* **2** (2011).

[14] J. A. Fagan, E. H. Hároz, R. Ihly, H. Gui, J. L. Blackburn, J. R. Simpson, S. Lam, A. R. Hight Walker, S. K. Doorn, and M. Zheng, "Isolation of >1 nm diameter

single-wall carbon nanotube species using aqueous two-phase extraction," *ACS Nano* **9**, 5377 (2015).

[15] A. Nish, J. Y. Hwang, J. Doig, and R. J. Nicholas, "Highly selective dispersion of single-walled carbon nanotubes using aromatic polymers," *Nat. Nanotechnol.* **2**, 640 (2007).

[16] J. L. Blackburn, "Semiconducting Single-Walled Carbon Nanotubes in Solar Energy Harvesting," *ACS Energy Lett.* **2**, 1598 (2017).

[17] T. Schmid and P. Dariz, "Raman Microspectroscopic Imaging of Binder Remnants in Historical Mortars Reveals Processing Conditions," *Heritage* **2**, 1662 (2019).

[18] A. G. Ryabenko, T. V. Dorofeeva, and G. I. Zvereva, "UV-VIS-NIR spectroscopy study of sensitivity of single-wall carbon nanotubes to chemical processing and Van-der-Waals SWNT/SWNT interaction. Verification of the SWNT content measurements by absorption spectroscopy," *Carbon* **42**, 1523 (2004).

[19] K. H. Eckstein, F. Oberndorfer, M. M. Achsnich, F. Schöppler, and T. Hertel, "Quantifying Doping Levels in Carbon Nanotubes by Optical Spectroscopy," *J. Phys. Chem. C* **123**, 30001 (2019).

[20] J. A. Phys and J. L. Blackburn, "Carbon nanotubes in high-performance perovskite photovoltaics and other emerging optoelectronic applications," *J. Appl. Phys.* **010903** (2021).

[21] M. S. Arnold, J. D. Zimmerman, C. K. Renshaw, X. Xu, R. R. Lunt, C. M. Austin, and S. R. Forrest, "Broad spectral response using carbon nanotube/organic semiconductor/C 60 photodetectors," *Nano Lett.* **9**, 3354 (2009).

[22] S. Berson, R. De Bettignies, S. Bailly, S. Guillerez, and B. Jousselme, "Elaboration of P3HT/CNT/PCBM composites for organic photovoltaic cells," *Adv. Funct. Mater.* **17**, 3363 (2007).

[23] B. Pradhan, S. K. Batabyal, and A. J. Pal, "Functionalized carbon nanotubes in donor/acceptor-type photovoltaic devices," *Appl. Phys. Lett.* **88**, 2 (2006).

[24] G. D. M. R. Dabera, K. D. G. I. Jayawardena, M. R. R. Prabhath, I. Yahya, Y. Y. Tan, N. A. Nismy, H. Shiozawa, M. Sauer, G. Ruiz-Soria, P. Ayala, V. Stolojan, A. A. D. T. Adikaari, P. D. Jarowski, T. Pichler, and S. R. P. Silva, "Hybrid carbon nanotube networks as efficient hole extraction layers for organic photovoltaics," *ACS Nano* **7**, 556 (2013).

[25] S. N. Habisreutinger, B. Wenger, H. J. Snaith, and R. J. Nicholas, "Dopant-Free Planar n–i–p Perovskite Solar Cells with Steady-State Efficiencies Exceeding 18%," *ACS Energy Lett.* **2**, 622 (2017).

[26] P. Schulz, A.-M. Dowgiallo, M. Yang, K. Zhu, J. L. Blackburn, and J. J. Berry, "Charge Transfer Dynamics between Carbon Nanotubes and Hybrid Organic Metal Halide Perovskite Films," *J. Phys. Chem. Lett.* **7**, 418 (2016).

[27] S. Seo, I. Jeon, R. Xiang, C. Lee, H. Zhang, T. Tanaka, jin-wook lee, D. Suh, T. Ogamoto, R. Nishikubo, A. Saeki, S. Chiashi, J. Shiomi, H. Kataura, H. M. Lee, Y. Yang, Y. Matsuo, and S. Maruyama, "Semiconducting Carbon

Nanotubes as Crystal Growth Templates and Grain Bridges in Perovskite Solar Cells," *J. Mater. Chem. A* (2019).

[28] I. Jeon, C. Delacou, A. Kaskela, E. I. Kauppinen, S. Maruyama, and Y. Matsuo, "Metal-electrode-free Window-like Organic Solar Cells with p-Doped Carbon Nanotube Thin-film Electrodes," *Sci. Rep.* **6**, 1 (2016).

[29] I. Jeon, K. Cui, T. Chiba, A. Anisimov, A. G. Nasibulin, E. I. Kauppinen, S. Maruyama, and Y. Matsuo, "Direct and Dry Deposited Single-Walled Carbon Nanotube Films Doped with MoOx as Electron-Blocking Transparent Electrodes for Flexible Organic Solar Cells," *J. Am. Chem. Soc.* **137**, 7982 (2015).

[30] I. Jeon, T. Chiba, C. Delacou, Y. Guo, A. Kaskela, O. Reynaud, E. I. Kauppinen, S. Maruyama, and Y. Matsuo, "Single-Walled Carbon Nanotube Film as Electrode in Indium-Free Planar Heterojunction Perovskite Solar Cells: Investigation of Electron-Blocking Layers and Dopants," *Nano Lett.* **15**, 6665 (2015).

[31] I. Jeon, J. Yoon, U. Kim, C. Lee, R. Xiang, A. Shawky, J. Xi, J. Byeon, H. M. Lee, M. Choi, S. Maruyama, and Y. Matsuo, "High-Performance Solution-Processed Double-Walled Carbon Nanotube Transparent Electrode for Perovskite Solar Cells," *Adv. Energy Mater.* **9**, 1 (2019).

[32] I. Jeon, S. Seo, Y. Sato, C. Delacou, A. Anisimov, K. Suenaga, E. I. Kauppinen, S. Maruyama, and Y. Matsuo, "Perovskite Solar Cells Using Carbon Nanotubes Both as Cathode and as Anode," *J. Phys. Chem. C*, acs. jpcc.7b10334 (2017).

[33] C. Lee, S. W. Lee, S. Bae, A. Shawky, V. Devaraj, A. Anisimov, E. I. Kauppinen, J. W. Oh, Y. Kang, D. Kim, I. Jeon, S. Maruyama, and H. S. Lee, "Carbon Nanotube Electrode-Based Perovskite–Silicon Tandem Solar Cells," *Sol. RRL* **2000353**, 1 (2020).

[34] I. Jeon, A. Shawky, S. Seo, Y. Qian, A. Anisimov, E. I. Kauppinen, Y. Matsuo, and S. Maruyama, "Carbon nanotubes to outperform metal electrodes in perovskite solar cellsviadopant engineering and hole-selectivity enhancement," *J. Mater. Chem. A* **8**, 11141 (2020).

[35] J.-W. Lee, I. Jeon, H.-S. Lin, S. Seo, T.-H. Han, A. Anisimov, E. I. Kauppinen, Y. Matsuo, S. Maruyama, and Y. Yang, "Vapor-Assisted Ex-Situ Doping of Carbon Nanotube toward Efficient and Stable Perovskite Solar Cells," *Nano Lett.*, acs. nanolett.8b04190 (2018).

[36] H. S. Lin, S. Okawa, Y. Ma, S. Yotsumoto, C. Lee, S. Tan, S. Manzhos, M. Yoshizawa, S. Chiashi, H. M. Lee, T. Tanaka, H. Kataura, I. Jeon, I. Jeon, Y. Matsuo, Y. Matsuo, S. Maruyama, and S. Maruyama, "Polyaromatic Nanotweezers on Semiconducting Carbon Nanotubes for the Growth and Interfacing of Lead Halide Perovskite Crystal Grains in Solar Cells," *Chem. Mater.* **32**, 5125 (2020).

[37] S. N. Habisreutinger, T. Leijtens, G. E. Eperon, S. D. Stranks, R. J. Nicholas, and H. J. Snaith, "Carbon nanotube/polymer composites as a highly stable hole collection layer in perovskite solar cells," *Nano Lett.* **14**, 5561 (2014).

[38] H. Wu, X. Zhao, Y. Sun, L. Yang, M. Zou, H. Zhang, Y. Wu, L. Dai, Y. Shang, and A. Cao, "Improving Carbon Nanotube-Silicon Solar Cells by Solution Processable Metal Chlorides," *Sol. RRL* **3**, 1900147 (2019).

[39] Y. Qian, I. Jeon, Y. L. Ho, C. Lee, S. Jeong, C. Delacou, S. Seo, A. Anisimov, E. I. Kaupinnen, Y. Matsuo, Y. Kang, H. S. Lee, D. Kim, J. J. Delaunay, and S. Maruyama, "Multifunctional Effect of p-Doping, Antireflection, and Encapsulation by Polymeric Acid for High Efficiency and Stable Carbon Nanotube-Based Silicon Solar Cells," *Adv. Energy Mater.* **10**, 1 (2020).

[40] D. D. Tune, N. Mallik, H. Fornasier, and B. S. Flavel, "Breakthrough Carbon Nanotube–Silicon Heterojunction Solar Cells," *Adv. Energy Mater.* **10**, 1 (2020).

[41] S. Esconjauregui, L. D'Arsié, Y. Guo, J. Yang, H. Sugime, S. Caneva, C. Cepek, and J. Robertson, "Efficient Transfer Doping of Carbon Nanotube Forests by MoO3," *ACS Nano* **9**, 10422 (2015).

[42] S. L. Hellstrom, M. Vosgueritchian, R. M. Stoltenberg, I. Irfan, M. Hammock, Y. B. Wang, C. Jia, X. Guo, Y. Gao, and Z. Bao, "Strong and stable doping of carbon nanotubes and graphene by MoO x for transparent electrodes," *Nano Lett.* **12**, 3574 (2012).

[43] R. Ihly, A. M. Dowgiallo, M. Yang, P. Schulz, N. J. Stanton, O. G. Reid, A. J. Ferguson, K. Zhu, J. J. Berry, and J. L. Blackburn, "Efficient charge extraction and slow recombination in organic-inorganic perovskites capped with semiconducting single-walled carbon nanotubes," *Energy Environ. Sci.* **9**, 1439 (2016).

[44] R. Xiang, T. Inoue, Y. Zheng, A. Kumamoto, Y. Qian, Y. Sato, M. Liu, D. Gokhale, J. Guo, et al., "One-dimensional van der Waals heterostructures," *Science,* **367**, 537 (2020).

[45] Y. Qian, S. Seo, I. Jeon, H. Lin, S. Okawa, Y. Zheng, A. Shawky, A. Anisimov, E. I. Kauppinen, J. Kong, R. Xiang, Y. Matsuo, and S. Maruyama, "MoS2-carbon nanotube heterostructure as efficient hole transporters and conductors in perovskite solar cells," *Appl. Phys. Express* **13** (2020).

[46] J. Chen, D. D. Tune, K. Ge, H. Li, and B. S. Flavel, "Front and Back-Junction Carbon Nanotube-Silicon Solar Cells with an Industrial Architecture," *Adv. Funct. Mater.* **30** (2020).

[47] A. Al-Ashouri, E. Köhnen, B. Li, A. Magomedov, H. Hempel, P. Caprioglio, J. A. Márquez, A. B. M. Vilches, E. Kasparavicius, et al., "Monolithic perovskite/silicon tandem solar cell with >29% efficiency by enhanced hole extraction," *Science,* **370**, 1300 (2020).

[48] G. M. Albuquerque, "Theoretical limit for efficiency of silicon solar cells 'The Shockley- Queisser Limit and Beyond'" (2019).

[49] G. Kim, H. Min, K. S. Lee, D. Y. Lee, S. M. Yoon, and S. Il Seok, "Impact of strain relaxation on performance of a-formamidinium lead iodide perovskite solar cells," *Science,* **370**, 108 (2020).

[50] K. Yoshikawa, H. Kawasaki, W. Yoshida, T. Irie, K. Konishi, K. Nakano, T. Uto, D. Adachi, M. Kanematsu, H. Uzu, and K. Yamamoto, "Silicon heterojunction

solar cell with interdigitated back contacts for a photoconversion efficiency over 26%," *Nat. Energy* **2** (2017).

[51] A. Kojima, K. Teshima, Y. Shirai, and T. Miyasaka, "Organometal halide perovskites as visible-light sensitizers for photovoltaic cells," *J. Am. Chem. Soc.* **131**, 6050 (2009).

[52] Q. Luo, R. Wu, L. Ma, C. Wang, H. Liu, H. Lin, N. Wang, Y. Chen, and Z. Guo, "Recent Advances on Carbon Nanotube Utilizations in Perovskite Solar Cells," *Adv. Funct. Mater.* **2004765**, 1 (2020).

[53] H. Tang, Q. Cao, Z. He, S. Wang, J. Han, T. Li, B. Gao, J. Yang, D. Deng, and X. Li, "SnO2–Carbon Nanotubes Hybrid Electron Transport Layer for Efficient and Hysteresis-Free Planar Perovskite Solar Cells," *Sol. RRL* **4**, 1 (2020).

[54] S. N. Habisreutinger, T. Leijtens, G. E. Eperon, S. D. Stranks, R. J. Nicholas, and H. J. Snaith, "Enhanced hole extraction in perovskite solar cells through carbon nanotubes," *J. Phys. Chem. Lett.* **5**, 4207 (2014).

[55] R. Ihly, A.-M. Dowgiallo, M. Yang, P. Schulz, N. J. Stanton, O. G. Reid, A. J. Ferguson, K. Zhu, J. J. Berry, and J. L. Blackburn, "Efficient charge extraction and slow recombination in organic–inorganic perovskites capped with semiconducting single-walled carbon nanotubes," *Energy Environ. Sci.* **9**, 1439 (2016).

[56] K. Aitola, K. Domanski, J. P. Correa-Baena, K. Sveinbjörnsson, M. Saliba, A. Abate, M. Grätzel, E. Kauppinen, E. M. J. Johansson, W. Tress, A. Hagfeldt, and G. Boschloo, "High Temperature-Stable Perovskite Solar Cell Based on Low-Cost Carbon Nanotube Hole Contact," *Adv. Mater.* **29** (2017).

[57] L. Rakocevic, F. Ernst, N. T. Yimga, S. Vashishtha, T. Aernouts, T. Heumueller, C. J. Brabec, R. Gehlhaar, and J. Poortmans, "Reliable Performance Comparison of Perovskite Solar Cells Using Optimized Maximum Power Point Tracking," *Sol. RRL* **3**, 1 (2019).

[58] D. W. DeQuilettes, S. M. Vorpahl, S. D. Stranks, H. Nagaoka, G. E. Eperon, M. E. Ziffer, H. J. Snaith, and D. S. Ginger, "Impact of microstructure on local carrier lifetime in perovskite solar cells," *Science,* **348**, 683 (2015).

[59] Y. Kutes, Y. Zhou, J. L. Bosse, J. Steffes, N. P. Padture, and B. D. Huey, "Mapping the Photoresponse of CH3NH3PbI3 Hybrid Perovskite Thin Films at the Nanoscale," *Nano Lett.* **16**, 3434 (2016).

[60] Y. Tidhar, E. Edri, H. Weissman, D. Zohar, G. Hodes, D. Cahen, B. Rybtchinski, and S. Kirmayer, "Crystallization of methyl ammonium lead halide perovskites: Implications for photovoltaic applications," *J. Am. Chem. Soc.* **136**, 13249 (2014).

[61] M. Wang, H. Wang, W. Li, X. Hu, K. Sun, and Z. Zang, "Defect passivation using ultrathin PTAA layers for efficient and stable perovskite solar cells with a high fill factor and eliminated hysteresis," *J. Mater. Chem. A* **7**, 26421 (2019).

[62] T. H. Han, J. W. Lee, C. Choi, S. Tan, C. Lee, Y. Zhao, Z. Dai, N. De Marco, S. J. Lee, S. H. Bae, Y. Yuan, H. M. Lee, Y. Huang, and Y. Yang, "Perovskite-

polymer composite cross-linker approach for highly-stable and efficient perovskite solar cells," *Nat. Commun.* **10**, 1 (2019).

[63] J. W. Lee, S. H. Bae, Y. T. Hsieh, N. De Marco, M. Wang, P. Sun, and Y. Yang, "A Bifunctional Lewis Base Additive for Microscopic Homogeneity in Perovskite Solar Cells," *Chem* **3**, 290 (2017).

[64] J. T. W. Wang, Z. Wang, S. Pathak, W. Zhang, D. W. Dequilettes, F. Wisnivesky-Rocca-Rivarola, J. Huang, P. K. Nayak, J. B. Patel, et al., "Efficient perovskite solar cells by metal ion doping," *Energy Environ. Sci.* **9**, 2892 (2016).

[65] M. Yang, Y. Zhou, Y. Zeng, C. S. Jiang, N. P. Padture, and K. Zhu, "Square-Centimeter Solution-Processed Planar CH3NH3PbI3 Perovskite Solar Cells with Efficiency Exceeding 15%," *Adv. Mater.* **27**, 6363 (2015).

[66] S. Chaudhary, H. Lu, A. M. Müller, C. J. Bardeen, and M. Ozkan, "Hierarchical placement and associated optoelectronic impact of carbon nanotubes in polymer-fullerene solar cells," *Nano Lett.* **7**, 1973 (2007).

[67] B. Aïssa, A. Ali, A. Bentouaf, W. Khan, Y. Zakaria, K. A. Mahmoud, K. Ali, N. Malik Muhammad, and S. A. Mansour, "Influence of single-walled carbon nanotubes induced exciton dissociation improvement on hybrid organic photovoltaic devices," *J. Appl. Phys.* **126** (2019).

[68] C. H. Chiang and C. G. Wu, "Bulk heterojunction perovskite-PCBM solar cells with high fill factor," *Nat. Photonics* **10**, 196 (2016).

[69] Y. Zhang, L. Tan, Q. Fu, L. Chen, T. Ji, X. Hu, and Y. Chen, "Enhancing the grain size of organic halide perovskites by sulfonate-carbon nanotube incorporation in high performance perovskite solar cells," *Chem. Commun.* **52**, 5674 (2016).

[70] T. Tanaka, Y. Urabe, D. Nishide, and H. Kataura, "Continuous separation of metallic and semiconducting carbon nanotubes using agarose gel," *Appl. Phys. Express* **2** (2009).

[71] T. Tanaka, Y. Urabe, D. Nishide, H. Liu, S. Asano, S. Nishiyama, and H. Kataura, "Metal/semiconductor separation of single-wall carbon nanotubes by selective adsorption and desorption for agarose gel," *Phys. Status Solidi Basic Res.* **247**, 2867 (2010).

[72] M. S. Fuhrer, J. Nygård, L. Shih, M. Forero, Y. G. Yoon, M. S. C. Mazzoni, H. J. Choi, J. Ihm, S. G. Louie, A. Zettl, and P. L. McEuen, "Crossed nanotube junctions," *Science,* **288**, 494 (2000).

[73] P. N. Nirmalraj, P. E. Lyons, S. De, J. N. Coleman, and J. J. Boland, "Electrical connectivity in single-walled carbon nanotube networks," *Nano Lett.* **9**, 3890 (2009).

[74] J. Huang, S. Tan, P. D. Lund, and H. Zhou, "Impact of H2O on organic-inorganic hybrid perovskite solar cells," *Energy Environ. Sci.* **10**, 2284 (2017).

[75] X. Gong, M. Li, X. B. Shi, H. Ma, Z. K. Wang, and L. S. Liao, "Controllable Perovskite Crystallization by Water Additive for High-Performance Solar Cells," *Adv. Funct. Mater.* **25**, 6671 (2015).

[76] D. Liu, C. J. Traverse, P. Chen, M. Elinski, C. Yang, L. Wang, M. Young, and R. R. Lunt, "Aqueous-Containing Precursor Solutions for Efficient Perovskite Solar Cells," *Adv. Sci.* **5** (2018).

[77] C. H. Chiang, M. K. Nazeeruddin, M. Grätzel, and C. G. Wu, "The synergistic effect of H2O and DMF towards stable and 20% efficiency inverted perovskite solar cells," *Energy Environ. Sci.* **10**, 808 (2017).

[78] B. Conings, A. Babayigit, T. Vangerven, J. D'Haen, J. Manca, and H. G. Boyen, "The impact of precursor water content on solution-processed organometal halide perovskite films and solar cells," *J. Mater. Chem. A* **3**, 19123 (2015).

[79] N. Ahn, D. Y. Son, I. H. Jang, S. M. Kang, M. Choi, and N. G. Park, "Highly Reproducible Perovskite Solar Cells with Average Efficiency of 18.3% and Best Efficiency of 19.7% Fabricated via Lewis Base Adduct of Lead(II) Iodide," *J. Am. Chem. Soc.* **137**, 8696 (2015).

[80] I. Ka, L. F. Gerlein, R. Nechache, and S. G. Cloutier, "High-performance nanotube-enhanced perovskite photodetectors," *Sci. Rep.* **7**, 1 (2017).

[81] F. Li, H. Wang, D. Kufer, L. Liang, W. Yu, E. Alarousu, C. Ma, Y. Li, Z. Liu, C. Liu, N. Wei, F. Wang, L. Chen, O. F. Mohammed, A. Fratalocchi, X. Liu, G. Konstantatos, and T. Wu, "Ultrahigh Carrier Mobility Achieved in Photoresponsive Hybrid Perovskite Films via Coupling with Single-Walled Carbon Nanotubes," *Adv. Mater.* **29** (2017).

[82] S. Sun, N. Liang, Y. Kawashima, D. Xia, and F. Cui, "Hydrophobic ion pairing of an insulin-sodium deoxycholate complex for oral delivery of insulin.," *Int. J. Nanomedicine* **6**, 3049 (2011).

[83] J. W. Lee, H. S. Kim, and N. G. Park, "Lewis Acid-Base Adduct Approach for High Efficiency Perovskite Solar Cells," *Acc. Chem. Res.* **49**, 311 (2016).

[84] Q. Wang, M. Lyu, M. Zhang, J. H. Yun, H. Chen, and L. Wang, "Transition from the Tetragonal to Cubic Phase of Organohalide Perovskite: The Role of Chlorine in Crystal Formation of CH3NH3PbI3 on TiO2 Substrates," *J. Phys. Chem. Lett.* **6**, 4379 (2015).

[85] J. Yin, D. Cortecchia, A. Krishna, S. Chen, N. Mathews, A. C. Grimsdale, and C. Soci, "Interfacial charge transfer anisotropy in polycrystalline lead iodide perovskite films," *J. Phys. Chem. Lett.* **6**, 1396 (2015).

[86] T. Zhang, N. Guo, G. Li, X. Qian, and Y. Zhao, "A controllable fabrication of grain boundary PbI2 nanoplates passivated lead halide perovskites for high performance solar cells," *Nano Energy* **26**, 50 (2016).

[87] W. Nie, H. Tsai, R. Asadpour, A. J. Neukirch, G. Gupta, J. J. Crochet, M. Chhowalla, S. Tretiak, M. A. Alam, and H. Wang, "High-efficiency solution-processed perovskite solar cells with millimeter-scale grains," 522 (2015).

[88] M. H. Park, S. H. Jeong, H. K. Seo, C. Wolf, Y. H. Kim, H. Kim, J. Byun, J. S. Kim, H. Cho, and T. W. Lee, "Unravelling additive-based nanocrystal pinning for high efficiency organic-inorganic halide perovskite light-emitting diodes," *Nano Energy* **42**, 157 (2017).

[89] Z. Chu, M. Yang, P. Schulz, D. Wu, X. Ma, E. Seifert, L. Sun, X. Li, K. Zhu, and K. Lai, "Impact of grain boundaries on efficiency and stability of organic-inorganic trihalide perovskites," *Nat. Commun.* **8**, 1 (2017).

[90] Q. Dong, Y. Fang, Y. Shao, P. Mulligan, J. Qiu, L. Cao, and J. Huang, "5、Electron-hole diffusion lengths > 175 m m in solution-grown CH 3 NH 3 PbI 3 single crystals," *Science (80-.).* **347**, 967 (2015).

[91] H. Cho, S. H. Jeong, M. H. Park, Y. H. Kim, C. Wolf, C. L. Lee, J. H. Heo, A. Sadhanala, N. S. Myoung, S. Yoo, S. H. Im, R. H. Friend, and T. W. Lee, "Overcoming the electroluminescence efficiency limitations of perovskite light-emitting diodes," *Science (80-.).* **350**, 1222 (2015).

[92] H. Uratani and K. Yamashita, "Charge Carrier Trapping at Surface Defects of Perovskite Solar Cell Absorbers: A First-Principles Study," *J. Phys. Chem. Lett.* **8**, 742 (2017).

[93] K. Wojciechowski, S. D. Stranks, A. Abate, G. Sadoughi, A. Sadhanala, N. Kopidakis, G. Rumbles, C. Z. Li, R. H. Friend, A. K. Y. Jen, and H. J. Snaith, "Heterojunction modification for highly efficient organic-inorganic perovskite solar cells," *ACS Nano* **8**, 12701 (2014).

[94] M. Batmunkh, C. J. Shearer, M. Bat-Erdene, M. J. Biggs, and J. G. Shapter, "Single-Walled Carbon Nanotubes Enhance the Efficiency and Stability of Mesoscopic Perovskite Solar Cells," *ACS Appl. Mater. Interfaces* **9**, 19945 (2017).

[95] S. Rühle, "Tabulated values of the Shockley-Queisser limit for single junction solar cells," *Sol. Energy* **130**, 139 (2016).

[96] W. Shockley and H. J. Queisser, "Detailed balance limit of efficiency of p-n junction solar cells," *J. Appl. Phys.* **32**, 510 (1961).

[97] S. Gharibzadeh, I. M. Hossain, P. Fassl, B. A. Nejand, T. Abzieher, M. Schultes, E. Ahlswede, P. Jackson, M. Powalla, S. Schäfer, M. Rienäcker, T. Wietler, R. Peibst, U. Lemmer, B. S. Richards, and U. W. Paetzold, "2D/3D Heterostructure for Semitransparent Perovskite Solar Cells with Engineered Bandgap Enables Efficiencies Exceeding 25% in Four-Terminal Tandems with Silicon and CIGS," *Adv. Funct. Mater.* **30** (2020).

[98] Y. Yan, "All-Perovskite Tandem Solar Cell Showing Unprecedentedly High Open-Circuit Voltage," *Joule* **2**, 2206 (2018).

[99] Z. Yang, Z. Yu, H. Wei, X. Xiao, Z. Ni, B. Chen, Y. Deng, S. N. Habisreutinger, X. Chen, K. Wang, J. Zhao, P. N. Rudd, J. J. Berry, M. C. Beard, and J. Huang, "Enhancing electron diffusion length in narrow-bandgap perovskites for efficient monolithic perovskite tandem solar cells," *Nat. Commun.* **10**, 1 (2019).

[100] R. Lin, K. Xiao, Z. Qin, Q. Han, C. Zhang, M. Wei, M. I. Saidaminov, Y. Gao, J. Xu, M. Xiao, A. Li, J. Zhu, E. H. Sargent, and H. Tan, "Monolithic all-perovskite tandem solar cells with 24.8% efficiency exploiting comproportionation to suppress Sn(ii) oxidation in precursor ink," *Nat. Energy* **4**, 864 (2019).

[101] Z. Yu, Z. Yang, Z. Ni, Y. Shao, B. Chen, Y. Lin, H. Wei, Z. J. Yu, Z. Holman, and J. Huang, "Simplified interconnection structure based on C60/SnO2-x for all-perovskite tandem solar cells," *Nat. Energy* **5**, 657 (2020).

[102] D. Zhao, Y. Yu, C. Wang, W. Liao, N. Shrestha, C. R. Grice, A. J. Cimaroli, L. Guan, R. J. Ellingson, K. Zhu, X. Zhao, R. G. Xiong, and Y. Yan, "Low-bandgap mixed tin-lead iodide perovskite absorbers with long carrier lifetimes for all-perovskite tandem solar cells," *Nat. Energy* **2**, 1 (2017).

[103] Z. Wang, X. Zhu, S. Zuo, M. Chen, C. Zhang, C. Wang, X. Ren, Z. Yang, Z. Liu, X. Xu, Q. Chang, S. Yang, F. Meng, Z. Liu, N. Yuan, J. Ding, S. Liu, and D. Yang, "27%-Efficiency Four-Terminal Perovskite/Silicon Tandem Solar Cells by Sandwiched Gold Nanomesh," *Adv. Funct. Mater.* **30**, 1 (2020).

[104] M. H. Futscher and B. Ehrler, "Efficiency Limit of Perovskite/Si Tandem Solar Cells," *ACS Energy Lett.* **1**, 863 (2016).

[105] A. H. Ali, Z. Hassan, and A. Shuhaimi, "Enhancement of optical transmittance and electrical resistivity of post-annealed ITO thin films RF sputtered on Si," *Appl. Surf. Sci.* **443**, 544 (2018).

[106] K. Han, M. Xie, L. Zhang, L. Yan, J. Wei, G. Ji, Q. Luo, J. Lin, Y. Hao, and C. Q. Ma, "Fully solution processed semi-transparent perovskite solar cells with spray-coated silver nanowires/ZnO composite top electrode," *Sol. Energy Mater. Sol. Cells* **185**, 399 (2018).

[107] K. Domanski, J. P. Correa-Baena, N. Mine, M. K. Nazeeruddin, A. Abate, M. Saliba, W. Tress, A. Hagfeldt, and M. Grätzel, "Not All That Glitters Is Gold: Metal-Migration-Induced Degradation in Perovskite Solar Cells," *ACS Nano* **10**, 6306 (2016).

[108] I. Jeon, A. Shawky, H. S. Lin, S. Seo, H. Okada, J. W. Lee, A. Pal, S. Tan, A. Anisimov, E. I. Kauppinen, Y. Yang, S. Manzhos, S. Maruyama, and Y. Matsuo, "Controlled Redox of Lithium-Ion Endohedral Fullerene for Efficient and Stable Metal Electrode-Free Perovskite Solar Cells," *J. Am. Chem. Soc.* **141**, 16553 (2019).

[109] A. G. Nasibulin, A. Kaskela, K. Mustonen, A. S. Anisimov, V. Ruiz, S. Kivistö, S. Rackauskas, M. Y. Timmermans, M. Pudas, B. Aitchison, M. Kauppinen, D. P. Brown, O. G. Okhotnikov, and E. I. Kauppinen, "Multifunctional free-standing single-walled carbon nanotube films," *ACS Nano* **5**, 3214 (2011).

[110] I. Jeon, R. Xiang, A. Shawky, Y. Matsuo, and S. Maruyama, "Single-Walled Carbon Nanotubes in Emerging Solar Cells: Synthesis and Electrode Applications," *Adv. Energy Mater.* **9**, 1 (2019).

[111] I. Jeon, Y. Matsuo, and S. Maruyama, "Single-Walled Carbon Nanotubes in Solar Cells," *Top. Curr. Chem.* **376**, 1 (2018).

[112] T. T. Larsen-Olsen, R. R. Sondergaard, K. Norrman, M. Jorgensen, and F. C. Krebs, "All printed transparent electrodes through an electrical switching mechanism: A convincing alternative to indium-tin-oxide, silver and vacuum," *Energy Environ. Sci.* **5**, 9467 (2012).

[113] M. Cai, Y. Wu, H. Chen, X. Yang, Y. Qiang, and L. Han, "Cost-Performance Analysis of Perovskite Solar Modules," *Adv. Sci.* **4** (2017).

[114] Z. Li, S. A. Kulkarni, P. P. Boix, E. Shi, A. Cao, K. Fu, S. K. Batabyal, J. Zhang, Q. Xiong, L. H. Wong, N. Mathews, and S. G. Mhaisalkar, "Laminated carbon nanotube networks for metal electrode-free efficient perovskite solar cells," *ACS Nano* **8**, 6797 (2014).

[115] S. Vaziri, V. Chen, L. Cai, Y. Jiang, M. E. Chen, R. W. Grady, X. Zheng, and E. Pop, " Ultrahigh Doping of Graphene Using Flame-Deposited MoO 3 ," *IEEE Electron Device Lett.* **41**, 1592 (2020).

[116] I. Jeon, J. Yoon, N. Ahn, M. Atwa, C. Delacou, A. Anisimov, E. I. Kauppinen, M. Choi, S. Maruyama, and Y. Matsuo, "Carbon Nanotubes versus Graphene as Flexible Transparent Electrodes in Inverted Perovskite Solar Cells," *J. Phys. Chem. Lett.* **8**, 5395 (2017).

[117] I. Jeon, C. Delacou, H. Okada, G. E. Morse, T. H. Han, Y. Sato, A. Anisimov, K. Suenaga, E. I. Kauppinen, S. Maruyama, and Y. Matsuo, "Polymeric acid-doped transparent carbon nanotube electrodes for organic solar cells with the longest doping durability," *J. Mater. Chem. A* **6**, 14553 (2018).

[118] L. Cai, C. J. McClellan, A. L. Koh, H. Li, E. Yalon, E. Pop, and X. Zheng, "Rapid flame synthesis of atomically thin MoO3 down to monolayer thickness for effective hole doping of WSe2," *Nano Lett.* **17**, 3854 (2017).

[119] F. Wang, D. Kozawa, Y. Miyauchi, K. Hiraoka, S. Mouri, Y. Ohno, and K. Matsuda, "Considerably improved photovoltaic performance of carbon nanotube-based solar cells using metal oxide layers," *Nat. Commun.* **6**, 1 (2015).

[120] K. K. Ki, J. B. Jung, K. P. Hyeon, M. K. Soo, H. Z. Geng, A. P. Kyung, H. J. Shin, S. M. Yoon, A. Benayad, J. Y. Choi, and H. L. Young, "Fermi level engineering of single-walled carbon nanotubes by AuCl 3 doping," *J. Am. Chem. Soc.* **130**, 12757 (2008).

[121] P. Liu, X. Liu, L. Lyu, H. Xie, H. Zhang, D. Niu, H. Huang, C. Bi, Z. Xiao, J. Huang, and Y. Gao, "Interfacial electronic structure at the CH3NH3PbI3/MoOx interface," *Appl. Phys. Lett.* **106** (2015).

[122] P. Schulz, J. O. Tiepelt, J. A. Christians, I. Levine, E. Edri, E. M. Sanehira, G. Hodes, D. Cahen, and A. Kahn, "High-work-function molybdenum oxide hole extraction contacts in hybrid organic-inorganic perovskite solar cells," *ACS Appl. Mater. Interfaces* **8**, 31491 (2016).

[123] N. T. Dee, J. Li, A. O. White, C. Jacob, W. Shi, P. R. Kidambi, K. Cui, D. N. Zakharov, N. Z. Janković, M. Bedewy, C. A. C. Chazot, J. Carpena-Núñez, B. Maruyama, E. A. Stach, D. L. Plata, and A. J. Hart, "Carbon-assisted catalyst pretreatment enables straightforward synthesis of high-density carbon nanotube forests," *Carbon,* **153** (2019).

[124] J. Li, M. Bedewy, A. O. White, E. S. Polsen, S. Tawfick, and A. J. Hart, "Highly Consistent Atmospheric Pressure Synthesis of Carbon Nanotube Forests by Mitigation of Moisture Transients," *J. Phys. Chem. C* **120**, 11277 (2016).

[125] K. Cui, T. Chiba, S. Omiya, T. Thurakitseree, P. Zhao, S. Fujii, H. Kataura, E. Einarsson, S. Chiashi, and S. Maruyama, "Self-assembled microhoneycomb network of single-walled carbon nanotubes for solar cells," *J. Phys. Chem. Lett.* **4**, 2571 (2013).

[126] S. Jessl, D. Copic, S. Engelke, S. Ahmad, and M. De Volder, "Hydrothermal Coating of Patterned Carbon Nanotube Forest for Structured Lithium-Ion Battery Electrodes," *Small* **15** (2019).

[127] Y. Bai, B. Shen, S. Zhang, Z. Zhu, S. Sun, J. Gao, B. Li, Y. Wang, R. Zhang, and F. Wei, "Storage of Mechanical Energy Based on Carbon Nanotubes with High Energy Density and Power Density," *Adv. Mater.* **1800680**, 1 (2018).

[128] Q. Kong, L. Bodelot, B. Lebental, Y. D. Lim, L. L. Shiau, B. Gusarov, C. W. Tan, K. Liang, C. Lu, C. S. Tan, P. Coquet, and B. K. Tay, "Novel three-dimensional carbon nanotube networks as high performance thermal interface materials," *Carbon,* **132**, 359 (2018).

[129] X. Wang, A. Ugur, H. Goktas, N. Chen, M. Wang, N. Lachman, E. Kalfon-Cohen, W. Fang, B. L. Wardle, and K. K. Gleason, "Room Temperature Resistive Volatile Organic Compound Sensing Materials Based on a Hybrid Structure of Vertically Aligned Carbon Nanotubes and Conformal oCVD/iCVD Polymer Coatings," *ACS Sensors* **1**, 374 (2016).

[130] J. Lee, S. S. Kessler, and B. L. Wardle, "Void-Free Layered Polymeric Architectures via Capillary-Action of Nanoporous Films," *Adv. Mater. Interfaces* **7**, 1 (2020).

[131] B. Lee, Y. Baek, M. Lee, D. H. Jeong, H. H. Lee, J. Yoon, and Y. H. Kim, "A carbon nanotube wall membrane for water treatment," *Nat. Commun.* **6**, 1 (2015).

[132] M. Sun, C. Boo, W. Shi, J. Rolf, E. Shaulsky, W. Cheng, D. L. Plata, J. Qu, and M. Elimelech, "Engineering Carbon Nanotube Forest Superstructure for Robust Thermal Desalination Membranes," *Adv. Funct. Mater.* **29**, 1 (2019).

[133] M. Chhowalla, K. B. K. Teo, C. Ducati, N. L. Rupesinghe, G. A. J. Amaratunga, A. C. Ferrari, D. Roy, J. Robertson, and W. I. Milne, "Growth process conditions of vertically aligned carbon nanotubes using plasma enhanced chemical vapor deposition," *J. Appl. Phys.* **90**, 5308 (2001).

[134] H. Cui, G. Eres, J. Y. Howe, A. Puretkzy, M. Varela, D. B. Geohegan, and D. H. Lowndes, "Growth behavior of carbon nanotubes on multilayered metal catalyst film in chemical vapor deposition," *Chem. Phys. Lett.* **374**, 222 (2003).

[135] M. Xu, D. N. Futaba, M. Yumura, and K. Hata, "Alignment control of carbon nanotube forest from random to nearly perfectly aligned by utilizing the crowding effect," *ACS Nano* **6**, 5837 (2012).

[136] Y. Won, "Zipping, entanglement, and the elastic modulus of aligned single-walled carbon nanotube film," *Proc. Natl. Acad. Sci.* **110**, 20426 (2013).

[137] S. Yasuda, T. Hiraoka, D. N. Futaba, T. Yamada, M. Yumura, and K. Hata, "Existence and kinetics of graphitic carbonaceous impurities in carbon nanotube forests to assess the absolute purity," *Nano Lett.* **9**, 769 (2009).

[138] L. Zhang, Z. Li, Y. Tan, G. Lolli, N. Sakulchaicharoen, F. G. Requejo, B. S. Mun, and D. E. Resasco, "Influence of a top crust of entangled nanotubes on the structure of vertically aligned forests of single-walled carbon nanotubes," *Chem. Mater.* **18**, 5624 (2006).

[139] S. Kim, H. Sojoudi, H. Zhao, D. Mariappan, G. H. Mckinley, K. K. Gleason, and A. J. Hart, "Ultrathin high-resolution flexographic printing using nanoporous stamps," *Sci. Adv.* (2016).

[140] A. L. Kaiser, I. Y. Stein, K. Cui, and B. L. Wardle, "Morphology control of aligned carbon nanotube pins formed via patterned capillary densification," *Nano Futur.* **3** (2019).

[141] M. F. L. De Volder, S. J. Park, S. H. Tawfick, D. O. Vidaud, and A. J. Hart, "Fabrication and electrical integration of robust carbon nanotube micropillars by self-directed elastocapillary densification," *J. Micromechanics Microengineering* **21** (2011).

[142] S. J. Park, J. Shin, D. J. Magagnosc, S. Kim, C. Cao, K. T. Turner, P. K. Purohit, D. S. Gianola, and A. J. Hart, "Strong, Ultralight Nanofoams with Extreme Recovery and Dissipation by Manipulation of Internal Adhesive Contacts," *ACS Nano* **14**, 8383 (2020).

[143] S. Kim, Y. Jiang, K. L. T. Towell, M. S. H. Boutilier, N. Nayakanti, C. Cao, C. Chen, C. Jacob, H. Zhao, K. T. Turner, and A. J. Hart, "Soft nanocomposite electroadhesives for digital micro- And nanotransfer printing," *Sci. Adv.* **5**, 1 (2019).

[144] H. M. Duong, E. Einarsson, J. Okawa, R. Xiang, and S. Maruyama, "Thermal degradation of single-walled carbon nanotubes," *Jpn. J. Appl. Phys.* **47**, 1994 (2008).

[145] S. Banerjee, T. Hemraj-Benny, and S. S. Wong, "Covalent surface chemistry of single-walled carbon nanotubes," *Adv. Mater.* **17**, 17 (2005).

[146] M. De Volder and A. J. Hart, "Engineering hierarchical nanostructures by elastocapillary self-assembly," *Angew. Chemie - Int. Ed.* **52**, 2412 (2013).

[147] D. J. Babu, S. Yadav, T. Heinlein, G. Cherkashinin, and J. J. Schneider, "Carbon dioxide plasma as a versatile medium for purification and functionalization of vertically aligned carbon nanotubes," *J. Phys. Chem. C* **118**, 12028 (2014).

[148] J. Wang, A. N. Kawde, and M. Musameh, "Carbon-nanotube-modified glassy carbon electrodes for amplified label-free electrochemical detection of DNA hybridization," *Analyst* **128**, 912 (2003).

[149] P. Singh, J. Kumar, F. M. Toma, J. Raya, M. Prato, B. Fabre, S. Verma, and A. Bianco, "Synthesis and characterization of nucleobase-carbon nanotube hybrids," *J. Am. Chem. Soc.* **131**, 13555 (2009).

[150] A. J. Hart and A. H. Slocum, "Rapid growth and flow-mediated nucleation of millimeter-scale aligned carbon nanotube structures from a thin-film catalyst," *J. Phys. Chem. B* **110**, 8250 (2006).

[151] B. He, Y. Yang, M. F. Yuen, X. F. Chen, C. S. Lee, and W. J. Zhang, "Vertical nanostructure arrays by plasma etching for applications in biology, energy, and electronics," *Nano Today* **8**, 265 (2013).

[152] H. Puliyalil and U. Cvelbar, "Selective plasma etching of polymeric substrates for advanced applications," *Nanomaterials* **6** (2016).

[153] C. Chen, A. Ogino, X. Wang, and M. Nagatsu, "Oxygen functionalization of multiwall carbon nanotubes by Ar/H_2O plasma treatment.," *Diam. Relat. Mater.* **20**, 153 (2011).

[154] Y. Won, Y. Gao, R. Guzman De Villoria, B. L. Wardle, R. Xiang, S. Maruyama, T. W. Kenny, and K. E. Goodson, "Nonhomogeneous morphology and the elastic modulus of aligned carbon nanotube films," *J. Micromechanics Microengineering* **25**, 115023 (2015).

[155] H. Deng, K. Endo, and K. Yamamura, "Atomic-scale and pit-free flattening of GaN by combination of plasma pretreatment and time-controlled chemical mechanical polishing," *Appl. Phys. Lett.* **107**, 3 (2015).

[156] B. N. Chapman and V. J. Minkiewicz, "Flow rate effects in plasma etching," *J. Vac. Sci. Technol.* **15**, 329 (1978).

[157] A. Gohel, K. C. Chin, Y. W. Zhu, C. H. Sow, and A. T. S. Wee, "Field emission properties of N2and Ar plasma-treated multi-wall carbon nanotubes," *Carbon N. Y.* **43**, 2530 (2005).

[158] J. Lee, A. Efremov, J. Lee, K. Kim, and K.-H. Kwon, "Etching characteristics of carbon nanotube thin films in O2/Ar plasma," *J. Nanosci. Nanotechnol.* **16**, 12021 (2016).

[159] B. Zhao, L. Zhang, X. Wang, and J. Yang, "Surface functionalization of vertically-aligned carbon nanotube forests by radio-frequency Ar/O2plasma," *Carbon N. Y.* **50**, 2710 (2012).

[160] W. H. Wang, B. C. Huang, L. S. Wang, and D. Q. Ye, "Oxidative treatment of multi-wall carbon nanotubes with oxygen dielectric barrier discharge plasma," *Surf. Coatings Technol.* **205**, 4896 (2011).

[161] Q. Wang, J. Dai, W. Li, Z. Wei, and J. Jiang, "The effects of CNT alignment on electrical conductivity and mechanical properties of SWNT/epoxy nanocomposites," *Compos. Sci. Technol.* **68**, 1644 (2008).

[162] M. Xu, D. N. Futaba, M. Yumura, and K. Hata, "Alignment control of carbon nanotube forest from random to nearly perfectly aligned by utilizing the crowding effect," *ACS Nano* **6**, 5837 (2012).

[163] M. Bedewy and A. J. Hart, "Mechanical coupling limits the density and quality of self-organized carbon nanotube growth," *Nanoscale* **5**, 2928 (2013).

[164] A. Ya'akobovitz, M. Bedewy, A. Rao, and A. J. Hart, "Strain relaxation and resonance of carbon nanotube forests under electrostatic loading," *Carbon,* **96**, 250 (2016).

[165] M. Bedewy, E. R. Meshot, M. J. Reinker, and A. J. Hart, "Population growth dynamics of carbon nanotubes," *ACS Nano* **5**, 8974 (2011).

[166] H. Zhao, S. J. Park, B. R. Solomon, S. Kim, D. Soto, A. T. Paxson, K. K. Varanasi, and A. J. Hart, "Synthetic Butterfly Scale Surfaces with Compliance-Tailored Anisotropic Drop Adhesion," *Adv. Mater.* **31**, 1 (2019).

[167] S. J. Park, H. Zhao, S. Kim, M. De Volder, and A. John Hart, "Predictive Synthesis of Freeform Carbon Nanotube Microarchitectures by Strain-Engineered Chemical Vapor Deposition," *Small*, 4393 (2016).

[168] M. De Volder, S. Park, S. Tawfick, and A. J. Hart, "Strain-engineered manufacturing of freeform carbon nanotube microstructures," *Nat. Commun.* **5**, 1 (2014).

[169] J. Li, M. Bedewy, A. O. White, E. S. Polsen, S. Tawfick, and A. John Hart, "Highly Consistent Atmospheric Pressure Synthesis of Carbon Nanotube Forests by Mitigation of Moisture Transients," *J. Phys. Chem. C* **120**, 11277 (2016).

[170] K. Cui, A. Kumamoto, R. Xiang, H. An, B. Wang, T. Inoue, S. Chiashi, Y. Ikuhara, and S. Maruyama, "Synthesis of subnanometer-diameter vertically aligned single-walled carbon nanotubes with copper-anchored cobalt catalysts," *Nanoscale* **8**, 1608 (2016).

[171] R. Xiang, E. Einarsson, Y. Murakami, J. Shiomi, S. Chiashi, Z. Tang, and S. Maruyama, "Diameter modulation of vertically aligned single-walled carbon nanotubes," *ACS Nano* **6**, 7472 (2012).

[172] T. Maruyama, T. Okada, K. P. Sharma, T. Suzuki, T. Saida, S. Naritsuka, Y. Iizumi, T. Okazaki, and S. Iijima, "Vertically aligned growth of small-diameter single-walled carbon nanotubes by alcohol catalytic chemical vapor deposition with Ir catalyst," *Appl. Surf. Sci.* **509**, 145340 (2020).

[173] I. Ivanov, A. Puretzky, G. Eres, H. Wang, Z. Pan, H. Cui, R. Jin, J. Howe, and D. B. Geohegan, "Fast and highly anisotropic thermal transport through vertically aligned carbon nanotube arrays," *Appl. Phys. Lett.* **89**, 1 (2006).

[174] L. Ping, P. X. Hou, C. Liu, and H. M. Cheng, "Vertically aligned carbon nanotube arrays as a thermal interface material," *APL Mater.* **7** (2019).

[175] S. Vollebregt, F. D. Tichelaar, H. Schellevis, C. I. M. Beenakker, and R. Ishihara, "Carbon nanotube vertical interconnects fabricated at temperatures as low as 350 °c," *Carbon,* **71**, 249 (2014).

[176] T. Xu, Z. Wang, J. Miao, X. Chen, and C. M. Tan, "Aligned carbon nanotubes for through-wafer interconnects," *Appl. Phys. Lett.* **91**, 8 (2007).

List of publications

First Author Publications

1. Y. Qian‡, **S. Seo**‡, I. Jeon‡, H. Lin, S. Okawa, Y. Zheng, A. Shawky, A. Anisimov, E. I Kauppinen, J. Kong, R. Xiang, Y. Matsuo, S. Maruyama, "MoS_2-carbon nanotube heterostructure as efficient hole transporters and conductors in perovskite solar cells", Appl. Phys. Express, 13(7) (2020.7) (‡equal contribution)

2. **S. Seo**, S. Kim, S. Yamamoto, K. Cui, T. Inoue, S. Chiashi, S. Maruyama, A. J. Hart, "Tailoring the surface morphology of carbon nanotube forest by plasma etching: a parametric study", submitted.

3. **S. Seo**‡, I. Jeon‡, R. Xiang, C. Lee, H. Zhang, T. Tanaka, J.-W. Lee, D. Suh, T. Ogamoto, R. Nishikubo, A. Saeki, S. Chiashi, J. Shiomi, H. Kataura, H. M. Lee, Y. Yang, Y. Matsuo, S. Maruyama, "Semiconducting carbon nanotubes as crystal growth templates and grain bridges in perovskite solar cells", J. Mater. Chem. A, 7, 12987-12992, (2019.5) (‡equal contribution)

4. I. Jeon‡, **S. Seo**‡, Y. Sato, C. Delacou, A. Anisimov, K. Suenaga, E. I Kauppinen, S. Maruyama, Y. Matsuo, "Perovskite solar cells using carbon nanotubes both as cathode and as anode", J. Phys. Chem. C, 121(46), 25743-25749 (2017.10). (‡equal contribution)

5. **S. Seo**, S. Maruyama et al., "Highly Transparent and Efficient Metal Electrode-free Semi-Transparent Perovskite Solar Cells by Multifunctional MoO3-Doping of Carbon Nanotube Top Contact", to be submitted.

Co-Author Publications

1. H.-S. Lin, J.-M. Lee, J. Han, C. Lee, **S. Seo**, S. Tan, H. M. Lee, E. J. Choi, M. S Strano, Y. Yang, S. Maruyama, I. Jeon, Y. Matsuo, J.-W. Oh, "Denatured M13 Bacteriophage-Templated Perovskite Solar Cells Exhibiting High Efficiency", Adv. Sci., 2000782 (2020.8).

2. I. Jeon, A. Shawky, **S. Seo**, Y. Qian, A. S Anisimov, E. Kauppinen, Y. Matsuo, S. Maruyama, "Carbon nanotubes to outperform metal electrodes in perovskite solar cells via dopant engineering and hole-selectivity enhancement", J. Mater. Chem. A, 8, 11141-11147 (2020.5).

3. H. S. Kum, H. Lee, S. Kim, S. Lindemann, W. Kong, K. Qiao, P. Chen, J. Irwin, J. H. Lee, S. Xie, S. Subramanian, J. Shim, S.-H. Bae, C. Choi, L. Ranno, **S. Seo**, S. Lee, J. Bauer, H. Li, K. Lee, J. A. Robinson, C. A. Ross, D. G. Schlom, M. S. Rzchowski, C.-B. Eom, J. Kim, "Heterogeneous integration of single-crystalline complex-oxide membranes", Nature, 578(7793), 75-81 (2020.1).

4. Y. Qian, I. Jeon, Y.-L. Ho, C. Lee, S. Jeong, C. Delacou, **S. Seo**, A. Anisimov, E. I Kaupinnen, Y. Matsuo, Y. Kang, H.-S. Lee, D. Kim, J.-J. Delaunay, S. Maruyama, "Multifunctional Effect of p-Doping, Antireflection, and Encapsulation by Polymeric Acid for High Efficiency and Stable Carbon Nanotube-Based Silicon Solar Cells", Adv. Energy Mater., 1902389 (2020.1).

5. I. Jeon, A. Shawky, H.-S. Lin, **S. Seo**, H. Okada, J.-W. Lee, A. Pal, S. Tan, A. Anisimov, E. I Kauppinen, Y. Yang, S. Manzhos, S. Maruyama, Y. Matsuo, "Controlled Redox of Lithium-Ion Endohedral Fullerene for Efficient and Stable Metal Electrode-Free Perovskite Solar Cells", J. Am. Chem. Soc., 16553-16558 (2019.9).

6. A. Thote, I. Jeon, J.-W. Lee, **S. Seo**, H.-S. Lin, Y. Yang, H. Daiguji, S. Maruyama, Y. Matsuo, "Stable and reproducible 2D/3D formamidinium–lead–iodide perovskite solar cells", ACS Appl. Energy Mater. 2(4), 2486-2493 (2019.3).

7. J.-W. Lee, I. Jeon, H.-S. Lin, **S. Seo**, T.-H. Han, A. Anisimov, E. I Kauppinen, Y. Matsuo, S. Maruyama, Y. Yang, "Vapor-assisted ex-situ doping of carbon nanotube toward efficient and stable perovskite solar cells", Nano Lett., 19(4), 2223-2230 (2018.12).

8. H.-S. Lin, I. Jeon, R. Xiang, **S. Seo**, J.-W. Lee, C. Li, A. Pal, S. Manzhos, M. S. Goorsky, Y. Yang, S. Maruyama, Y. Matsuo, "Achieving High Efficiency in Solution-Processed Perovskite Solar Cells Using C60/C70Mixed Fullerenes", ACS Appl. Mater. Interfaces, 10(46), 39590-39598, (2018.9).

9. I. Jeon, H. Ueno, **S. Seo**, K. Aitola, R. Nishikubo, A. Saeki, H. Okada, G. Boschloo, S. Maruyama, Y. Matsuo, "Lithium-Ion Endohedral Fullerene (Li+@C60) Dopants in Stable Perovskite Solar Cells Induce Instant Doping and Anti-Oxidation", Angew. Chem. Int. Ed., 57(17), 4607-4611 (2018.2).

10. I. Jeon, R. Sakai, **S. Seo**, G. E. Morse, H. Ueno, T. Nakagawa, Y. Qian, S. Maruyama, Y. Matsuo, "Engineering high-performance and air-stable PBTZT-stat-BDTT-8: PC 61 BM/PC 71 BM organic solar cells", J. Mater. Chem. A, 6, 5746-5751, (2018.2).

11. C. Delacou, I. Jeon, **S. Seo**, T. Nakagawa, E. I Kauppinen, S. Maruyama, Y. Matsuo, "Indium tin oxide-free small molecule organic solar cells using single-walled carbon nanotube electrodes ", ECS J. Solid State Sci. Technol., 6(6), M3181-M3184 (2017.5).

International Conferences

Poster Presentation

1. **S. Seo**, I. Jeon, T. Sakaguchi, T. Inoue, R. Xiang, S. Chiashi, Y. Matsuo, S. Maruyama, "Lamination of Vertically Aligned Single-Walled Carbon Nanotube Forests on Perovskite Solar Cells via Membrane Filter Transfer Method", CIAiS International Symposium, Tokyo, 11 (2017.2).

2. **S. Seo**, I. Jeon, T. Sakaguchi, T. Inoue, R. Xiang, S. Chiashi, Y. Matsuo, S. Maruyama, "Lamination of Vertically Aligned Single-Walled Carbon Nanotube Forests on Perovskite Solar Cells via Membrane Filter Transfer Method", The Fullerenes, Nanotubes and Graphene Research Society 52th Symposium, 3P-11, Tokyo, (2017.3).

3. I. Jeon, H. Ueno, **S. Seo**, N. Ryosuke, S. Akinori, H. Okada, S. Maruyama, Y. Matsuo, "Air-stable Perovskite solar cells using Li-containing fullerene salts as both dopant and anti-oxidant", The Fullerenes, Nanotubes and Graphene Research Society 53th Symposium, Kyoto, 1P-4 (2017.9).

4) I. Jeon, **S. Seo**, Y. Sato, D. Clement, A. Anton, K. Suenaga, E. I. Kauppinen, S. Maruyama, Y. Matsuo, "Perovskite Solar Cells using Carbon Nanotubes as both Cathode and Anode Electrodes", The Fullerenes, Nanotubes and Graphene Research Society 53th Symposium, Kyoto, 2-6 (2017.9).

5) **S. Seo**, S. Okawa, T. Inoue, R. Xiang, S. Chiashi, E. I. Kauppinen, I. Jeon, Y. Matsuo, S. Maruyama, "Interface Engineering of Single-Walled Carbon Nanotube Cathode in

Inverted Perovskite Solar Cells" , The Fullerenes, Nanotubes and Graphene Research Society S3th Symposium, Kyoto, 2P-12 (2017.9).

6) H. Ueno, I. Jeon, **S. Seo**, S. Maruyama, Y. Matsuo, "High Stability Perovskite Solar Cells by Li+-Containing Fullerene Salt as both Dopant and Anti-Oxidant", MRS Fall Meeting 2017, Boston, ES01.07.25 (2017.11).

7) **S. Seo**, I. Jeon, H. Zhang, T. Tanaka, H. Kataura, Y. Matsuo, S. Maruyama, "Semiconducting Carbon Nanotubes as Charge-transporting Grain Boundary Protector of Perovskite Solar Cells", The Fullerenes, Nanotubes and Graphene Research Society 54th Symposium, Tokyo, 3P-10 (2018.3)

8) **S. Seo**, I. Jeon, H. Zhang, S. Okawa, T. Tanaka, H. Kataura, Y. Matsuo, S. Maruyama "Achieving 19.7% Efficiency Perovskite Solar Cells with High Stability by using Semiconducting Single-walled Carbon Nanotube Grain Bridges", NT18: International Conference on the Science and Application of Nanotubes and Low-Dimensional Materials, Peking, PA089 (2018.7).

9) **S. Seo**, I. Jeon, Z. Hao, T. Tanaka, J.-W. Lee, D. Suh, J. Shiomi, Y. Yang, Y. Matsuo, H. Kataura, S. Maruyama "Semiconducting Single-Wall Carbon Nanotubes as Crystal Growth Templates and Grain Bridges in Perovskite Solar Cells", IUMRS-ICEM 2018, Daejeon, ThP62 (2018.8).

10) **S. Seo**, I. Jeon, H. Zhang, S. Okawa, T. Ogamoto, R. Nishikubo, A. Saeki, T. Tanaka, H. Kataura, Y. Matsuo, S. Maruyama, "Achieving High Efficiency Perovskite Solar Cells by Grain Engineering using Semiconducting Single-walled Carbon Nanotube", 31th International Microprocesses and Nanotechnology Conference, Hokkaido, 16P-11-102L (2018.11).

11) **S. Seo**, I. Jeon, R. Xiang, C. Lee, H. Zhang, T. Tanaka, J.-W. Lee, D. Suh, T. Ogamoto, R. Nishikubo, A. Saeki, S. Chiashi, J. Shiomi, H. Kataura, H. M. Lee, Y. Yang, Y. Matsuo, S. Maruyama, "Semiconducting Single-Wall Carbon Nanotubes as Crystal Growth Templates and Grain Bridges in Perovskite Solar Cells", NT19: International Conference on the Science and Application of Nanotubes and Low-Dimensional Materials, Wurzburg, P075 (2019.7).

12) **S. Seo**, I. Jeon, E. I. Kauppinen, Y. Matsuo, S. Maruyama, "Scalable MoO_3 Doping of Carbon Nanotube Electrodes towards Efficient Perovskite Solar Cells", 10th A3 Symposium on Emerging Materials : Nanomaterials for Electronics, Energy and Environment, Suwon, No. 4 (2019.10).

13) **S. Seo**, I. Jeon, E. I. Kauppinen, Y. Matsuo, S. Maruyama, "Stable MoO_3 Doping of Carbon Nanotube Top Electrodes for Highly Efficient Metal-Electrode-Free Perovskite Solar Cells", The Fullerenes, Nanotubes and Graphene Research Society 58th Symposium, Tokyo, 2P-2 (2020.3)

14) **S. Seo**, I. Jeon, K. Akino, H. Nagaya, E. I. Kauppinen, Y. Matsuo, S. Maruyama, "MoO3 Doping of Carbon Nanotube Top Electrodes for Highly Efficient Metal-Electrode-Free Perovskite Solar Cells", The Fullerenes, Nanotubes and Graphene Research Society 59th Symposium, Kyusyu, 2P-4 (2020.9)

Oral Presentation

1) **S. Seo**, S. Nomura, K. Ariu, Y. Yoshihara, K. Kumse, N. Funabiki, K. Ozawa, E. Tanaka, T. Yuki, "Monitoring of Natural Disaster based on Synthetic Aperture Radar (SAR) Satellite in Southeast Asia", The 68th International Astronautical Congress, Adelaide, IAC-17.E6.1.9 (2017.9).

2) **S. Seo**, I. Jeon, Y. Sato, C. Delacou, A. Anisimov, K. Suenaga, E. I. Kauppinen, S. Maruyama, Y. Matsuo, "Perovskite Solar Cells using Carbon Nanotubes both as Cathode and Anode", APS March Meeting 2018, Los Angeles, H40.00005 (2018.3)

3) H. Ueno, I. Jeon, **S. Seo**, N. Ryosuke, S. Akinori, S. Maruyama, Y. Matsuo, "Highly Stabilized Perovskite Solar Cells by Li+-Encapsulated [60]Fullerene Salt as Both Dopant and Anti-Oxidant", The Fullerenes, Nanotubes and Graphene Research Society 54th Symposium, Tokyo, 3-4 (2018.3)

List of Abbreviations

AFM: Atomic Force Microscopy

CNT: Carbon Nanotube

SiSC: Silicon Solar Cell

XPS: X-ray Photoelectron Spectroscopy

XRD: X-Ray Diffraction

EQE: External Quantum Efficiency

EIS: Electrochemical Impedance Spectroscopy

CVD: Chemical Vapor Deposition

PL: Photoluminescence

PYS: Photoelectron Yield Spectroscopy

SEM: Scanning Electron Microscopy

TEM: Transmission Electron Microscopy

SWNT: Single-walled Carbon Nanotubes

PSC: Perovskite Solar Cell